UNSTABLE RESONATOR SEMICONDUCTOR LASERS FABRICATED BY FOCUSED ION BEAM MICROMACHINING

James Brian Cser
B.S., California Institute of Technology, 1985

A thesis submitted to the faculty
of the Oregon Graduate Institute
of Science and Technology
in partial fulfillment of the
requirements for the degree
Master of Science
in
Applied Physics

October, 1990

The thesis "Unstable Resonator Semiconductor Lasers Fabricated by Focused Ion Beam Micromachining" by James Brian Cser has been examined and approved by the following examination committee:

Richard K. DeFreez, Advisor
Associate Professor

Reinhart Engelmann
Professor

R. Thomas Hawkins II
Tektronix, Inc.

For my family.

Acknowledgements

I graciously acknowledge...

Dr. Richard K. DeFreez, my faculty advisor, for all his help and guidance on this and other projects, for his inspirational standards of quality, and for more than once talking me out of turning in my tweezers.

Dr. Richard A. Elliott, my original faculty advisor, who once told me, prophetically, that graduate school is where you learn self-confidence.

Dr. David Depatie, of the Air Force Weapons Lab, for providing the motivation and funding for the work in this thesis; Dr. Weng Chow, of Sandia Laboratories, for letting me use his unstable resonator simulation program; Dr. Daniel Yap, of Hughes Research Labs, for providing the excellent laser material; and Dr. Mike Tilton, of Rockwell Corporation, for useful discussions about his unstable resonator model.

Micromachinists Union Local #809 — Alice Reinheimer, Peter Carleson, and Hongyu Ximen — for sharing with me their vast knowledge and skills, and for always going that extra micron. Also, the rest of the Optics group — Dave Bossert, Marc Felisky, Geoff Wilson, and Nu Yu — for putting up with all my annoying questions, and even answering most of them.

Bev Kyler, our APEE Department secretary, for being as nice as she is indispensable.

John Hunt, whose grounds never flap in the wind, for cheerfully clearing up many mysteries of the world of electronics.

The other students, faculty, and staff of the Oregon Graduate Institute, except for the ones who grab all the good donuts in the morning before I get a chance.

The Saturday night garage band, whatever name they're calling themselves this week...

...and everyone else who had the slightest bit to do with any of this. They know who they are.

Table of Contents

List of Figures

List of Tables

Abstract

UNSTABLE RESONATOR SEMICONDUCTOR LASERS

FABRICATED BY FOCUSED ION BEAM MICROMACHINING

James Brian Cser

B.S., California Institute of Technology, 1985

High power (>100 mW), single-lobed diffraction-limited light from a semiconductor laser is desirable for many applications, but laser configurations such as arrays have various problems associated with them. Unstable resonator configurations show good potential as a way to avoid these problems, but traditional wet chemical etching techniques cannot produce mirrors that are perpendicular to the substrate over their entire curvature. Focused ion beam (FIB) micromachining is a promising technique for fabricating such lasers.

This thesis will review the analytical theories of unstable resonators and discuss the need for a numerical model that includes gain and complex index effects. Two different numerical models, and their results, will be discussed. The apparatus and programming for FIB micromachining will be discussed. Problems encountered during the research will be described. Photographs of micromachined unstable resonator semiconductor lasers will be presented, as well

as their light output characteristics.

It will be shown that the FIB micromachining process produces high quality, reproducible mirrors. It will also be shown that, although single-lobed operation is not achieved, the output characteristics are reproducible, and that the unstable resonators produce the highest powers to date for this type of device.

Chapter 1 — Introduction

1.1 Unstable Resonator Semiconductor Lasers

The laser[1] is regarded as one of the most significant technological advances of the twentieth century. Laser light, because it can be highly directional and nearly monochromatic, has found countless scientific and engineering applications. There are many types of lasers now available, among them gas, solid-state, dye, and semiconductor lasers.

In comparison with the other types, semiconductor lasers are small, efficient, and inexpensive. For many semiconductor laser applications, such as solid-state laser end-pumping and free space optical communication, single-lobed, diffraction-limited beams with output powers of hundreds of milliwatts are required, but the best single-stripe devices [2] can produce only tens of milliwatts of continuous wave (CW) optical power in a single-lobed, diffraction-limited beam.

Figure 1.1 illustrates a typical semiconductor laser and the light emission from its output facet. The laser is essentially a sandwich of several semiconductor layers epitaxially grown on a substrate such as GaAs. In the active layer, the

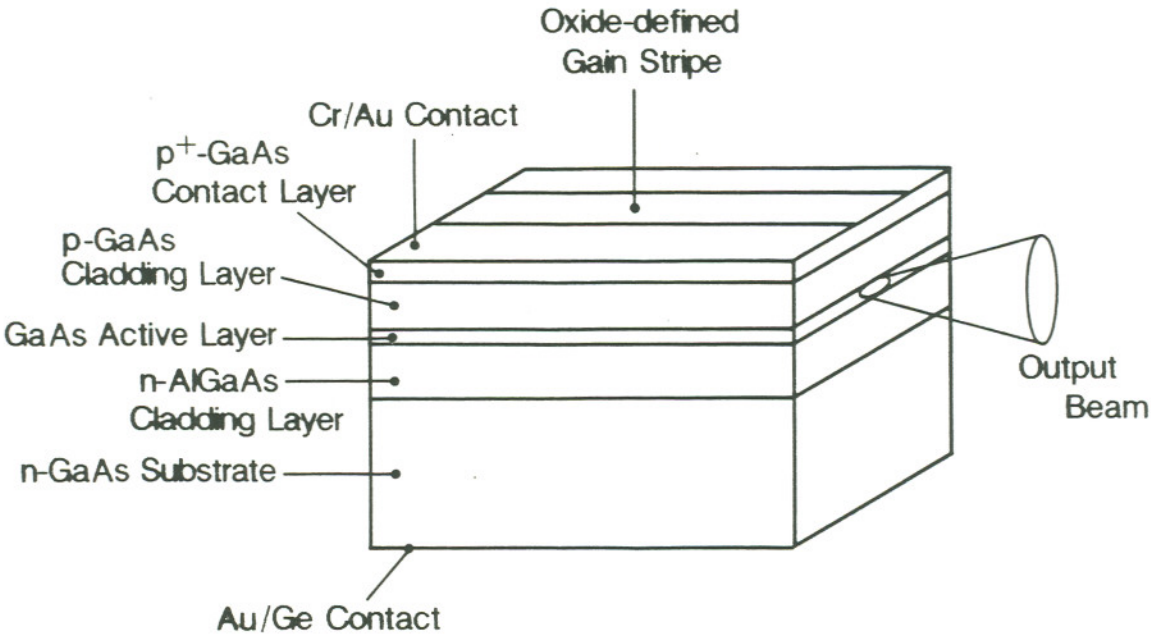

Figure 1.1 — Schematic of a typical semiconductor laser.

recombination of electrons and holes produces spontaneous emission, which in turn is amplified bystimulated emission, generating the laser light. The light is emitted from the laser through a small area of the facet, determined in the transverse dimension (perpendicular to the layers) by the thickness of the active layer and its refractive index relative to the surrounding layers, and in the lateral dimension (parallel to the layers) by the electrical contact window in the oxide layer (The figure shows a "gain-guided" laser. In an "index-guided" laser, the beam is laterally confined by additional lateral confining layers).

Output power from a semiconductor laser is limited by damage at the laser facet, caused by excessive optical power density ($>$ 1-10 MW/cm^2) at the facet. If the lasing stripe is wider than about 20 μm, then the laser has a tendency to form highly localized, self-focusing regions of optical power, or "filaments"[3], which produce local "hot spots" of intensity that can damage the facet before the rest of the laser is emitting at maximum power.

Furthermore, the nonuniform lasing creates a spatially incoherent near field. If the near field is spatially coherent, then the angular divergence is limited only by diffraction ("diffraction-limited"). A spatially incoherent near field, on the other hand, results in a far field with an angular divergence wider than the diffraction limit ("non-diffraction-limited"), which is undesirable for most applications. Therefore, the elimination of filaments is an important step towards the production of high power, single-lobed, diffraction-limited, semiconductor laser light.

One way filamentation can be avoided is to use arrays of lasers, with each element being small enough to prevent the formation of filaments. However, it is often observed[4,5] that adjacent array elements tend to oscillate 180° out of phase. The out-of-phase elements destructively interfere, resulting in an undesirable two-lobed far field pattern. To remove the phase shift, many variations on the array theme have been tried, such as diffraction-coupled[6], chirped[7], offset stripe[8,9], and Y-junction arrays[10]. For example, CW optical power of 350 mW with a diffraction-limited beam has been reported for an offset stripe array[9], but only 61%, or 215 mW was contained in the central lobe (Ideally, all of the output power should be contained in the central lobe). More recently, a complementary self-aligned (CSA) array[11] has produced diffraction-limited beams with a single lobe of 50 mW CW and with multiple lobes of 100 mW CW, and an interferometric array[12] has produced a four-lobed diffraction-limited beam of 200 mW CW.

An alternate method to suppress filamentation, without the the complications associated with arrays, is the use of an unstable resonator[13,14] geometry. An unstable resonator, an example of which is illustrated in Figure 1.2, employs a convex mirror to spread out filaments before they form, and thus permits higher output powers before the onset of catastrophic optical damage. It is "unstable" in the sense that the propagating beam does not reproduce itself after each round trip, as in a "stable" resonator. Resonator theory will be discussed in more detail in the next chapter.

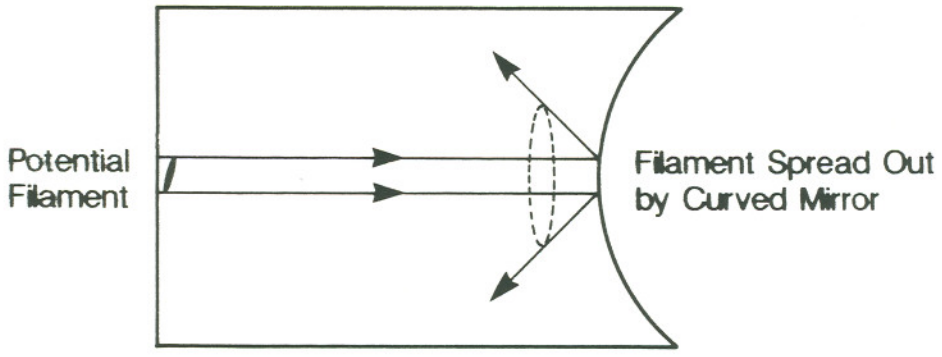

Figure 1.2 — Filament spreading in an unstable resonator.

Unstable resonators have been extensively used for gas and solid state lasers, but have only recently been fabricated for semiconductor lasers. In 1979, Bogotov et al[15]. made the first such devices, polishing the curved mirrors with a nylon thread coated with diamond paste. Since then, various groups have used wet chemical etching to etch curved mirrors in single-stripe GaAs[16-19] and GaInAsP[20] lasers, and in GaAs arrays[21], but none have shown both diffraction-limited far field patterns and the high optical powers that motivated the unstable resonator approach. The main problem is that the chemical etching rate depends in general on the orientation of the etch mask with respect to the crystal planes, making it difficult to produce high quality curved mirrors that are perpendicular to the substrate over their entire curvature.

One mirror fabrication technique that does not have this disadvantage is focused ion beam (FIB) micromachining[22,23]. The FIB system focuses a high energy beam of gallium ions onto a small spot to sputter away material where desired. Computer control enables the spot to be positioned with sub-micron precision. This technique has the advantages of being maskless and sample orientation-independent, and so avoids the problems encountered with wet chemical etching. Previous FIB work[24] has demonstrated planar mirrors in GaAs lasers that are nearly as smooth as cleaved facets and cause little degradation of the laser efficiency.

This thesis discusses the use of FIB micromachining to fabricate unstable resonator semiconductor lasers. Chapter 2 will discuss general resonator theory

and present analytical treatments of unstable resonators. Chapter 3 will discuss numerical methods for modeling unstable resonators. The FIB system and the procedures used in micromachining curved mirrors will be described in Chapter 4. Chapter 5 will report the results of the optical and electrical characterization of the fabricated unstable resonator lasers, and Chapter 6 will present conclusions and discuss possible future work on unstable resonator semiconductor lasers.

Chapter 2
Unstable Resonator Theory — Analytical

This chapter will discuss the basic theory of unstable optical resonators, survey their analytical models, and give some insight into the behavior of the various waveguide modes of unstable resonator semiconductor lasers.

2.1 Resonators

Laser operation requires two conditions: gain and feedback. Gain is the amplification necessary for the propagating beam to overcome the losses in the lasing medium and is produced by pumping the laser with light or charge carriers. The primary effect of gain on the medium is to introduce a complex component into the index of refraction. Although this is a necessary component of a working laser, this chapter will follow the historical development of the unstable resonator theory, and not introduce gain until the last section. Feedback — returning a portion of the amplified light back into the gain medium — is generally accomplished with a pair of opposing mirrors between which the light can oscillate, a system generically known as an optical resonator.

The characterization of optical resonators can be approached in a geometrical optics context by representing a resonator as a periodic system of lenses, as

was done by Boyd and Kogelnik[13]. This is shown schematically in Figure 2.1 . In this model, each mirror can be reprsented as a thin lens of focal length f = -R/2. Here we make three basic assumptions: that the lenses are very thin, that the beam is paraxial (near the centers of the lenses), and that diffraction effects of the beam at the edges of the mirrors can be neglected (this third assumption will not be valid in later analyses).

A periodic system of lenses is considered "stable" if the lateral displacement of an input beam oscillates periodically but remains bounded. If the lenses are of equal focal length, then the system can support a non-divergent beam if

$$0 \leq \frac{L}{f} \leq 4 \tag{2.1}$$

where L is the lens spacing and f is the focal length of the lens. In addition, two lenses with focal lengths f_1 and f_2 can be replaced by an equivalent single lens with focal length

$$\frac{1}{f_{eff}} = \frac{1}{f_1} + \frac{1}{f_2} - \frac{L}{f_1 f_2} \tag{2.2}$$

If we define an effective spacing for the two lens system by $L_{eff}=L+h_1+h_2$, where L is the physical distance between the lenses, $h_1 = L(f_{eff}/f_1)$ and $h_2 = L(f_{eff}/f_2)$, we obtain the relation

$$\frac{L_{eff}}{f_{eff}} = L\left\{\frac{2}{f_1} + \frac{2}{f_2} - \frac{L}{f_1 f_2}\right\} \tag{2.3}$$

Substituting back into the stability condition (2.1), and replacing the lenses with their equivalent mirrors, we finally arrive at the stability criterion

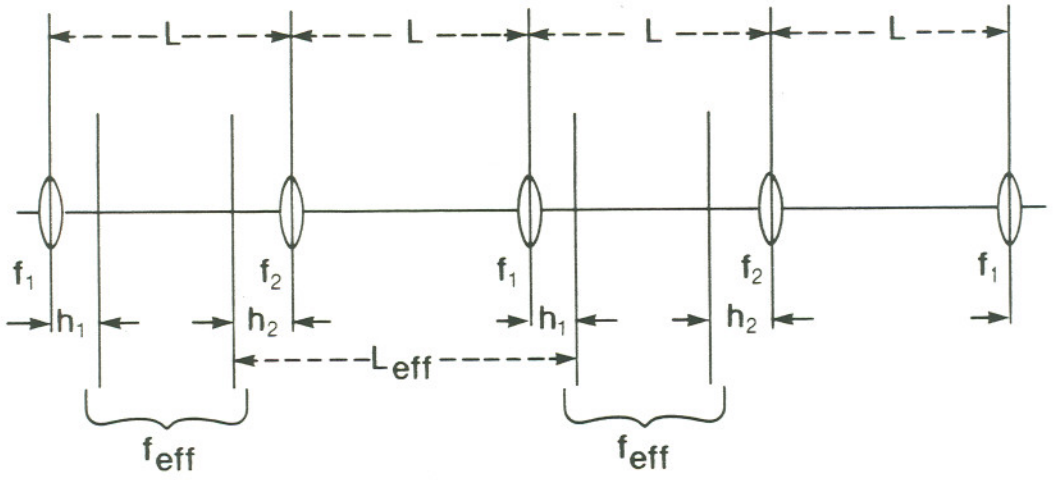

Figure 2.1 — A periodic system of lenses (after Ref. 13).

$$0 \leq \left(1-\frac{L}{R_1}\right)\left(1-\frac{L}{R_2}\right) \leq 1 \tag{2.4}$$

If we define "g-parameters"[13,25] by setting $g_1=1-L/R_1$ and $g_2=1-L/R_2$, where L is the length of the resonator, R_1 and R_2 are the radii of curvature for mirrors 1 and 2, respectively, then the stability criterion becomes

$$0 \leq g_1 g_2 \leq 1 \tag{2.5}$$

Figure 2.2 is the resulting diagram of the g_1g_2 plane. Any resonator that falls on or within the boundaries of the shaded area can support a stable, self-replicating beam. Conversely, an input beam will eventually diverge in any resonator outside the shaded region.

Different resonator types can be characterized by their positions on the diagram. Stable resonators, as mentioned above, occupy the shaded regions of the diagram. Stable configurations have been the most popular for lasers, because of their low losses. However, there is one drawback to a stable resonator design: in general, the beam inside a laser resonator has a gaussian lateral intensity profile. A consequence of this is that the beam must have a narrow waist inside the resonator (or a virtual waist outside the resonator). As a result, much of the volume of the gain medium between the mirrors does not contribute to lasing; the resonator has a "low mode volume".

Marginally stable resonators occupy the edges of the stability boundary. Two special cases — concentric resonators, where the two mirrors share the same center of curvature, and confocal resonators, where the each mirror's center of

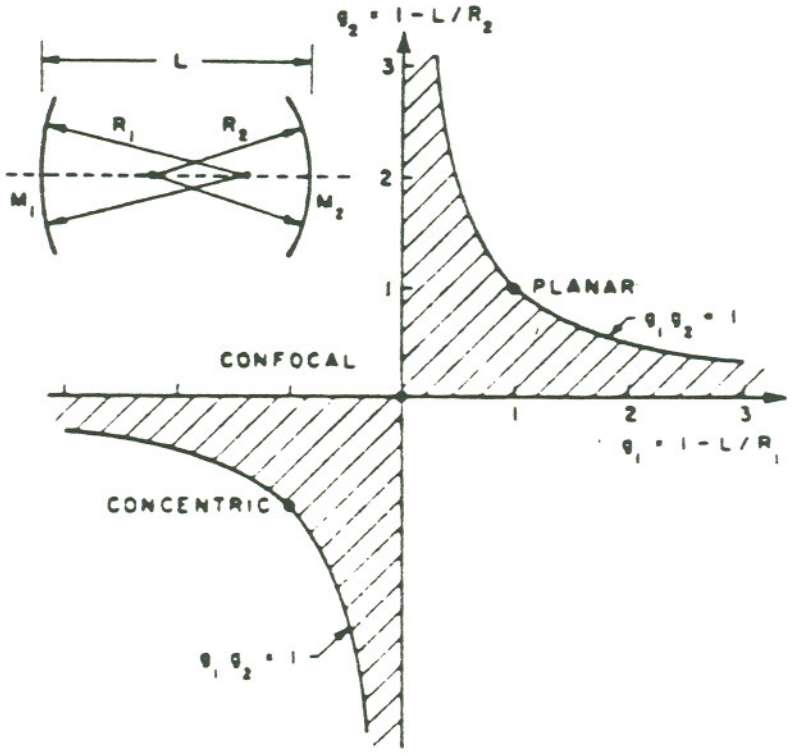

Figure 2.2 — Diagram of g_1g_2 plane. Shaded areas denote stable resonators (after Ref. 14)

curvature lies on the opposite mirror — have specialized, limited uses in lasers, but will not be discussed here. However, one type of marginally stable resonator, the planar resonator, is of great interest, since it is used in semiconductor lasers, which have seen a rapid increase of production in recent years. Although planar mirrors non-integral to a laser cavity, such as a gas laser tube, are usually difficult to keep properly aligned, semiconductor lasers can take advantage of the natural crystal planes, and parallel planar mirrors are easily made by cleaving the laser crystal at each end. Another advantage, common to all planar resonators, is that the entire volume of the gain region is available for lasing; the resonator has a "high mode volume".

The remaining areas of the diagram are occupied by the unstable resonators. Any beam propagating inside an unstable resonator experiences high losses from light escaping around the edges of the mirror. At first, having high losses does not seem very useful, but the high gain of semiconductor lasers can overcome the losses, and other benefits of the resonator can be exploited: a high mode volume, the ability to spread out filaments, as described in the first chapter, and the possibility of operating in a single lateral lasing mode, for reasons to be discussed in the following sections.

In the theory discussed in this and the next two sections, the mirrors are assumed to have finite width and the medium is assumed to have an infinite width. In this case, the losses are diffraction losses around the edges of the mirrors. For the theories discussed in Section 2.4 and Chapter 3, which specifically

model semiconductor unstable resonators, the gain medium is assumed to have a finite width, and the mirrors are assumed to be be much larger than the gain medium width. In these cases, the major losses are from light escaping out the sides of the gain medium.

2.2 Minimum Loss Calculations

In the Boyd and Kogelnik resonator theory discussed above, unstable resonators are predicted to have an infinite loss, since all the light eventually escapes outside the mirrors. Another approach is needed if a useful model for understanding unstable resonators is to be created. Early work by Fox and Li[25-27] used numerical integration to find the normal modes and their associated losses for planar and confocal resonators, and later for resonators with mirrors of arbitrary shape. Their method of describing the propagation of the resonator mode was based on Huygen's principle, which states that a scalar Fresnel integral can be used to calculate the electric field on a final aperture from that on an initial aperture. In their resonator calculations, Fox and Li assumed an even- or odd-symmetric initial field at the first mirror, propagated it to find the field at the second mirror, and then propagated that field back to find a new field at the first mirror. This was then repeated many times until the field at each mirror was unchanged from pass to pass, except for a complex constant.

For the case of unstable resonators with two strip (curved in one dimension) mirrors, the propagation integrals[25] are of the form

$$\gamma_1\psi_1(x_1) = \int_{S_2} K(x_1,x_2)e^{j\beta\left[h_1(x_1)+h_2(x_2)\right]}\psi_2(x_2)\, dS_2 \qquad (2.6a)$$

$$\gamma_2\psi_2(x_2) = \int_{S_1} K(x_2,x_1)e^{j\beta\left[h_2(x_2)+h_1(x_1)\right]}\psi_1(x_1)\, dS_1 \qquad (2.6b)$$

where ψ_1 and ψ_2 are the fields at mirrors S_1 and S_2, γ_1 and γ_2 are the complex eigenvalues from each propagation direction, $K(x_1,x_2)$ is a propagation kernel, $h(x_1)$ and $h(x_2)$ are the deviations of each mirror from planar, and β is the propagation constant of the medium. These two equations were then combined into a single equation, which was solved for the total loss Γ, equal to $\gamma_1\gamma_2$. The assumptions made were that the mirror dimensions are large compared to wavelength, and that the mirror perturbations are small compared to the mirror sizes and separation.

The authors plotted the loss per pass of various symmetric (both mirrors of equal curvature) resonator configurations against the Fresnel number $N = a^2/\lambda L$, where 2a equals the mirror diameter, λ is the wavelength of the light, and L is the resonator length. It was found that for the stable resonators ($g_1g_2 \leq 1$), the losses for the lowest order mode decrease steadily with increasing mirror size, while for the unstable resonators ($g_1g_2 > 1$), for increasing mirror size, the losses exhibit ripples around some constant value.

Siegman[14], using a purely geometric model that neglected diffraction effects, calculated losses for several resonators where $g_1 = g_2 = g$. The losses were independent of N, but were found to be in good agreement with the Fox and

Li[25,27] data, as illustrated in Figure 2.3 . The ripples in the Fox and Li data, it was theorized, were due to interference effects of the wave at the edges of the mirrors.

Siegman and Arrathoon[28] further extended the analysis, and proposed for unstable resonators an equivalent Fresnel number, N_{eq}, defined by

$$N_{eq} \equiv \frac{1}{2}\left(M-\frac{1}{M}\right)N = \frac{1}{2}\left(M-\frac{1}{M}\right)\frac{a^2}{\lambda L} \tag{2.7}$$

Here, M is the so-called magnification, a measure of how much a small lateral segment of a propagating beam is expanded over one complete pass through the resonator. M is given by

$$M = \frac{1+\sqrt{1-(g_1g_2)^{-1}}}{1-\sqrt{1-(g_1g_2)^{-1}}} \tag{2.8}$$

and satisfies the relation

$$M = \frac{1}{|\Gamma|^2} \tag{2.9}$$

The physical significance of N_{eq} can be looked at in a number of different ways. A way described by the authors is an analogy to the Fresnel number, N: the Fresnel number represents the difference of path length, in half wavelengths, of a plane wave traveling from the center of one mirror to the center of the next mirror, as compared to a wave traveling to the edge of the next mirror. Because of the convex curvature of the mirrors, a cylindrical wave would seem to come from a virtual center behind the mirror. This modified path length difference in

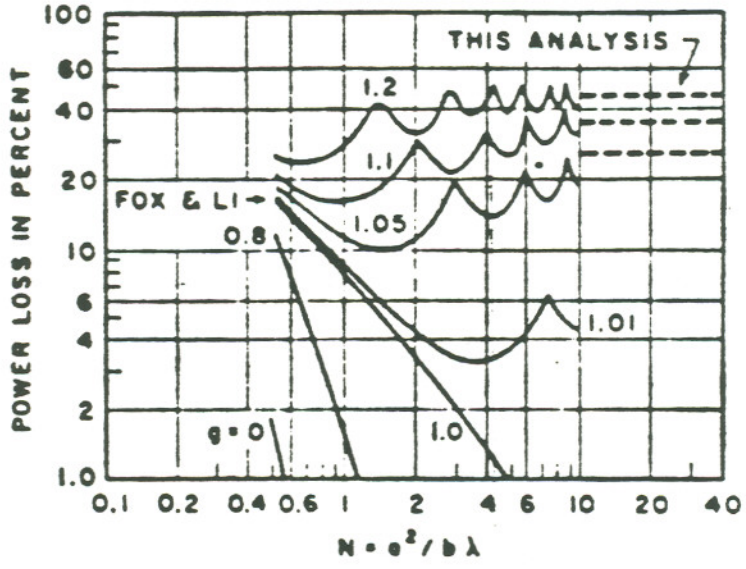

Figure 2.3 — Power loss versus Fresnel number for various unstable resonators. Numerical analysis (solid lines) is compared to geometrical analysis (dashed lines). After Ref. 14.

half wavelengths, is the equivalent Fresnel number.

The ripples in the loss curve, it is argued, are caused by interference between the reflected and diffracted waves, and should be related to N_{eq}. The authors found that the loss peaks indeed occur near integral values of N_{eq}, and occur independently of the value of g, as shown in Figure 2.4 . From observations of the abrupt change of the near field patterns near the cusping points, it was concluded that these points are intersections of the loss curves from different lateral modes.

A paper by Smith[29] showed that for strip resonators, when N_{eq} is above a critical value, estimated by $N_{crit}=11.5/(\ln M)^3$, one mode can completely separate off from the others, allowing a very wide latitude in which to design unstable resonators for single mode operation. It has been observed by Horwitz[30] that above N_{crit} the separation will last for several cusping points, after which another mode will have a lower loss for several cusping points; this pattern continues as N_{eq} is increased. No such separations have been observed for unstable resonators with circular mirrors.

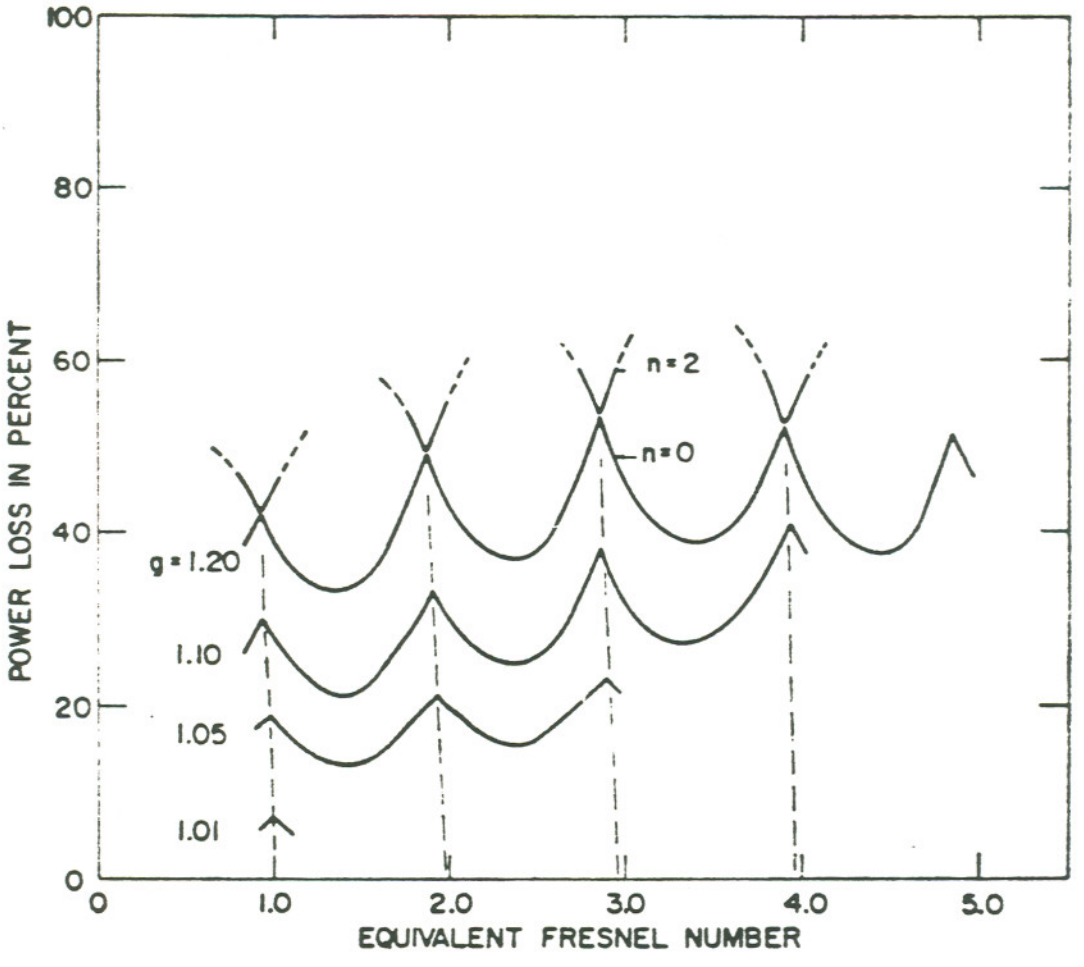

Figure 2.4 — Loss per bounce versus equivalent Fresnel number for various unstable resonators (after Ref. 28).

2.3 Loss Calculations for Multiple Modes

Although knowing the lowest mode loss for a given value of N_{eq} is of interest, more information is necessary for the practical design of unstable resonator lasers. When a laser is brought to its lasing threshold, the gain is clamped at its threshold value, which is equal to the loss of the lowest-loss lasing mode. If there are other modes with losses at or near that of the lowest loss mode, then they can reach threshold as well, and the laser will either run in several modes or hop from mode to mode. Since it is required that only one lateral mode be operating to achieve spatial coherence and a diffraction-limited far field pattern, the laser should be designed so that one mode will have a large loss separation from all the others.

A more complete picture of the mode losses for symmetric unstable resonators was offered by several authors. The approach of Sanderson and Streifer[31] was similar to that of Fox and Li, but instead of iterating the propagation integral many times until a stable solution was found, the integral was treated as an eigenvalue equation, from which the normal modes E_n were found, each with a mode loss eigenvalue γ_n. Siegman and Miller[32] extended this work by employing the Prony method, an approximation that reduces the size of the matrix that must be solved. Typical results from these two papers are shown in Figures 2.5 and 2.6, respectively.

The main observations about these figures are that the curve of lowest loss

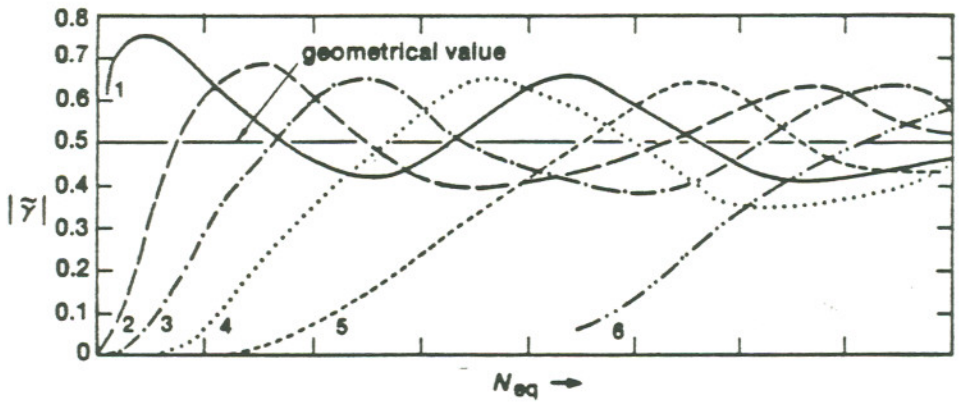

Figure 2.5 — Loss eigenvalue γ versus equivalent Fresnel number for a circular mirror unstable resonator with M = 2 (after Ref. 32).

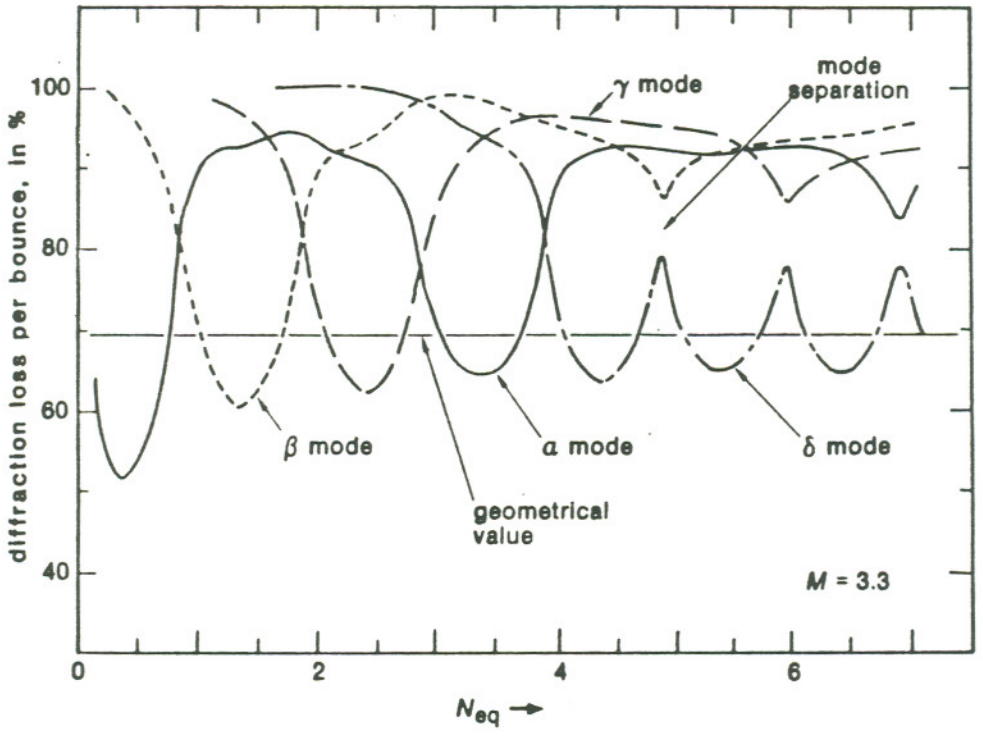

Figure 2.6 — Loss per bounce versus equivalent Fresnel number for a strip mirror resonator with M = 3.3 (after Ref. 31).

shows cusps, with increasing N_{eq}, similar to those of Figure 2.4, and that the losses of the different modes exchange their relative ordering with increasing N_{eq}. Furthermore, some places on the curve are crossing points between modes, while in other places the mode separation is relatively large, demonstrating that in this analysis, a resonator could in principle be designed to operate in a single mode.

Other analytical techniques, such as coupled-mode analysis[33], asymptotic theory[30], and virtual source theory[34] have also been employed to study unstable resonators, but will not be discussed here. A review of unstable resonator theory can be found in the book by Siegman[35].

2.4 Analytical Model Including Gain

Unfortunately, the models discussed in the last section are still not sufficient to simulate the operation of an unstable resonator semiconductor laser. The preceding analysis of the passive resonators may have provided a starting point into understanding the workings of active semiconductor laser resonators, but we cannot automatically expect the previous results to remain strictly valid.

One limitation is that in an actual operating laser, the gain process introduces a complex component into the index of refraction, and for semiconductor lasers, which have a relatively high gain, this is especially important. Another limitation, as mentioned in Section 2.1, is that the preceding analyses assumed an infinite width medium and a finite width mirror. In a semiconductor laser, the propagating wave is guided laterally, either by a complex index step, as in gain-

guided lasers, or a real index step, as in index-guided lasers, or both, and the mirror can be either wider or narrower than the lateral confinement region.

A formalism including these new elements[18,36,37] has been presented by Lang, Salzman, Mittlestein, and Yariv. In this formulation, the electric field inside the laser is represented as linear combination of the complete set of modes of the lateral waveguide, which can be expressed by

$$E(y,z) = \sum_n a_n u_n \tag{2.10}$$

where $\{a_n\}$ are the amplitudes of the basis set $\{u_n\}$.

The field E(y,z) can then be represented by a column vector A with components $\{a_n\}$, and propagated around the resonator by operating on it with a complex propagation matrix $\mathbf{P}(L)$, a complex mirror coupling matrix $\mathbf{R}_1$, $\mathbf{P}(L)$ again, and another mirror coupling matrix $\mathbf{R}_2$. The normal modes for the laser are then found by requiring that the vector A reproduce itself over one roundtrip. Symbolically this can be written as

$$\mathbf{R}_2\mathbf{P}(L)\mathbf{R}_1\mathbf{P}(L)A = A \tag{2.11}$$

The basis set $\{u_n\}$ is derived analytically by solving the Helmholz equation for a waveguide with three lateral sections: a central gain section with refractive index n_1, between two guiding sections, each with a refractive index n_2. The quantity Δn is defined by $\Delta n \equiv \mathrm{Re}[n_1 - n_2]$ The boundary conditions are chosen to allow "leaky" modes, which diverge far from the gain region, and to ignore "radiation" modes, whose eigenvalues are continuous. The gain and frequency

dependence of the propagation matrix is treated as a first order perturbation, and the problem is finally reduced to the linear eigenvalue equation

$$\left[\mathbf{R}_2\mathbf{P}(\mathrm{L})\mathbf{R}_1\mathbf{P}(\mathrm{L})-\gamma\mathbf{I}\right]\mathrm{A} = 0 \tag{2.12}$$

which is solved by computer matrix routines. The normal modes are then the eigenvectors A, and their losses are the eigenvalues γ.

Figures 2.7 - 2.9 show the loss curves calculated by this formalism for gain guided and index guided semiconductor lasers. In all three figures, the radius of curvature of the curved mirrors is 100 μm, the width of the gain section is 25 μm, and the mirror apertures are assumed to be very large compared to the width of the gain section. In the gain guided regime ($\Delta n = 0.001$), the two modes are separated for cavity lengths above about 25 μm. The authors predict that interference effects between the modes should cause the losses to fluctuate with L with a period of roughly $2\pi/(\beta_n-\beta_l)$, where β_n and β_l are propagation constants for modes n and l, respectively.

In the weak index guiding ($\Delta n = 0.005$) and strong index guiding ($\Delta n = 0.01$) regimes, the relative ordering of the eigenvalues changes many times with increasing cavity length. A modified Fresnel number F′ is defined by

$$\mathrm{F}' \equiv \frac{a^2}{2\lambda \mathrm{L}} \tag{2.13}$$

and loss maxima are predicted when $\mathrm{F}'=\mathrm{N}_1/\mathrm{N}_2^2$, where $\mathrm{N}_{1,2}$ are integers. The predictions for the loss maxima, indicated by the small arrows in the diagrams, agree quite well with the calculated curves.

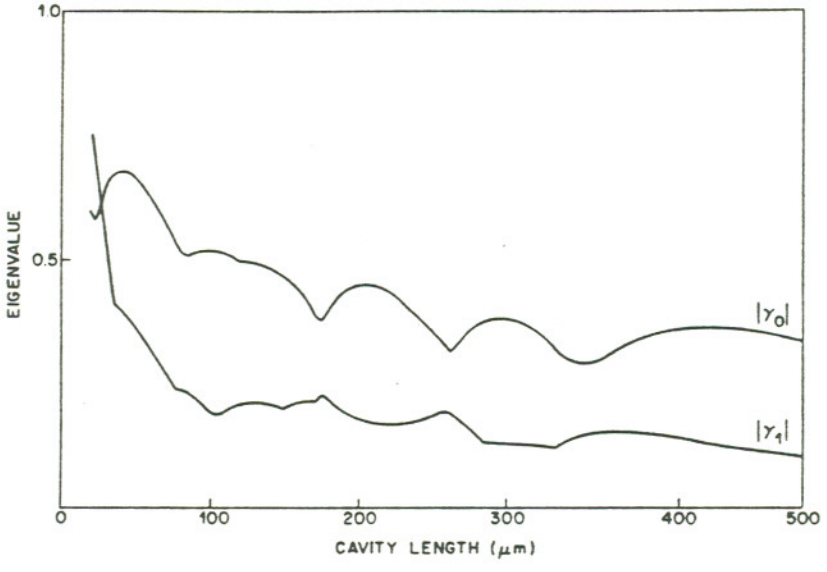

Figure 2.7 — Eigenvalues for the lowest loss modes versus laser length for a gain guided semiconductor laser (after Ref. 37)

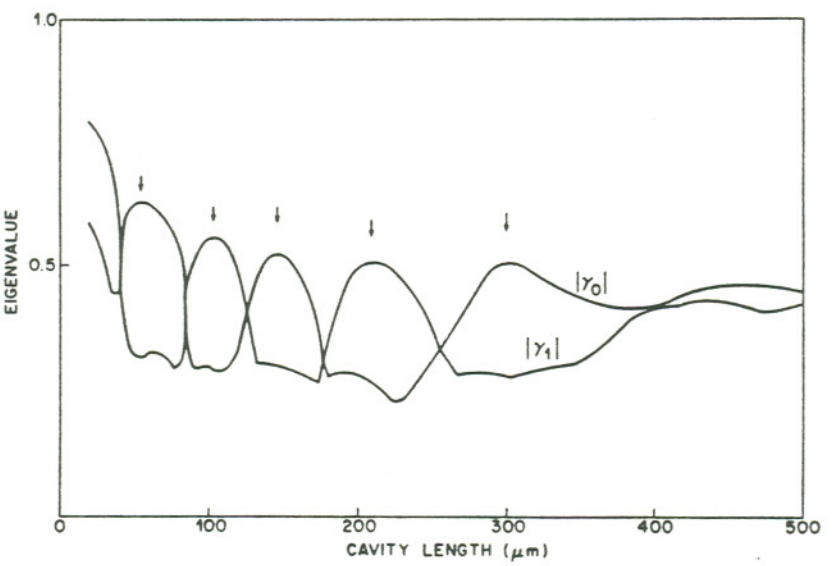

Figure 2.8 — Eigenvalues for the lowest loss modes versus laser length for a weak index guided semiconductor laser (after Ref. 37).

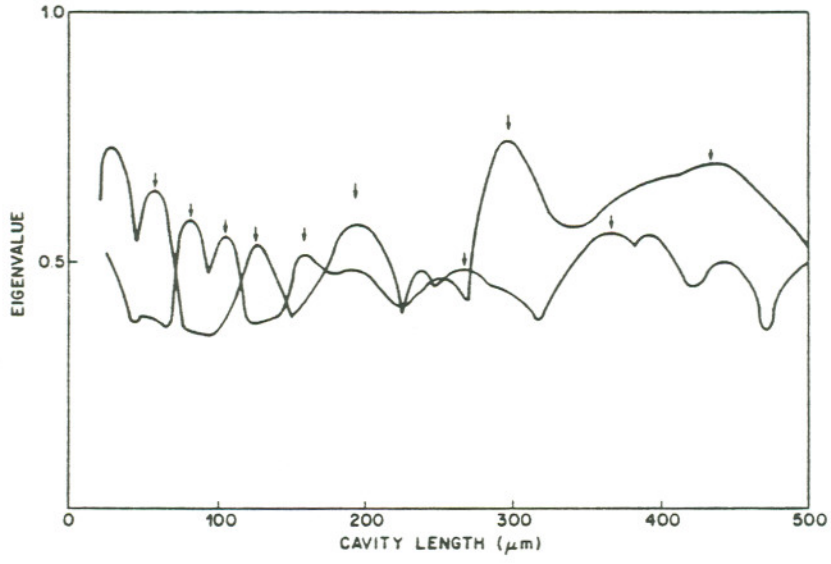

Figure 2.9 — Eigenvalues for the lowest loss modes versus laser length for a strong index guided semiconductor laser (after Ref. 37).

These results further support the possibility of having lateral mode discrimination, and thus single mode operation in unstable resonator semiconductor lasers. However, it must be noted that in all the preceding analyses, only the near field patterns were calculated, and no guarantee is given of laser output in a single-lobed diffraction-limited far field.

Chapter 3
Unstable Resonator Theory — Numerical Approach

3.1 Need for Numerical Model

Although there were differences in the unstable resonator analyses of the preceding chapter — some assumed an infinite width medium with no gain while another assumed a finite width medium with gain — they all calculated the electric field with an analytical approximation based on some form of the Fresnel propagation integral. However, these approximations are limited, since in each case, the laser medium is treated as being uniform over the entire gain region and the optical field is only evaluated at the surfaces of the mirrors. Clearly, if a model of the operating characteristics of a semiconductor laser is to be accurate, it should have realistic representations of the carrier density, gain and loss, and index of refraction, and should calculate those quantities at many points inside the resonator.

The work in this thesis was motivated by the results of Tilton and Depatie[38,39], who created a numerical model which incorporated the above considerations. The model starts with the paraxial wave equation for the vector optical field, E:

$$\left(\frac{1}{2ik}\frac{\partial^2}{\partial x^2} + \frac{1}{2ik}\frac{\partial^2}{\partial y^2} + \frac{\partial}{\partial z}\right)\mathbf{E} = \frac{-1}{2ik}\omega^2\mu_0\mathbf{P} \tag{3.1}$$

The vector electric field **E** is taken to be propagating along the z axis. The y dimension is across the laser stripe, and the x dimension is perpendicular to the junction of the laser. The polarization **P** can be expressed in the form

$$\frac{-1}{2ik}\omega^2\mu_0\mathbf{P} \rightarrow \frac{1}{2}G(x,y,z,|E|^2)\mathbf{E} + ik_0\Delta n_c(x,y,z,|E|^2)\mathbf{E} \equiv g\mathbf{E} \tag{3.2}$$

where G and Δn_c represent position and intensity dependent gain and index change functions, respectively. An effective index approximation[38] removes the x dependence of the field and implies a TE polarization state. The equation is now reduced to the form

$$\left(\frac{1}{2ik}\frac{\partial^2}{\partial y^2} + \frac{\partial}{\partial z}\right)\mathbf{E} = g\mathbf{E} \tag{3.3}$$

A Fourier transform technique is used to evaluate Equation (3.3) . In this technique, the electric field is taken to be periodic, such that

$$\mathbf{E}(y,z) = \mathbf{E}(y+a_y,z) \tag{3.4}$$

so it can be represented as a Fourier expansion in the form

$$\mathbf{E}(y,z) = \sum_{n=0}^{N_y-1} \phi_n(z)\, e^{\frac{i2\pi yn}{a_y}} \tag{3.5}$$

The problem is made discrete in y by defining $y_m \equiv m(a_y/N_y)$, yielding

$$\mathbf{E}(y_m,z) = \mathbf{E}(m,z) = \sum_{n=0}^{N_y-1} \phi_n(z)\, e^{\frac{i2\pi nm}{N_y}} \tag{3.6}$$

When gain and index variations are included, for each value of y the field is pro-

pagated from z to z + Δz by

$$E(y,z+\Delta z) = \sum_{n=0}^{N_y-1} \phi_n(z+\Delta z)\, e^{\frac{i2\pi yn}{a_y}\Delta z \cdot g(y,z)} \tag{3.7}$$

where

$$\phi(z+\Delta z) = \phi(z) \cdot e^{\frac{-i\pi\lambda n^2}{a_y^2}\Delta z} \tag{3.8}$$

Here λ is the free space wavelength.

The carrier density, N, is linearly related to G and Δn_c by

$$G = A \cdot N - B \tag{3.9}$$

$$k\Delta n_c = \alpha \cdot \frac{G}{2} \tag{3.10}$$

where A is the gain coefficient, and B and α are constants, and N is related to the current density J by the steady-state rate equation

$$D_e \frac{d^2N(y,z,t)}{dy^2} - \frac{N(y,z,t)}{\tau_s} - \frac{G\Gamma}{h\nu}\left[I_f(y,z) + I_b(y,z)\right] + \frac{\eta J(y,z)}{qW_a} = 0 \tag{3.11}$$

where D_e is the effective carrier diffusion constant, W_a is the active region thickness, Γ the optical confinement factor, η a current injection efficiency factor, and I_b and I_f the intensities of the forward and backward traveling waves. This equation can be approximated by a finite-difference equation and solved with a Crank-Nicolson algorithm[40], in a manner similar to that described in detail in Section 3.4 .

The program used by Tilton modeled unstable resonators with one planar mirror and one curved mirror and calculated the laser output from the curved

mirror, since it was a modified version of a program that modeled unstable resonator gas lasers of that configuration. The curved mirror is represented as a complex phase factor, such that

$$E_2(y,z) = r\,E_1(y,z)\cdot e^{\frac{i2\pi}{\lambda R}(y^2-b^2)} \tag{3.12}$$

where r is the facet reflectivity of the field (taken to be 0.56), R is the radius of curvature of the mirror, and b is the half width of the mirror aperture.

3.2 Results of the Tilton Model

The resonator simulated in the initial model, illustrated in Figure 3.1, had a single curved mirror with an aperture of 100 μm, a cavity length of 500 μm, and a gain region width of 100 μm. Many values of the magnification M were tried, and the most uniform near field distributions were observed when M was between 2 and 3. A calculated near field intensity for the case of M = 2, at a simulated current density of 2× threshold, is shown in Figure 3.2 . The distribution is not quite uniform, and has a rough variation across the stripe. The calculated phase distribution for the same resonator, shown in Figure 3.3 , has a smoother curve, and the phase angles range from about 0° at the edges of the resonator to 65° at the center.

Next, the resulting far field of the laser, as emanated from the curved mirror end, was calculated. Since the light from the laser emerges from a convex mirror, it appears to diverge from a localized region known as a "virtual source",

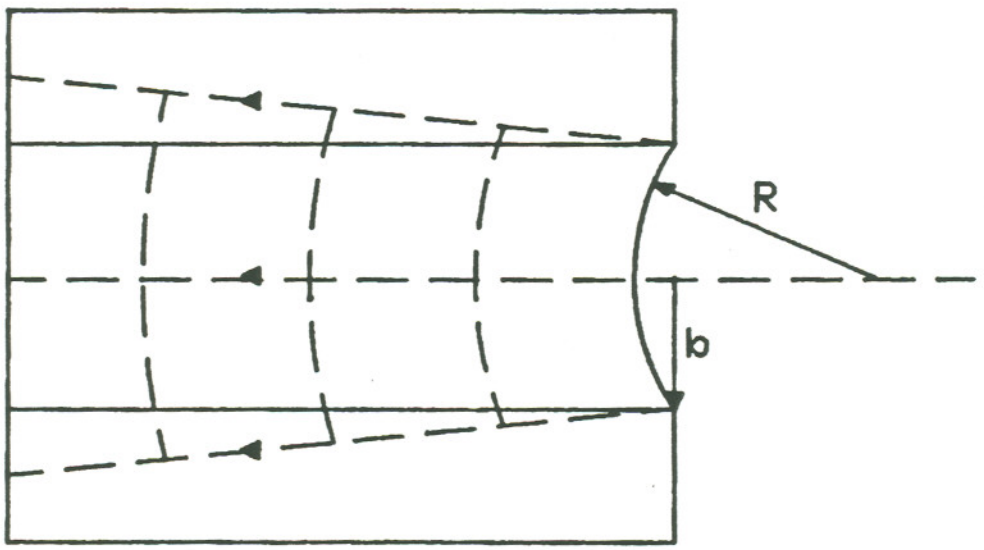

R - radius of curvature
of ion-etched surface

b - aperture radius

Figure 3.1 — Schematic of the unstable resonators modeled by Tilton.

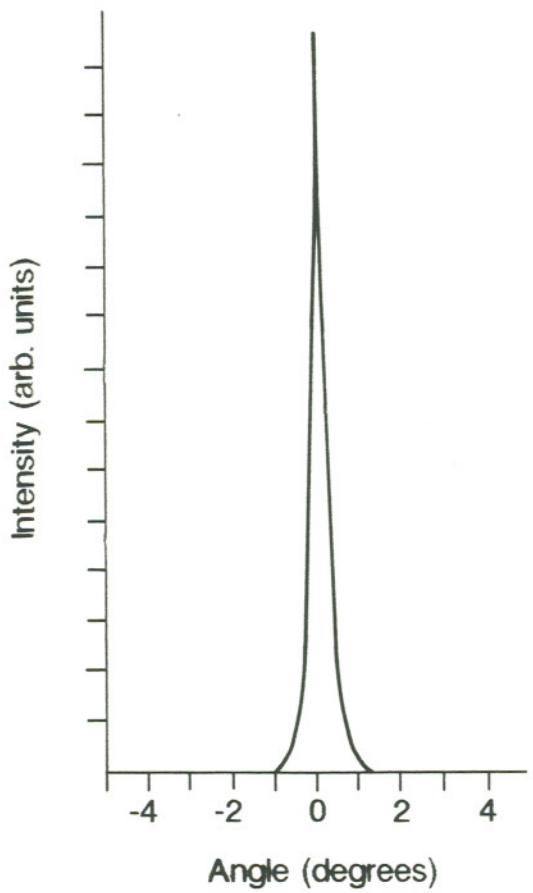

Figure 3.2 — Unstable resonator near field intensity distribution calculated by Tilton. For this model, the mirror aperture was 100 μm, the magnification was 2, and the pumping was at 2× threshold.

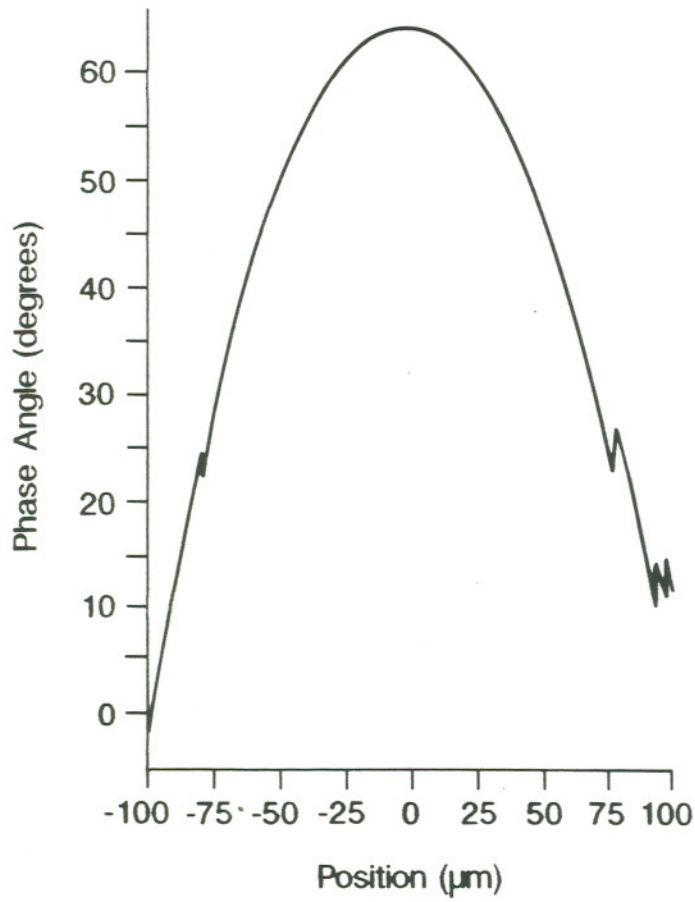

Figure 3.3 — Unstable resonator phase distribution calculated by Tilton. For this model, the mirror aperture was 100 μm, the magnification was 2, and the pumping was at 2× threshold.

located inside the resonator. To make the beam more directional, the divergence was removed by multiplying the complex field by the conjugate of Equation (3.12), in essence reversing the effect of the curved mirror, equivalent to placing a lens in front of the laser. The complex far field was then calculated as the Fourier transform of the complex near field, in a method similar to that described in detail in Section 3.6 .

The calculated far field, shown in Figure 3.4, has a single, narrow lobe with a width of about 0.80° FWHM. For comparison, assuming the aperture is illuminated by a uniform, spatially coherent plane wave, the theoretical diffraction limit for the far field angular divergence is of the order λ/d. For a gain region width $d = 100\mu m$ and a lasing wavelength of $\lambda = 8400$ Å (close to the value measured for the fabricated unstable resonators described in Chapter 5), this comes out to be 0.0084 radians, or 0.48°. The divergence of the far field, then, is only about 1.7 times this diffraction limit.

In subsequent work, the aperture size was changed to see the effect on the calculated near and far field intensity distributions. Otherwise, the modeled lasers were the same as in the preceding analysis. Figure 3.5 shows the near field intensity distributions corresponding to mirror apertures of 150 μm and 200 μm. In both cases, the near fields are much more flat than that of the 100 μm aperture, but there is little difference between that of the 150 μm aperture and that of the 200 μm aperture. Thus, according to the model, an aperture size of at least 150 μm is sufficient for achieving a flat near-field intensity distribution.

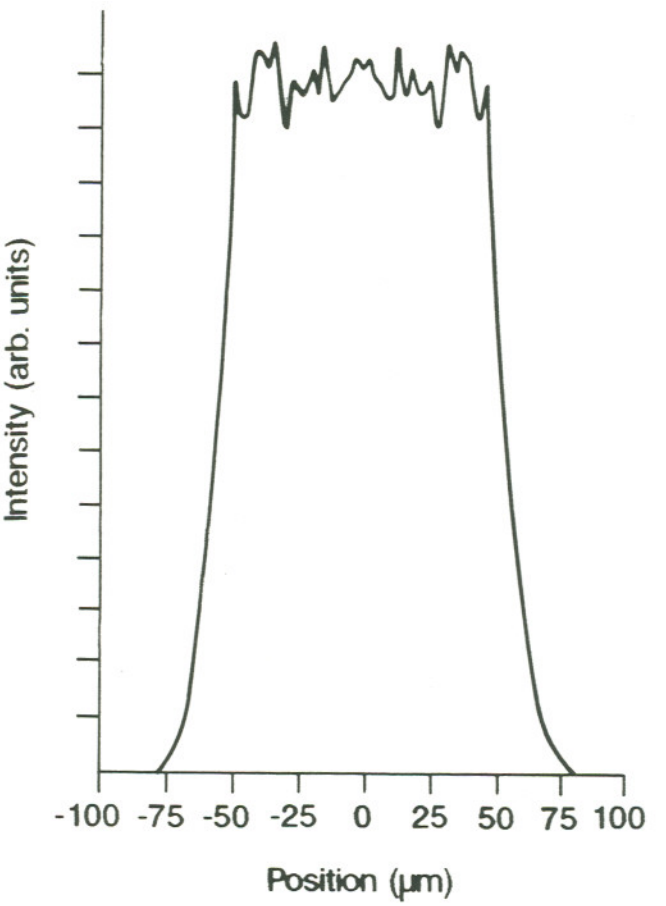

Figure 3.4 — Unstable resonator far field intensity distribution calculated by Tilton. For this model, the mirror aperture was 100 μm, the magnification was 2, and the pumping was at 2× threshold.

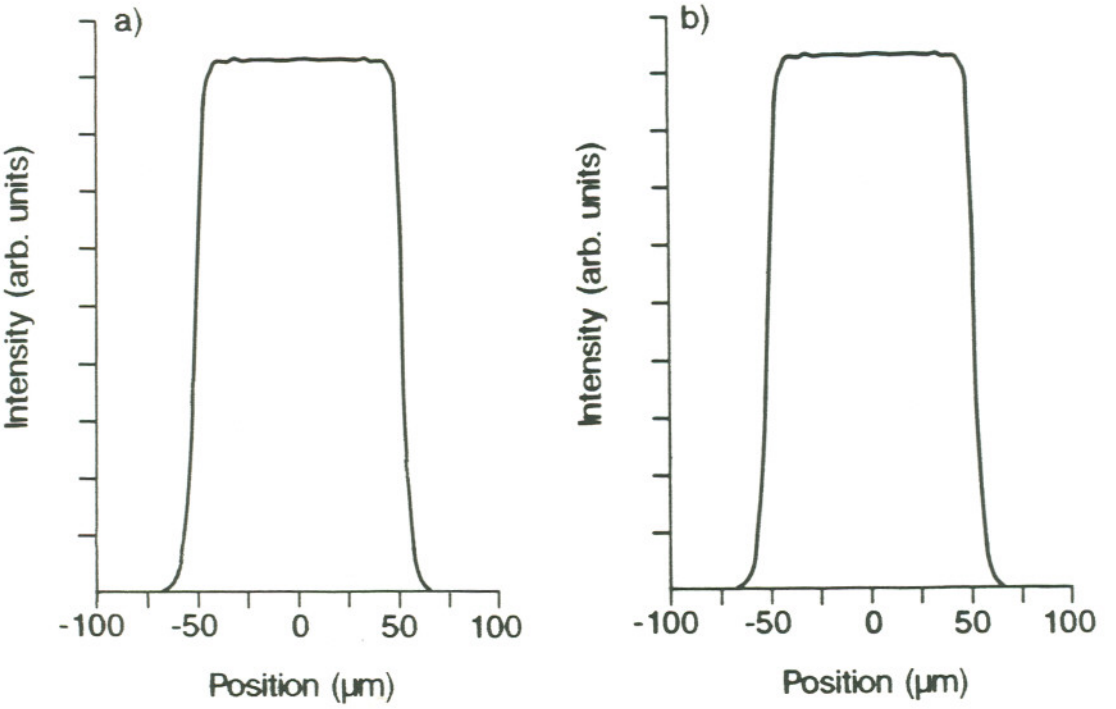

Figure 3.5 — Unstable resonator near field intensity distributions calculated by Tilton. For these models, the mirror apertures were 150 μm (a) and 200 μm (b). In both cases, the magnification was 2, and the pumping was at 2× threshold.

Figure 3.6 shows the calculated far field intensity distributions of the same two resonators. For both the 150 μm and 200 μm apertures, the far fields are also quite narrow, with widths of about 0.80° FWHM. The results presented in this section — the flat near field distributions and the narrow, single-lobed far field distributions — provided a strong impetus to continue work in the modeling and fabrication of unstable resonator semiconductor lasers.

3.3 UNS.FOR — Theoretical Background

A numerical analysis program similar to that of Tilton and Depatie, the Fortran program UNS.FOR, was provided by Weng Chow for use in the investigation of other resonator configurations. The theory motivating the program, discussed in more detail below, starts with Maxwell's wave equation to derive the necessary differential propagation equations. A finite element analysis, described in the following section, is used to obtain the solution for the propagating electric field.

The overall structure of the program is relatively straightforward: an initial field is input into the resonator, propagated toward a flat mirror, reflected off the flat mirror by multiplying by 0.34 (a nominal facet reflectivity for GaAs semiconductor lasers), propagated toward a curved mirror, and reflected. Reflection off the curved mirror is approximated by

$$E_2(y) = r\, e^{-i\phi} E_1(y) \tag{3.13}$$

where

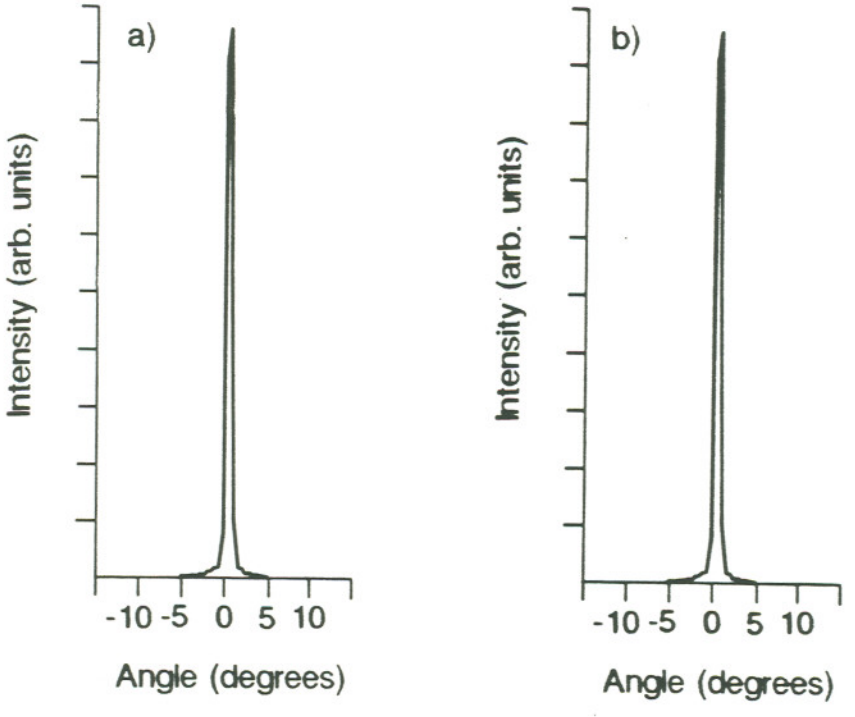

Figure 3.6 — Unstable resonator far field intensity distributions calculated by Tilton. For these models, the mirror apertures were 150 μm (a) and 200 μm (b). In both cases, the magnification was 2, and the pumping was at 2× threshold.

$$\phi = \frac{4\pi Rn}{\lambda}\left[1-\sqrt{1-(\Delta y)^2/R}\right]^2 \tag{3.14}$$

$E_1(y)$ and $E_2(y)$ are the electric fields before and after the reflection, respectively, and $\Delta y(y)$ is the distance between a point on the mirror and the optic axis.

For the work in this thesis, the program, originally written to run on a Cray supercomputer, was modified only minimally to run on the OGI APEE Micro-VAX II: the input was changed so that it could be read from a file rather than from tape, the output was changed so that it would be compatible with our own graphics software, and the control menus were removed so that the program could be run as a background process. The modified program listing is presented in Appendix A .

The following theoretical discussion is taken from private communications with Weng Chow, and from previous work of Chow and Depatie[41,42] that studied filamentation in semiconductor lasers. We begin with the standard Maxwell wave equation

$$\left\{-\nabla^2 + \frac{1}{c^2}\frac{\partial^2}{\partial t^2}\right\}\mathbf{E}(\mathbf{r},t) = -\mu_0\frac{\partial^2}{\partial t^2}\mathbf{P}(\mathbf{r},t) \tag{3.15}$$

$\mathbf{E}(\mathbf{r},t)$ is the propagating electric field and $\mathbf{P}(\mathbf{r},t)$ is the polarization of the medium.

Since in a semiconductor laser the transverse thickness of the active layer is very small compared the lateral and longitudinal dimensions of the laser we can make the approximation that the electric field has a fixed transverse dependence, and choose a two-dimensional field of the form

$$\mathbf{E}(\mathbf{r},t) = \frac{\hat{j}}{2} E(y,z)\, e^{i\phi(y,z)}\, e^{i(kz-\nu t)} + \text{c.c.} \tag{3.16}$$

and a polarization of the form

$$\mathbf{P}(\mathbf{r},z) = \left(P_r(y,z) + iP_i(y,z)\right) e^{i\phi(y,z)} \tag{3.17}$$

Here the dimension y is in the plane of junction of the semiconductor laser, and the dimension z is along the optic axis.

Relations (3.16) and (3.17) are substituted into (3.15) to arrive at the relation

$$\left\{-\frac{\partial^2}{\partial y^2} - 2ik\frac{\partial}{\partial z}\right\} E e^{i\phi} = 2ik\left(\frac{\nu P_i}{2\epsilon_0 cn}\right) e^{i\phi} + 2k\frac{\nu}{2\epsilon_0 cn} e^{i\phi} + k^2\left(\frac{1}{n}-1\right) E e^{i\phi} \tag{3.18}$$

We now define $Ee^{i\phi}$ as the function u, $\nu P_i/2\epsilon_0 n$ as $-G_E E$, where G_E includes gain and loss terms, and define the last two terms on the right side of (3.18) as $2Ekk_0\delta n$, where k and k_0 are the wavenumbers for the medium and free space, respectively, and δn is the carrier-induced refractive index change. Making the substitutions and rearranging terms, we finally arrive at the partial differential equation

$$\frac{\partial}{\partial z} u = \frac{i}{2k}\frac{\partial^2}{\partial y^2} u + \left\{\Gamma(g+ik_0\delta n)-\alpha\right\} u \tag{3.19}$$

G_E and δn have been expanded to include Γ, the optical confinement factor for the active layer, g(x,y), the induced gain, and α, the intrinsic loss, which includes absorption and scattering loss.

3.4 Finite Element Analysis

Equation (3.19) may be solved using the finite element method developed by Crank and Nicholson[40] to solve diffusion-type partial differential equations. In this method, the first and second partial derivatives of a function at a given point in space are expressed in terms of a sum of values of the function at adjacent points. If we evaluate the field at j points across the stripe and propagate the field for n steps along the resonator, the field at any point inside the resonator can be represented by u_n^j, and the finite element equation becomes

$$\frac{u_{n+1}^j - u_n^j}{\Delta z} = \frac{D}{2(\Delta y)^2}\left\{u_{n+1}^{j+1} - 2u_{n+1}^j + u_{n+1}^{j-1} + u_n^{j+1} - 2u_n^j + u_n^{j-1}\right\} + F_n^j u_n^j \quad (3.20)$$

where $D \equiv i/2k$ and $F_n^j \equiv \Gamma(g_n^j + ik_0\delta n_n^j) - \alpha^j$. Letting $a \equiv i\Delta z/4k_0 n(\Delta y)^2$, we group terms with like subscripts, and obtain the formula

$$-au_{n+1}^{j+1} + (1+a)u_{n+1}^j - au_{n+1}^{j-1} = au_n^{j+1} + (1-a)u_n^j + au_n^{j-1} + \Delta z F_n^j \equiv r_n^j \quad (3.21)$$

We now have a way to express the electric field at one propagation step in terms of the field at the previous step.

The program solves for the field u at each propagation step using the matrix equation

$$\begin{bmatrix} (1+2a) & -a & 0 & 0 & \cdots & 0 \\ -a & (1+2a) & -a & 0 & & 0 \\ 0 & -a & (1+2a) & -a & & 0 \\ 0 & 0 & -a & (1+2a) & & 0 \\ & & & & & -a \\ 0 & 0 & 0 & 0 & -a & (1+2a) \end{bmatrix} \begin{bmatrix} u_{n+1}^2 \\ u_{n+1}^3 \\ u_{n+1}^4 \\ \\ \\ u_{n+1}^{j-1} \end{bmatrix} = \begin{bmatrix} r_n^2 \\ r_n^3 \\ r_n^4 \\ \\ \\ r_n^{j-1} \end{bmatrix} \quad (3.22)$$

The program evaluates the field of the propagating wave at 200 points (j superscripts). The field is stored at 200 sheets along the resonator (n subscripts). Between the stored sheets, the field is linearly interpolated at 10 equal intervals, so that a total of 2000 propagation steps can be made on each one-way pass through the resonator.

At each propagation step, the quantities g and δn must be found as a function of the carrier density N. The gain medium is modeled as an ensemble of two-level band-to-band laser transitions, each with different transition energies that are broadened by electron-electron and electron-phonon interactions. N can be calculated as a function of g and the optical intensity I from the relation

$$\xi D\nabla^2 N(y,z) + \gamma_s[N_0(y)-N(y,z)] = \frac{4\pi g(y,z)\, I(y,z)}{h\nu} \tag{3.23}$$

where $N_0(y)$ is the unsaturated carrier density, calculated using a current spreading model of Hakki[43], D is the carrier diffusion coefficient, γ_s is the carrier recombination rate, and ξ is a perturbation parameter.

The solution for N may be found in a power series in ξ:

$$N(y,z) = N_1(y,z) + \xi N_2(y,z) + \cdots \tag{3.24}$$

Substituting (3.24) into (3.23) and equating like powers of ξ, gives, in the first order perturbation

$$\gamma_s\left[N_0(y)-N_1(y,z)\right] = \frac{4\pi g(y,z)\, I(y,z)}{h\nu} \tag{3.25}$$

and

$$N_2(y,z) = L_D^2 \frac{d^2N_1}{dy^2} \left(1+\frac{4\pi I}{\gamma_s h\nu} \frac{dg}{dN}(N_1)\right)^{-1} \tag{3.26}$$

where $L_D=\sqrt{D/\gamma_s}$ is the carrier diffusion length. N_1 can be thought of as the contribution from the interaction of carriers with the laser field, and N_2 the interaction from the diffusion of saturated carriers. At current densities near the threshold current density of the laser, the regime for which this program is designed, the contribution from diffusion is small, so N_2 is neglected.

In the program, a lookup table with calculated values of g and δn for different values of N is read from an external parameter file (also in Appendix A). For each value of I, Equation (3.25) is solved by looking through the table and selecting the values of N and g which most nearly equate the left and right sides of the equation.

3.5 Results of UNS.FOR

The program was run using a resonator length of 450 μm and a stripe width of 100 μm, which were the dimensions of the laser material that was available for machining. The radius of curvature of the curved mirror was set at 2000 μm, so that the magnification (calculated by Equation (2.8) to be 2.61) would be comparable to those used in the Tilton models. The wavelength of the beam was set at 8500 Å, a value near those measured from the fabricated unstable resonator devices, to be described in Chapter 5.

The initial electric field intensity launched into the resonator was essentially

uniform, falling off in amplitude as it extended out of the gain region. The initial phase was set to zero over the whole field. The wave was sent through the resonator a total of 450 roundtrip passes (as far as the program could get in two weeks of allotted running time). The intensity and phase of the resulting mode at the planar mirror was saved in a file each pass for the first 100 passes, and every five passes up to 450 passes.

When an actual operating laser is first turned on, relaxation of the carriers causes the field to undergo transient oscillations before it reaches steady state. Thus, it is desirable that the program run, in terms of the time seen by the propagating wave, for at least a few times the relaxation time constant to ensure that any potential transients have died out. For a pumping level of about twice threshold, the relaxation oscillation frequency is a few gigahertz, corresponding to a period of a few tenths of a nanosecond. Assuming a refractive index for the medium of 3.4, the propagation time for each pass through the resonator is 900 μm $\times$ 3.4 / (3×10^8 m/sec) = 0.01 ns. For 450 passes, the total propagation time is 4.6 ns. Unfortunately, this is not a sufficient length of time to be sure that the relaxation transients to have completely decayed, but since no dramatic oscillations of the field were observed on the relaxation oscillation time scale, we can assume that after a few nanoseconds the effects from relaxation oscillations are small.

Figures 3.7 to 3.9 show the calculated near field intensities for several intervals during its run. The gain stripe is 100 μm wide, and centered at the 150 μm

position on the graphs. For the first few passes (Figure 3.7), the field intensity moves toward the edges of the stripe, as one might expect in an unstable resonator, and then begins to develop a many-peaked pattern. With more passes, the field shows quasi-oscillatory behavior, with intensity maxima that appear to move back and forth with each pass. In figure 3.8, six main peaks are visible, and one can observe that the outer peaks are the highest at pass 45, that the peaks are about the same height at pass 48, and that the inner peaks are the highest at pass 50.

After about 100 passes the variations appear to settle down, and after 450 passes (Figure 3.9) the locations of the principal intensity maxima are more or less fixed, with some variation in the relative heights of the peaks. The fact that there are such peaks at all, however, does not indicate that any lasing filaments are being smoothed out, as was the original motivation of the unstable resonator design.

The calculated phase after 450 passes is shown in Figure 3.10 , and is typical of all the phase plots generated. The curve connecting the points is drawn as if all the absolute angles were between 0° and 360°; one cannot determine how many multiples of 360° the phase of each angle departs from its actual value. The erratic nature of the phase plots is most likely an artifact of an insufficient number of sampling points.

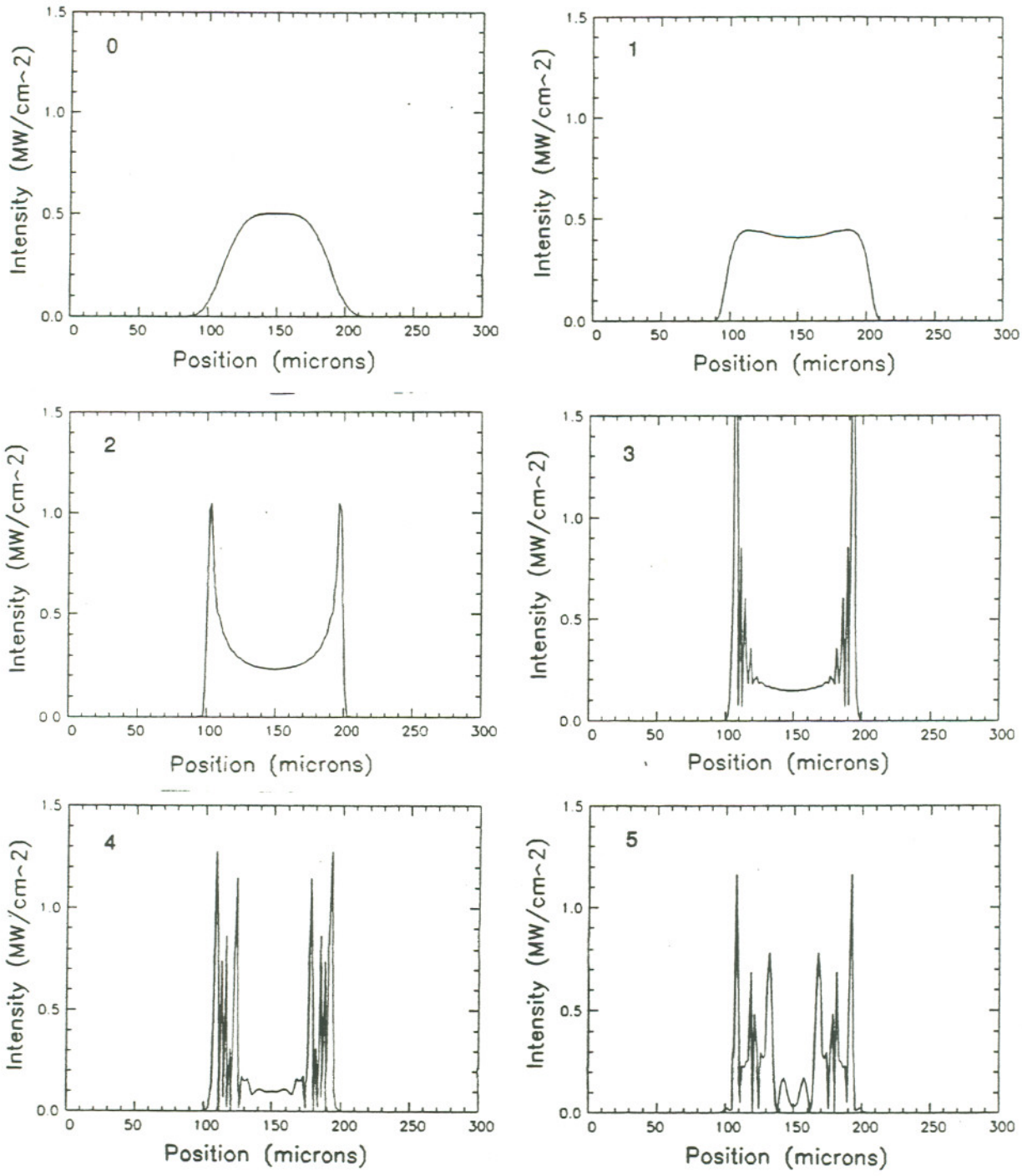

Figure 3.7 — Unstable resonator near field intensity distributions calculated by UNS.FOR for 0 to 5 passes. In this model the magnification was 2.61 and the pumping was at 2× threshold.

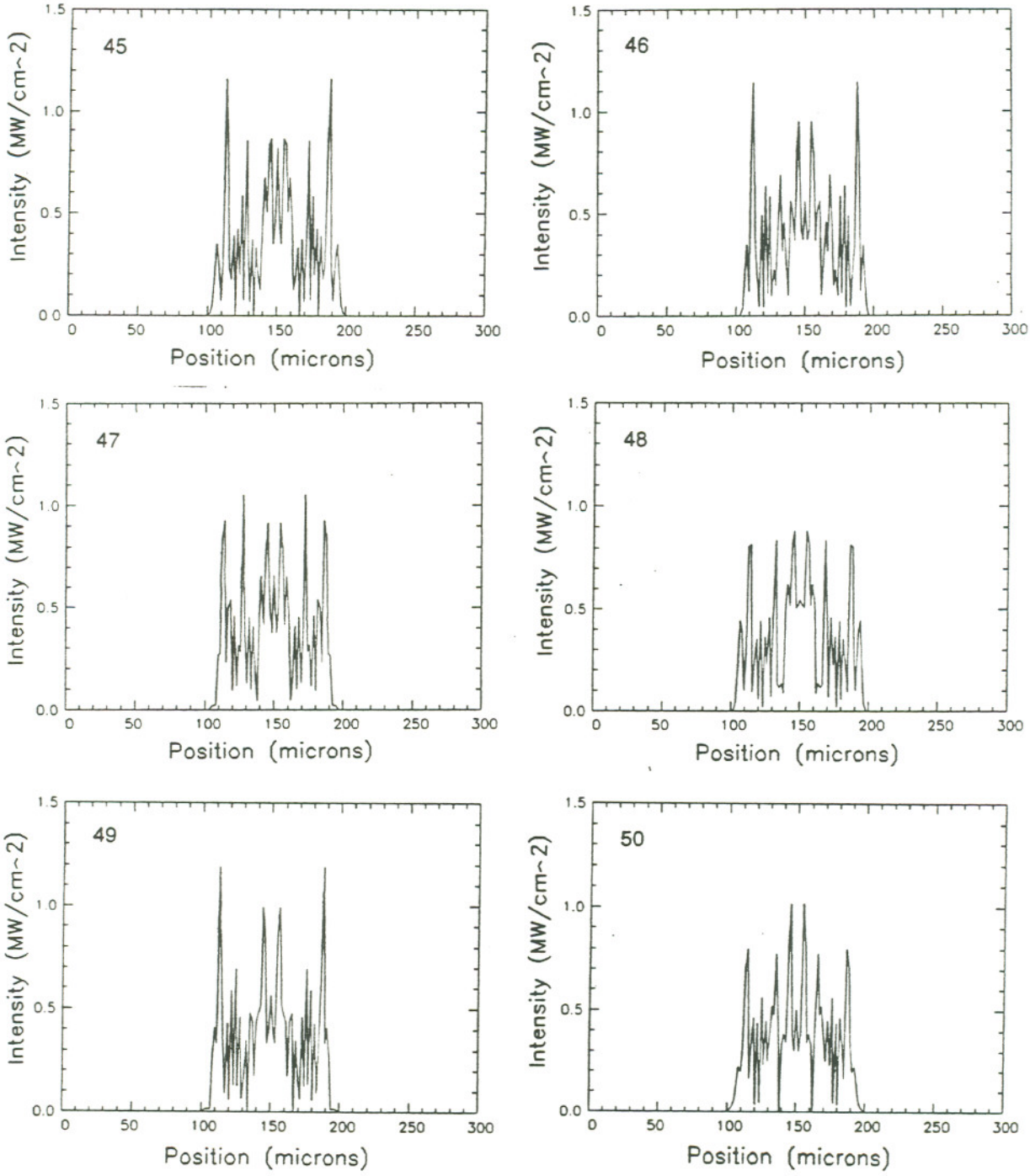

Figure 3.8 — Unstable resonator near field intensity distributions calculated by UNS.FOR for 45 to 50 passes. In this model the magnification was 2.61 and the pumping was at 2× threshold.

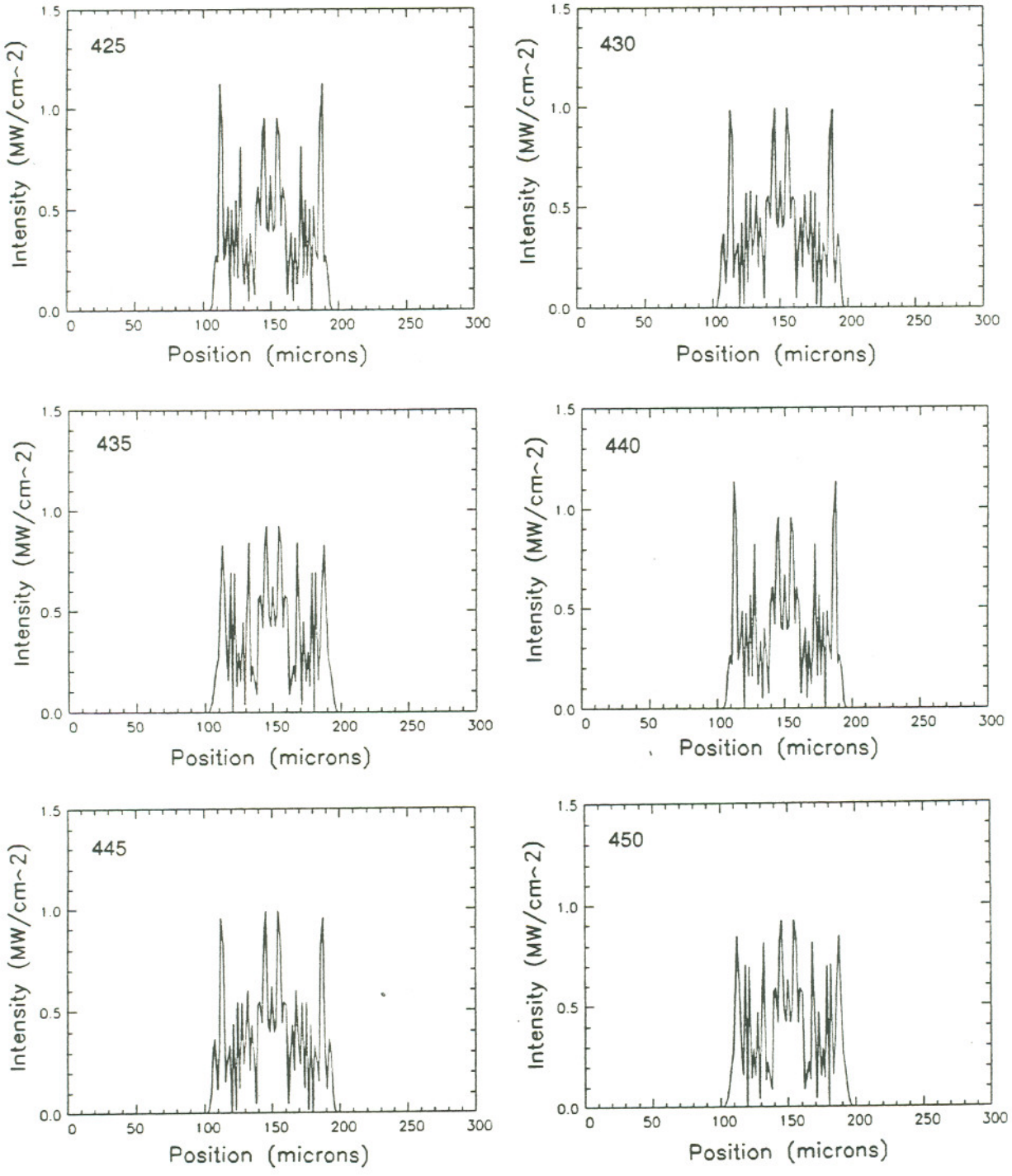

Figure 3.9 — Unstable resonator near field intensity distributions calculated by UNS.FOR for 425 to 450 passes. In this model the magnification was 2.61 and the pumping was at 2× threshold.

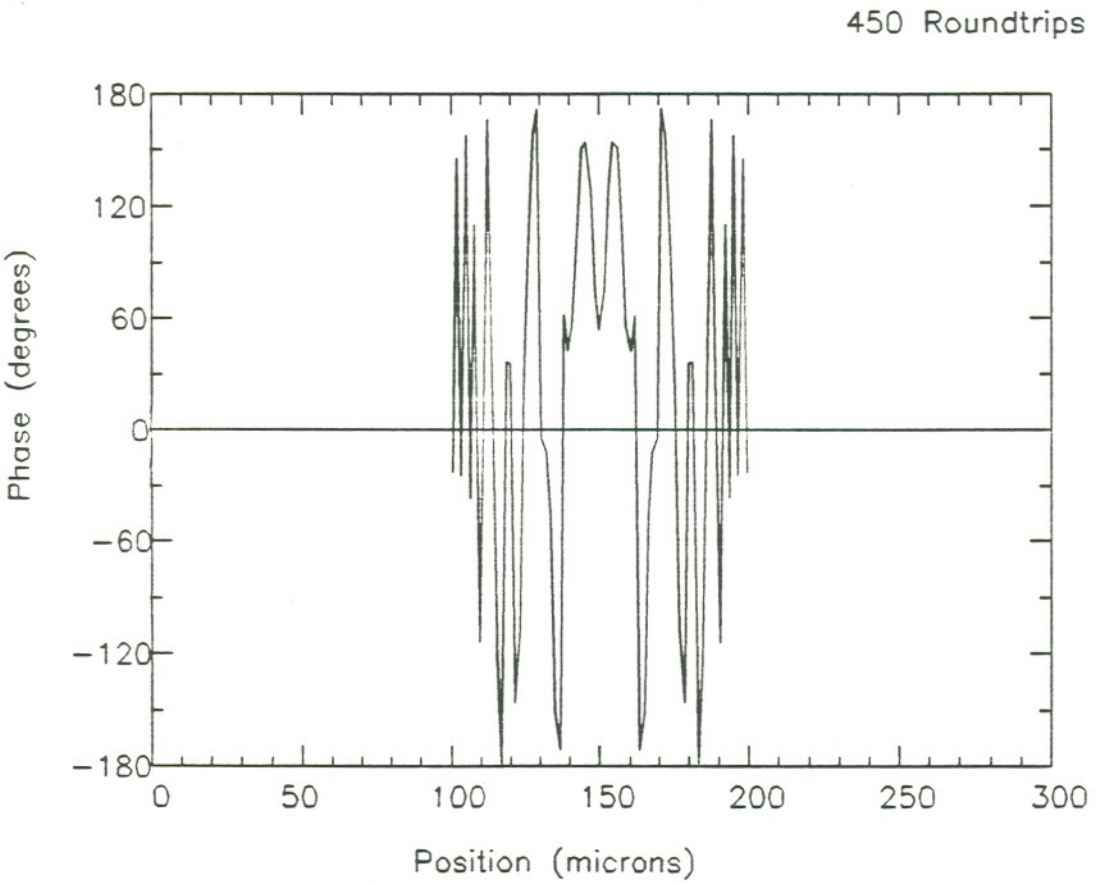

Figure 3.10 — Unstable resonator phase distribution calculated by UNS.FOR for 450 passes. In this model the magnification was 2.61 and the pumping was at 2× threshold.

3.6 Calculation of Far Field

Now that we have the calculated near field pattern for the unstable resonator semiconductor laser, we desire to find the corresponding far field pattern. According to the principles of Fraunhofer diffraction optics, the complex far field can be calculated from the Fourier transform of the complex near field, expressed as the relation[44]

$$P(s) = \int_{-\infty}^{\infty} E(\frac{x}{\lambda}) e^{i2\pi(\frac{x}{\lambda})} \, d(\frac{x}{\lambda}) \tag{3.27}$$

Here we have used a form relating the spatial near field $E(x/\lambda)$ to the angular spectrum $P(s)$, where $s = \sin\theta$. This can also be numerically calculated using a discrete Fourier transform (DFT) routine, defined by

$$\hat{z}_k = \frac{1}{\sqrt{N}} \sum_{j=0}^{N-1} z_j \times \exp\left(-i2\pi j \frac{k}{N}\right) \tag{3.28}$$

where $\{z_j\}$ is the set of N points of the complex initial field, and $\{\hat{z}_k\}$ is the set of N points of the complex transformed field.

The near field output generated by UNS.FOR after 450 passes was transformed by a short computer program (see Appendix A) using the DFT routine C06ECF from the Numerical Algorithms Group (NAG) Fortran library[45]. The calculated far field intensity (Figure 3.11) shows a central lobe with a full width at half maximum (FWHM) of about 7.4°, and two higher side lobes, 3.5° FWHM and 22° apart. If we take the width of the lasing stripe to be d = 100μm and the lasing wavelength to be λ = 8400 Å, then the theoretical

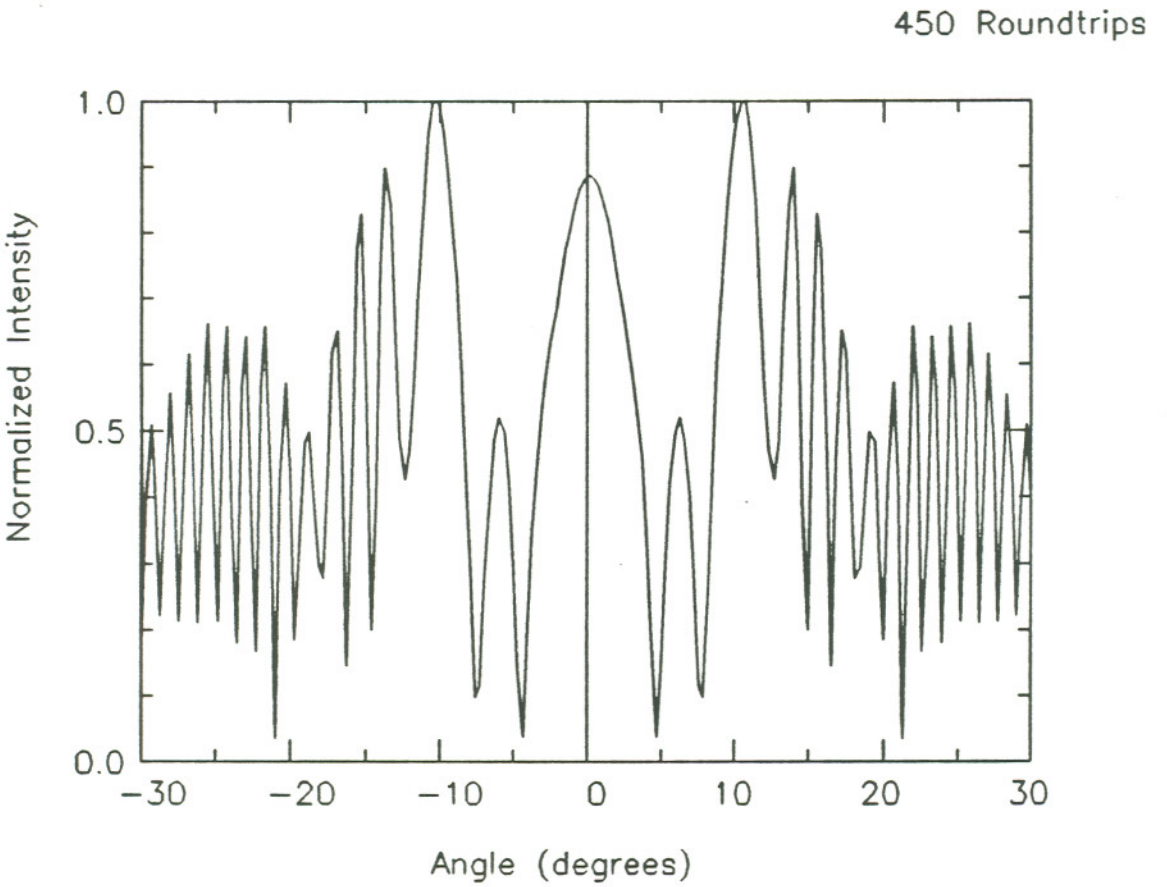

Figure 3.11 — Unstable resonator far field intensity distribution calculated by UNS.FOR for 450 passes. In this model the magnification was 2.61 and the pumping was at 2× threshold.

diffraction-limited angle (assuming a uniformly illuminated aperture) for the far field is of the order λ/d, which is 0.0084 radians, or 0.59°. The wide divergence from the diffraction limit of the far field lobes is attributable to the variations in the intensity and phase of the near field.

Using this model, the calculated far field, then, has neither a single lobe, nor any diffraction-limited lobes. Whether one model is more complete or more accurate than the other is open to question, but ultimately an actual unstable resonator should be fabricated, and its operation compared to theory. Such a device has indeed been fabricated for this thesis, and its fabrication and operation will be described in the following chapters.

Chapter 4
Focused Ion Beam Micromachining

The best way to test the validity of any theories about unstable resonator semiconductor lasers, clearly, is to actually fabricate and test an unstable resonator semiconductor laser. Specifically, the problem that needs to be solved is how to create a curved mirror in the facet of a semiconductor laser. The mirror must be both smooth (feature size $< \lambda/10$) and perpendicular to the substrate over its entire curvature so that the laser can achieve spatial coherence and not suffer excessive mirror loss[18].

4.1 Wet Chemical Etching

The first published attempt at creating a curved mirror in a semiconductor laser is attributed to Bogotov et. al.[15], who used a nylon thread coated with diamond paste to polish a small portion of one facet of a diode laser. Although this fabrication method seems somewhat crude and irreproducible, it was the inspiration for future work. Since then, wet chemical etching has been the method used to create curved mirrors in semiconductor lasers.

Unfortunately, there are two fundamental problems with wet chemical etching of curved surfaces. First, the etched surface is in general not perpendicular

to the substrate. Second, the angle of the etched surface changes with the direction of the mask edge. Both effects occur because the chemical etchant attacks different atomic planes within the crystal at different rates[46]. Since the etch profile also depends on the material being etched, a system of epitaxial layers and etchants can in fact be used[47] to make a vertical wall in one particular mask direction. However, this cannot be done for all mask directions at once, as required for etching curved mirrors.

4.2 Focused Ion Beam System

What is needed to make curved mirrors in semiconductor lasers is a process that that can create a vertical wall in any plane of the crystal. Furthermore, it is preferable that the process be maskless, since this would eliminate the problems associated with undercutting and mask deterioration, and would remove several processing steps. Since the mirrors to be made will be curved, to get a smooth edge the process must be controllable to a resolution of less than 0.01 μm.

One process that meets all these requirements, first mentioned in Chapter 1, is focused ion beam (FIB) micromachining[22,23], which uses a focused beam of ions to precisely sputter away material on a sample, in a pattern defined by a computer control program. As will be discussed in this thesis, FIB micromachining was used to fabricate curved mirrors on the facets of semiconductor lasers, creating unstable resonator geometries. The remainder of this chapter will

describe the FIB system and its operation, and Chapter 5 will report the experimental results of the devices.

The FIB system is shown schematically in Figure 4.1 . The computer sends a series of beam control addresses to a CAMAC crate, a controller for several digital-to-analog converters (DACs). The DAC signals are sent to two ramp generators, whose output is sent to the ion beam controller. Between one of the DACs and one of the ramp generators is a high resolution voltage divider, the purpose of which will be described in Section 4.4 . The ion gun power supply provides the voltages for extracting ions from the ion source and the voltages to focus the beam.

The twin-lens FIB gun, manufactured by FEI Company along with the beam controller and power supply, is illustrated schematically in Figure 4.2 (a single-lens gun was used for the initial experiments, but its operation is similar to that of the twin-lens gun described here). Essentially, it is much like an electron microscope run in reverse: electromagnetic lenses focus a beam of positively charged beam of ions instead of a negatively charged beam of electrons. A gallium liquid metal ion source (LMIS), generates the beam of Ga^+ ions. When the source is operating, liquid gallium flows onto the apex of a tungsten tip, and is held on the tip by a combination of electric and surface tension forces. An extracting voltage induces field ion emission, causing ions to stream off the tip toward the focusing lenses. The first lens focuses the beam onto an adjustable aperture, and a second lens focuses the beam onto the target. Octupole lenses,

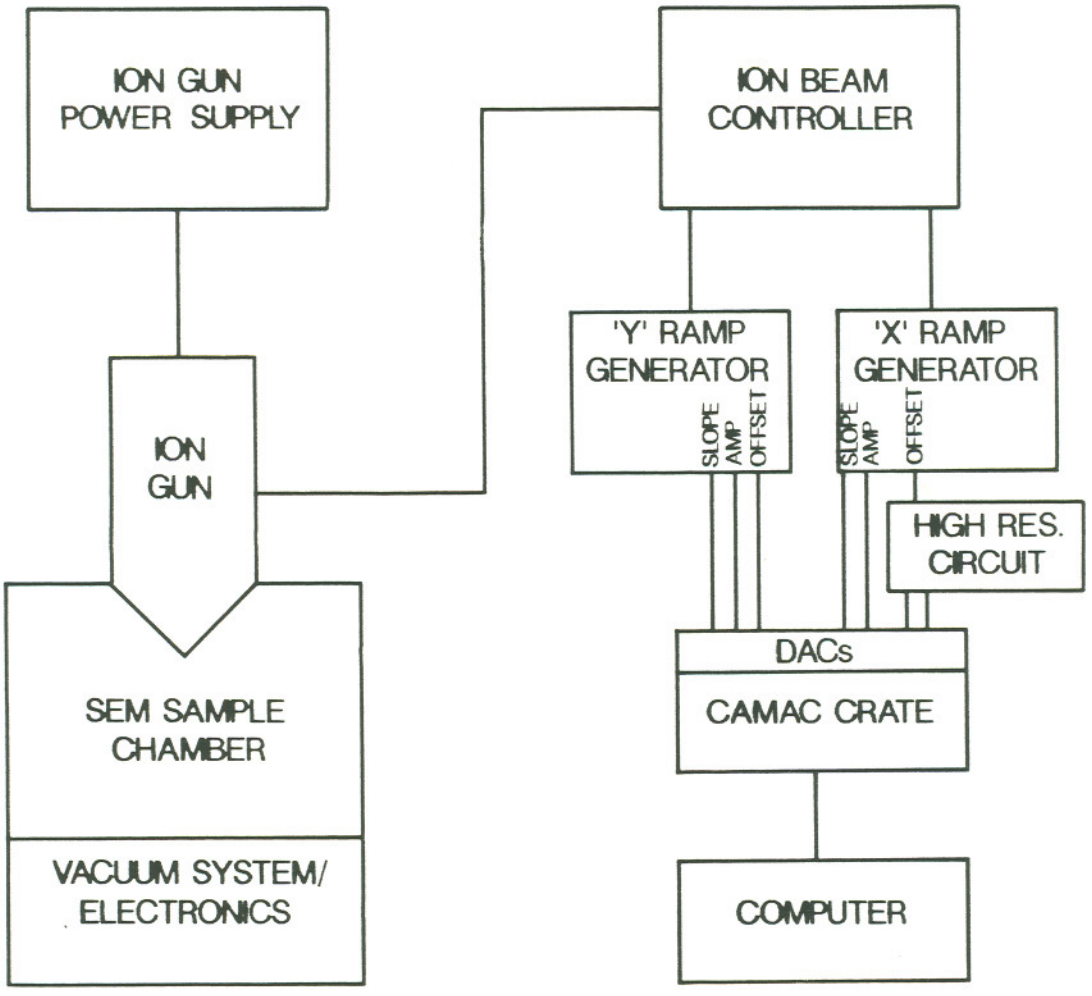

Figure 4.1 — Schematic of the focused ion beam micromachining system.

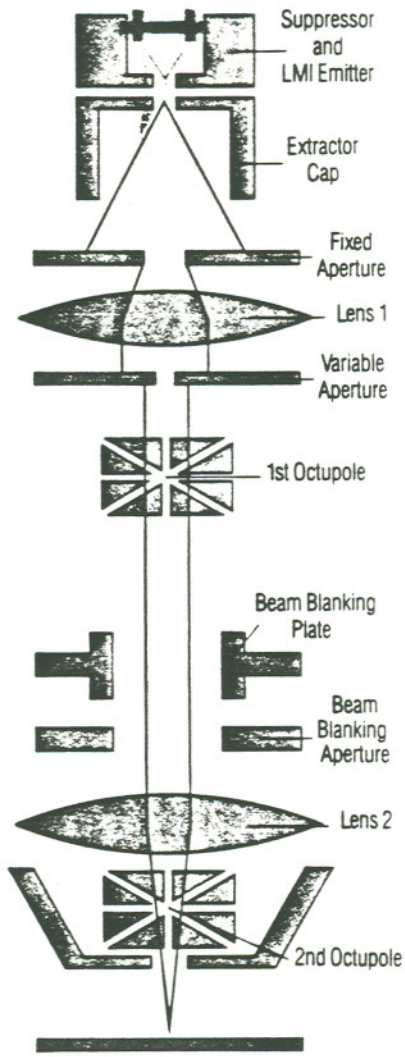

Figure 4.2 — Schematic of the FEI twin lens ion gun.

positioned after each focusing lens, position the beam for either milling or imaging. The size of the aperture and the total working distance determine the spot size and current density of the beam at the target.

The gun assembly is mounted onto the chamber of an Amray Model 1830 scanning electron microscope. A manual gate valve separates the gun chamber from the sample chamber. When the valve is closed, the gun can be kept under vacuum while the sample chamber is open to the atmosphere for loading and unloading samples. When the gate valve is open, a differential pressure aperture keeps the gun at its working pressure ($< 10^{-7}$ torr) even when the sample chamber is at its own, higher working pressure (approx 10^{-6} torr).

4.3 Beam Control Circuitry

The essential features of the beam control programming and circuitry can be understood by describing the function of the ramp generator circuits (Evans Electronics Model 4152). Two identical ramp generators are used, one for each scan dimension ("x" and "y"). Their function is to take input signals sent from the DACs and convert the signals into the form to be used by the ion beam controller. The inputs of the circuit used, defined below, are the "offset", the "amplitude", and the "slope". The ion beam is positioned by the beam controller within a two dimensional-field, with an absolute location defined by the voltage output of each ramp generator. Thus, a constant voltage fixes the position of the beam in that dimension, while a changing voltage sweeps the beam.

Figure 4.3 illustrates the sawtooth waveforms generated by the ramp generators, and the corresponding effects on the position of the beam. For both the x and y dimensions, the difference of the minimum voltage with respect to 0 V is the "offset", the total voltage range of the sawtooth is the "amplitude", and the rate of change of the voltage with respect to time is the "slope". The offset voltage has limits of ± 5 V, and thus allows a limit of 10 V for the amplitude. An adjustable potentiometer sets the maximum value of the slope. For the work in this thesis, the x slope has a maximum of 1 V / 0.1 ms, while the y slope has a maximum of 1 V / 10 ms. The maximum slopes are different for the x and y dimensions so that the beam can sweep out a raster scan.

When both dimensions are controlled independently, and the x and y slopes held constant, points, lines, or rectangles can be scanned, as illustrated in Figure 4.4 . When both amplitudes are set to zero, the beam stays at a single point. When only one amplitude is set to zero, the beam sweeps out a line. A rectangular area is swept out when both amplitudes are non-zero. When the slopes are changed with time, more general shapes can be scanned. For simplicity, however, only line scans were used for the work described in this thesis.

4.4 Beam Control Programming

ARC7.C (listed in Appendix B) was the C language milling program used in these experiments. The program can be organized into three basic parts. In the first part, the CAMAC crate is initialized, the slopes are set to their maximum

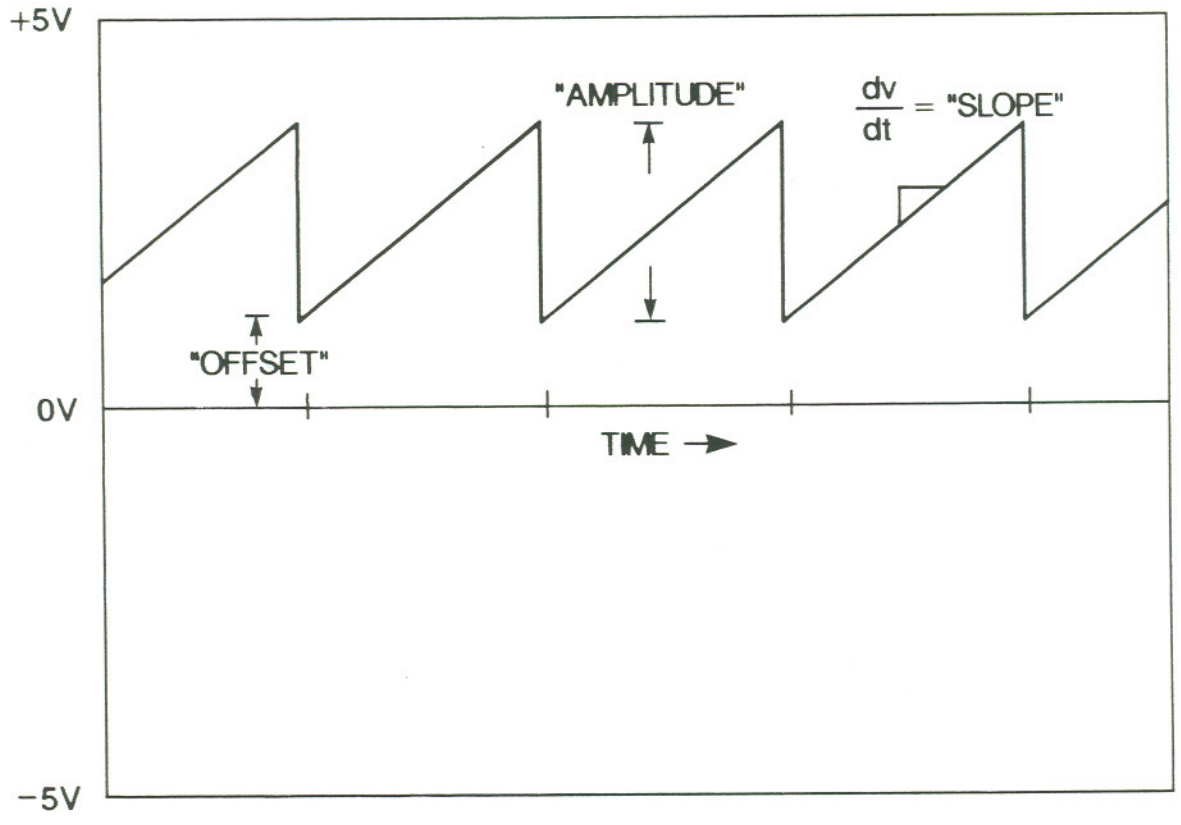

Figure 4.3 — Sawtooth waveforms produced by the ramp generators and their relationship to the beam control inputs.

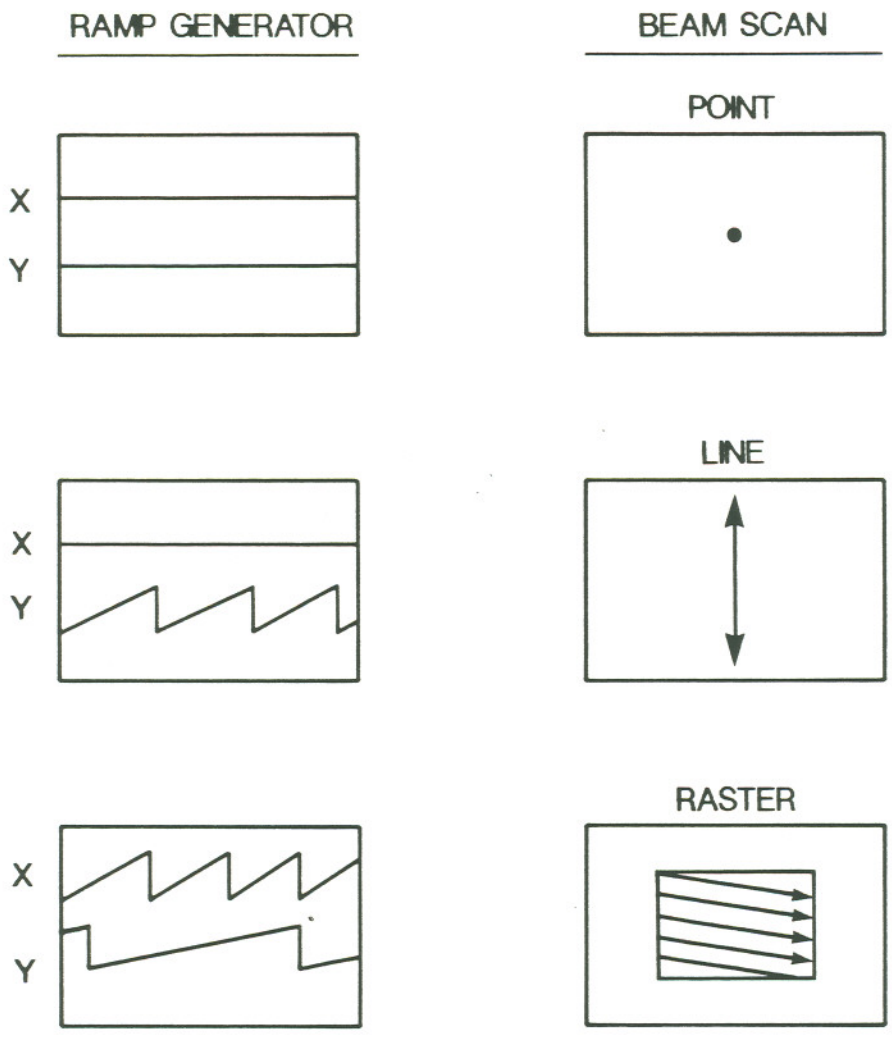

Figure 4.4 — Examples of milling patterns and their relationship to the ramp generator inputs.

values, and the x amplitude is set to zero so that the beam makes y-direction sweeps (vertical lines as seen on the monitor). In the second part of the program, the lengths and milling times of each line scan are calculated and put into lookup tables. The third part of the program is a loop that increments the x position, reads the corresponding y amplitude from the first table, sends the appropriate amplitudes and offsets to the DACs, then waits for the duration read from the second table. When the loop has been executed for the desired number of iterations, the program exits.

To calculate the line lengths and their associated milling times for any particular mirror radius and aperture size, it is helpful to look at the area available to the beam in terms of pixel addresses rather than voltages, since these are the numbers that the program sends to the ramp generators. The total available field of ± 5V in "voltage space" is equivalent to ± 1024 pixels in "pixel space".

Figure 4.5 shows a diagram of the curved area that the program mills out. The three dimensions that need to be determined are the aperture size 2a, the radius R, and the mirror depth d. Given a desired mirror aperture and radius, the mirror depth can be easily calculated using the formula

$$d = R - \sqrt{R^2 - a^2} \tag{4.1}$$

For an aperture of 200 μm and radius 2000 μm, the parameters used for the mirrors described in this thesis, the mirror depth is calculated to be 2.5 μm.

These numbers must then be converted to "pixel space", so the proper sig-

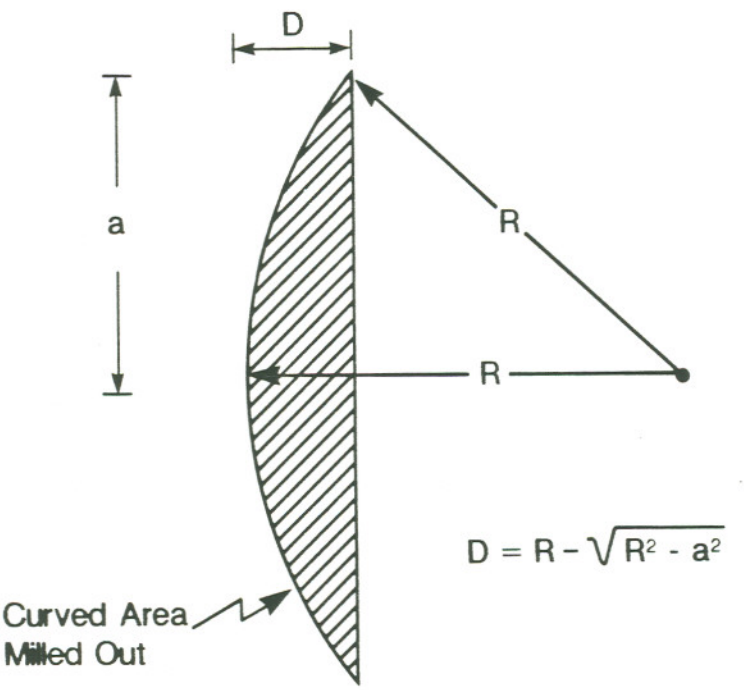

Figure 4.5 — Diagram of the curved area milled by the program ARC7.C . The required input parameters are the aperture size 2a, the mirror depth d, and the radius R.

nals can be sent to the ramp generator, and in turn to the beam controller. The aperture is arbitrarily set at 1500 pixels. In the above case, then, the radius is calculated to be 15000 pixels, and the depth is calculated to be 18.75 pixels. The actual size of the features milled out is determined by the magnification set on the ion beam controller and by the distance of the sample from the ion gun. Calibration is performed either by scaling a sample feature with a known size to markings on the video monitor, or by trial and error, measuring a milled feature later with a calibrated SEM.

The mirror is milled out by a series of overlapping line scans, as illustrated in Figure 4.6 . The length of each line in the y direction changes with position along the x direction to form a curved area. A high resolution voltage divider circuit, described below, increases the effective resolution in the x position to a fraction of a pixel. In all, 500 line scans were made within the mirror region and 200 line scans were made past the end of the aperture. For each iteration of the program loop, two passes of the mirror were made, one in each direction.

The circuit, shown schematically in Figure 4.7, was connected in series between two DACs and the "x" ramp generator, as per Figure 4.1 . The output from one DAC is reduced by an adjustable voltage divider to produce the high resolution signal. This signal is added to a second, undivided DAC so that the high resolution is available to the entire field. The combined output is then sent to the ramp generator controlling the x offset signal.

Figure 4.6 — Pattern of line scans used by the program ARC7.C to mill the curved mirrors. 500 line scans are made on the desired mirror area, and 200 line scans are made past the aperture.

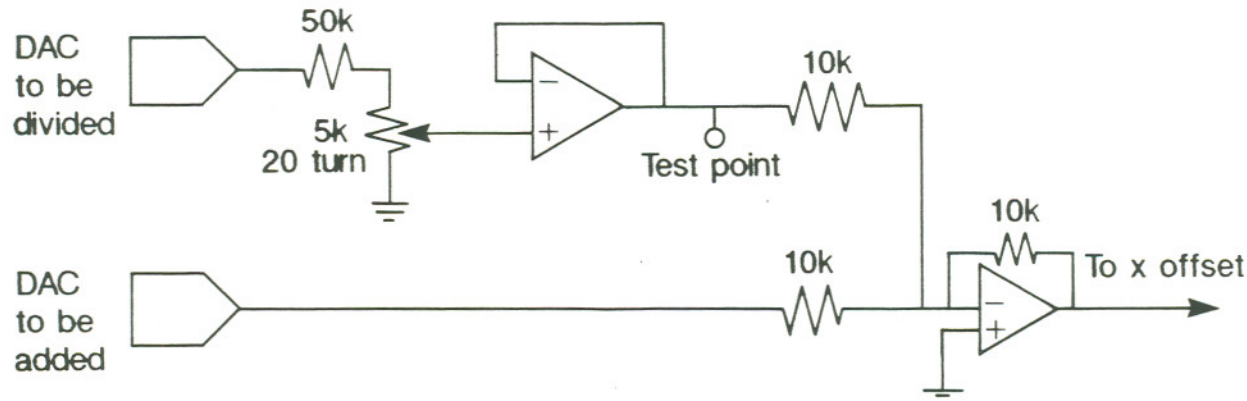

Figure 4.7 — Schematic of the high resolution voltage divider circuit.

The duration of each line scan is determined by simply dividing the magnitude of the y amplitude by ten, and waiting for that number of milliseconds before the x position is incremented. This particular conversion factor was chosen as a tradeoff between two concerns: previous experience had shown that faster scanning of the ion beam produced less gallium redeposition on the samples, but the system time of the computer was only available to a resolution of 10 ms.

4.5 Laser Material Preparation and Milling Procedures

The laser material was grown by metal-organic chemical vapor deposition (MOCVD) by Dan Yap of Hughes Research Laboratories. The epitaxial layer structure incorporated a single quantum well (SQW) within graded index (GRIN) layers. The wafer substrate was GaAs, n-doped to 10^{18} cm^{-3}. The epitaxial layers were: 1.5 μm $Al_{0.6}Ga_{0.4}As$(n−doped $10^{18}cm^{-3}$), 1200 Å lightly n-doped GRIN layer (60% to 20% Al), 80 Å unintentionally doped GaAs QW layer, 1200 Å lightly p-doped GRIN layer (20% to 60% Al), 1.5 μm $Al_{0.6}Ga_{0.4}As$(p−doped $3\times10^{17}cm^{-3}$), and 2000 Å GaAs (p−doped $10^{18}cm^{-3)}$. On top of the epilayers was a 1000 Å layer of SiO_2. The gain section windows, 100 μm wide, 900 μm long, with 100 μm spaces between rows to provide the machining area, were patterned with photoresist and etched with an HF solution. The evaporated metal contacts were Au-Mn on the p-side and Au-Ge/Ni/Au on the n-side.

The wafer material was scribed and cleaved into bars with gain regions that were 450 μm long, and then into pieces of two lasers each (see Figure 4.8). About 15 μm of unmetallized oxide left on the end where the curved mirror was to be machined, since previous experience had shown that machining through metallization had produced poor quality mirrors. Because this area is unpumped, it has a high optical loss, so it should be made as narrow as possible.

The lasers were mounted with a thin layer of conductive epoxy epilayer side up on copper heat sinks. Care was taken to make sure the epoxy was spread smoothly and did not well up over the sides of the laser, since excess epoxy could either short out the device or cause obstruction of the output beam. Furthermore, the laser had to be mounted with the front facet as even with the front of the heat sink as possible, to prevent the reflection of the divergent beam off the top of the heat sink. When the laser was successfully set into the epoxy, the laser, epoxy and heat sink were heated to 125° for two hours, rinsed with acetone and methanol, and blown dry.

Before loading the sample in the chamber, the variable aperture of the ion gun needed to be adjusted to the desired value. For virtually all the work described in this thesis, the fourth aperture was used, producing a beam current of 1000 pA and a spot diameter of 362 nm. Because of an oversight, for two devices the fifth aperture was used, producing a beam current of 4010 pA and a spot diameter of 2010 nm. Fortunately, both aperture sizes produced good quality mirrors — this will be discussed in the next chapter.

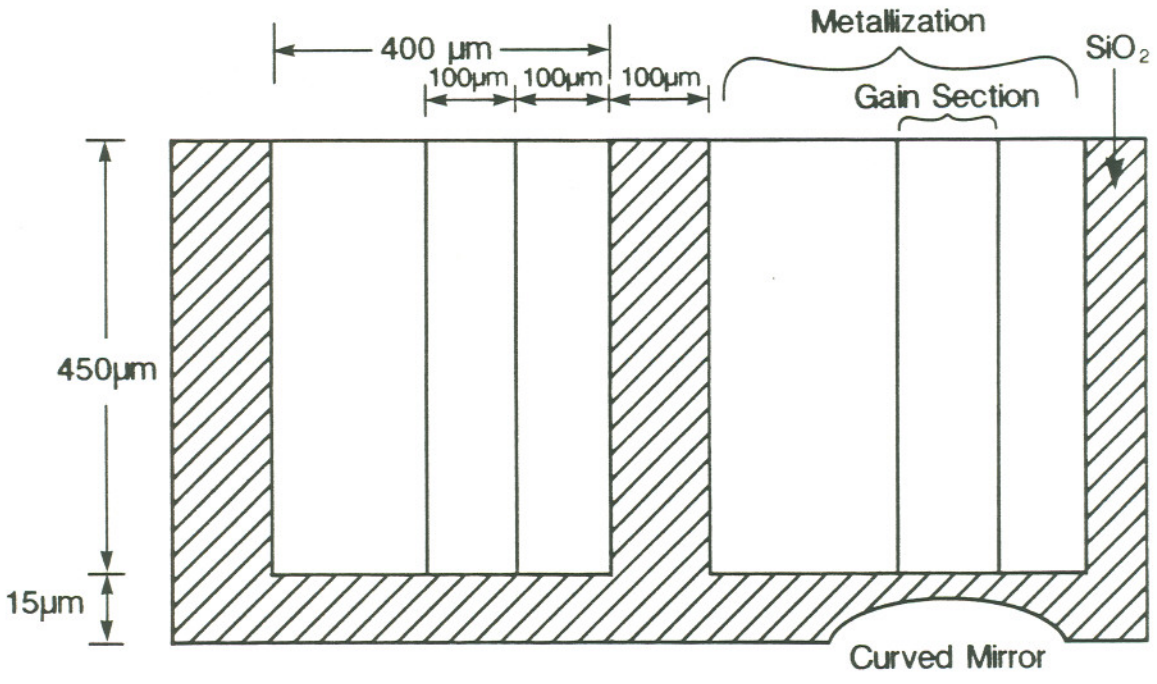

Figure 4.8 — Diagram of the cleaved pieces of laser material.

In preparation for machining, the heat sink on which the laser was attached was screwed onto a small aluminum mount, which was set into the SEM sample stage. After the sample chamber had been sufficiently pumped down ($<10^{-6}$ torr), the ion gun was turned on and set to the proper extraction current (2.5 μA) by adjusting the suppressing and extracting voltages. The isolation gate valve was opened and the laser was moved into position, first using known dial settings for the sample stage and then imaging the laser with the ion beam. The stage was then tilted so that the laser was normal to the ion beam; this was determined by the angle at which the laser facet to be machined was no longer visible.

After the beam was focused, the system was checked for beam drift by milling eight parallel lines for five minutes each on a part of the wafer away from the laser facets. If, after the test pattern was completed, the lines seemed to be uneven, the test was repeated until no more drift was observed. Also, the beam current would often drift from its original value, and would need to be readjusted by changing the beam suppressor voltage. When everything finally appeared to be stable, the section of the laser facet to be machined was positioned to the alignment dots on the monitor.

The program ARC7.C, described above, was used to mill the curved mirrors. By trial and error, it was observed that iterating the milling loop 30 times produced a milling depth of about 10 μm. This was sufficient to machine through all the epilayers, which were about 4 μm thick in total. The total running time

of the program was about 90 minutes.

4.6 Milling Resolution

One of the first technical problems encountered in our experiments with machining curved mirrors in GaAs was the appearance of vertical ridges on the mirror surface, as seen in Figure 4.9 . The mirror was milled with 128 line scans, one per pixel. The ridges, it was decided, were caused by having a insufficient number of line scans.

To solve this problem, a high resolution scan circuit, previously shown schematically in Figure 4.7, was built to increase the positioning resolution in the x direction. The circuit was connected in series between two DACs and the ramp generator, as per Figure 4.1 . The output from one DAC is reduced by an adjustable voltage divider to produce the high resolution signal. This signal is added to a second, undivided DAC so that the high resolution would be available to the entire field. The combined output is then sent to the ramp generator controlling the x offset signal.

The effect of the high resolution circuit can be seen in Figure 4.10 . The mirror radius and aperture size are the same as Figure 4.9 , but the number of line scans was increased from 128 to 500. The mirror is definitely smoother, with little sign of ridges.

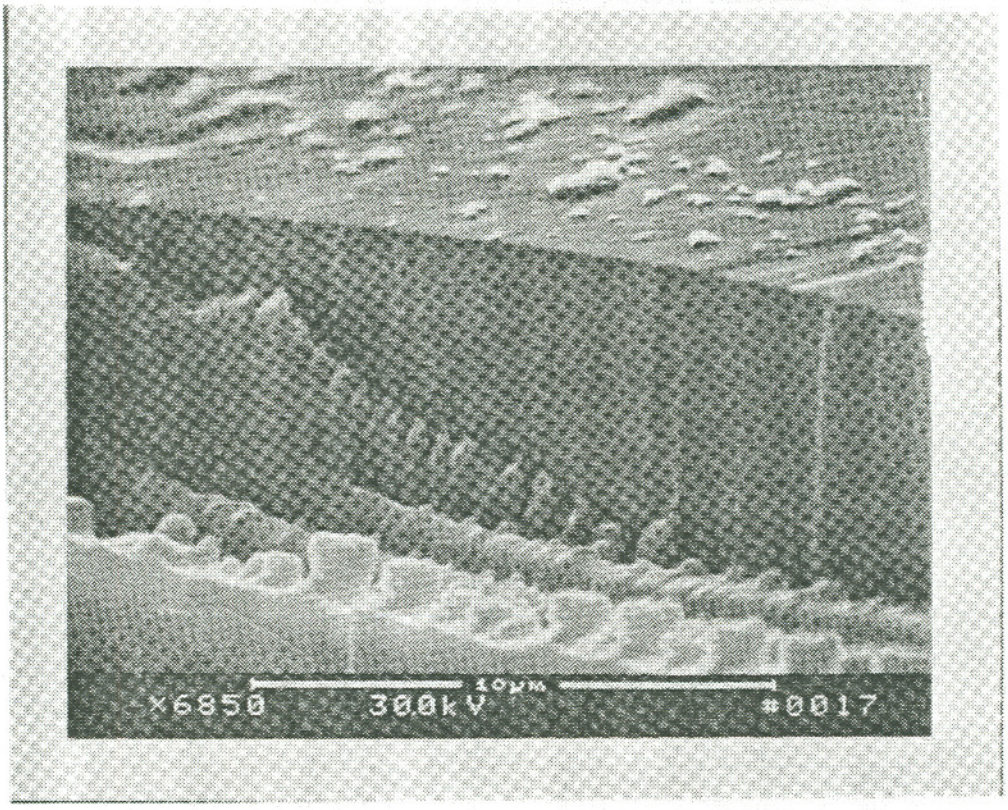

Figure 4.9 — SEM photograph of a mirror machined without the high resolution circuit. The radius of the mirror is 150 μm (photo by Alice Reinheimer).

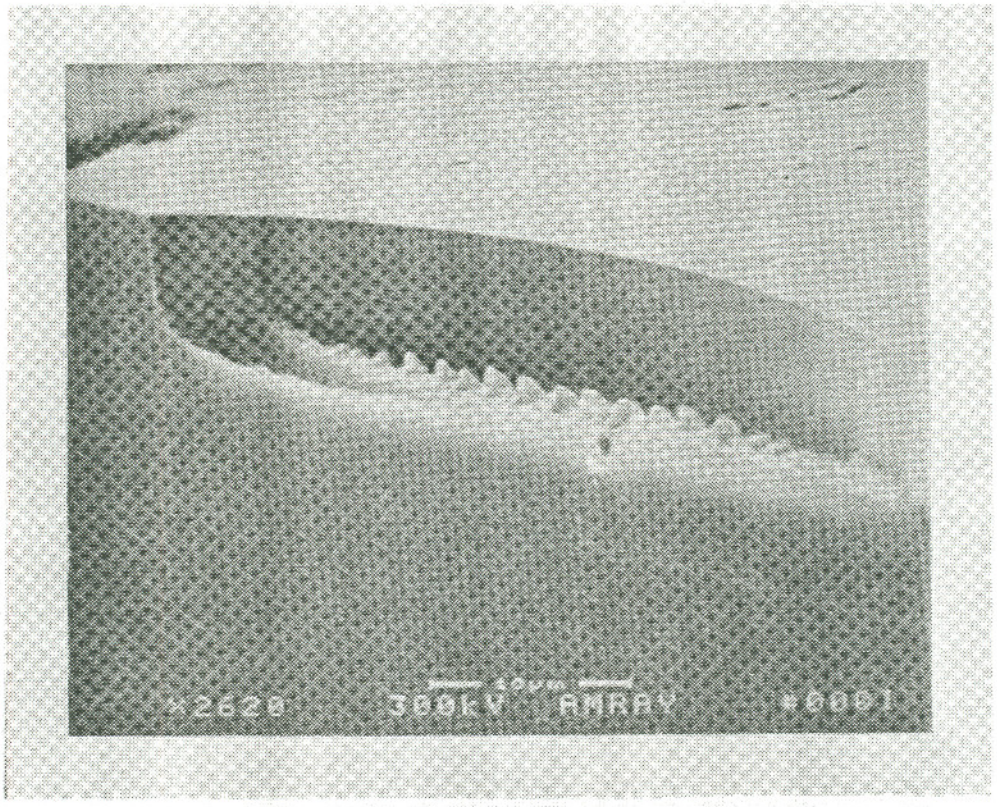

Figure 4.10 — SEM photograph of a mirror machined with the high resolution circuit. The radius of the mirror is 150 μm (photo by Alice Reinheimer).

4.7 Mirror Floor Roughness

One thing that can be seen in both Figures 4.9 and 4.10 is the relatively rough floor of the volume milled out in machining the curved mirror. Although this is not a problem per se, if a section of the floor were high enough it could interfere with the output beam of the laser, so it is preferable to have the floor profile relatively flat.

In initial machined mirrors, it was observed that the mirror floors were higher toward the facet, the opposite of what was desired. Another problem was that the time for each line scan was determined by the execution of a program loop rather than an actual elapsed time, making the results unpredictable. By the final version of the program, the system time of the computer was used to determine the elapsed time for each line scan. Each line scan was milled for a duration proportional to the length the line — 10 ms per 100 pixels seemed to give satisfactory results. Figure 4.11 shows a mirror (radius = 125 μm) milled in GaAs using a program with the new time routine, and one can see that the floor of the milled volume is much smoother than that of the mirror of Figure 4.10 . The drops observed are from Ga redeposition, and are less of a problem when milling the AlGaAs of semiconductor laser material.

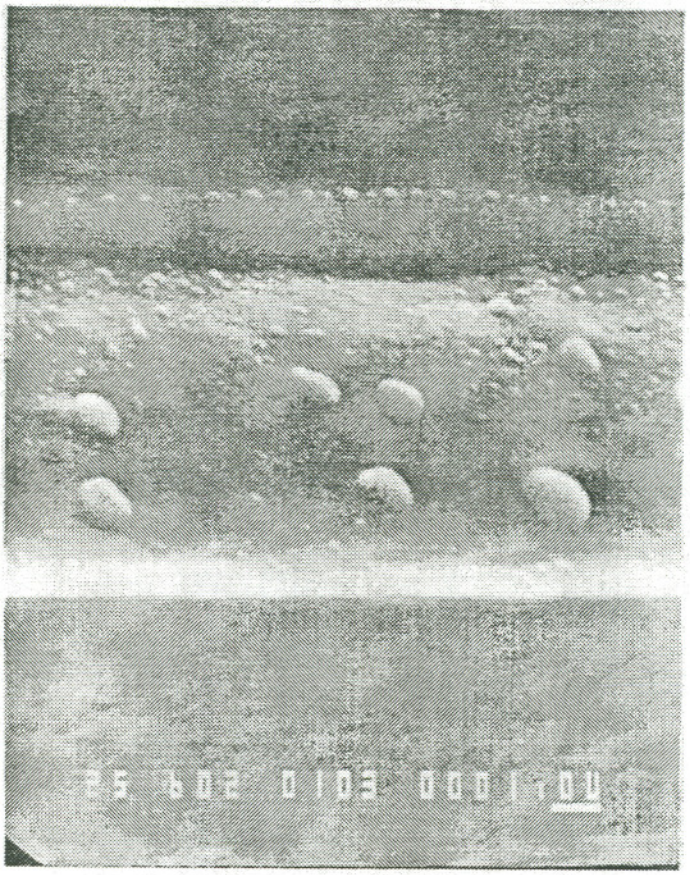

Figure 4.11 — SEM photograph of a mirror machined with a milling time per line scan proportional to the scan length.

4.8 Mirror Alignment

The next problem to be solved was the physical positioning of the mirror at the laser facet, which became more crucial for radii greater than 1000 μm. In the initial programs, the longest scan line, representing the flat edge of the area to be milled, was milled separately. The milled line could then be imaged to see if it had been milled along the laser facet. In addition, alignment dots could be drawn with a pen at the endpoints of the image of the milled line on the monitor screen. Even with this aid, however, many mirrors were still milled away from the mirror edge.

The positioning difficulty is illustrated in Figure 4.12 . For a radius of curvature of 2000 μm and an aperture size of 200 μm, the distance between the curved and flat edges of the mirror is roughly 2.5 μm. Ideally, it would be desirable to position the mirror to within a fraction of a micron. Given that the 200 μm aperture extends about 3/4 of the way across the monitor screen, a length of less than 1 μm is almost imperceptible, much smaller than any alignment dots that can be drawn on the screen.

The solution, as discussed in Section 4.4, was the extra scan lines in the area past the facet. The extra lines that were milled, representing about 1 μm, gave some more latitude in the absolute positioning of the mirror. There was still some uncertainty in position, in practice about ±0.5 μm, which resulted in an uncertainty in the aperture size of about 20% . Since the mirrors were now con-

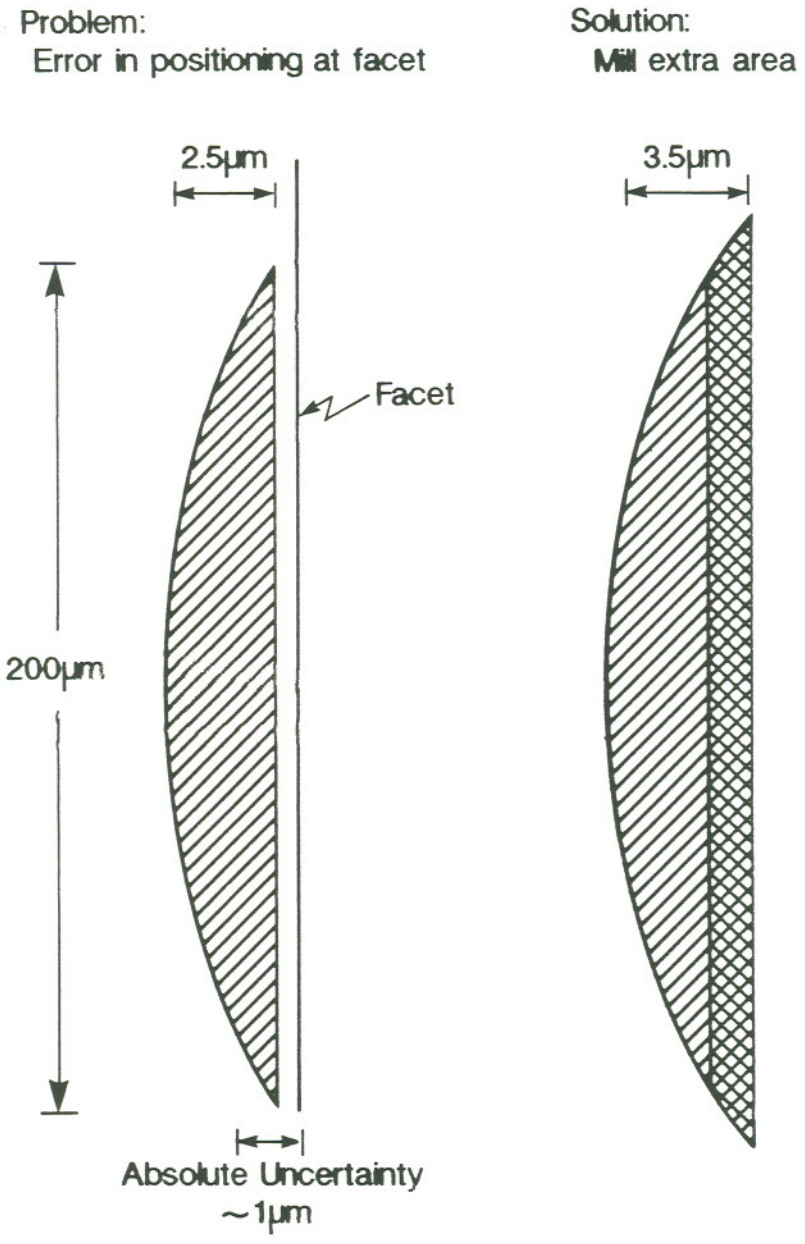

Figure 4.12 — Illustration of mirror alignment problem and its solution.

sistently intersecting the facet, this uncertainty was tolerable.

4.9 Beam Drift

Even after all the problems mentioned in the previous few sections had been identified and solved, machining a curved mirror of acceptable quality in semiconductor laser material remained an elusive task for several months. The mirrors had irregular profiles, slightly different from mirror to mirror. A typical result of that period is shown in Figure 4.13 , where one can see a mirror with a "step" rather than a flat, vertical surface. It was surmised that either the program was milling an incorrect shape or that the beam was drifting back and forth over the course of the total machining time, or perhaps both.

To try to find the source of the drift, the program was run and the signals sent to the beam controller were tested at several points along the the control circuit. First, the DAC addresses generated by the program were sent to a data file and plotted, but the plot still traced out a circular arc. Next, a constant x offset voltage was sent into the high resolution scan circuit, but the output remained constant. Then, x offset signal was measured just before the beam controller, but it oscillated with the required constant amplitude and period.

Since nothing wrong could be found with the control signals, it was hypothesized that the problem had to be with either the gun or the chamber. The long-term beam drift was tested by running the test program at 30 minutes per line, for a total time of two hours. The resulting test pattern indeed

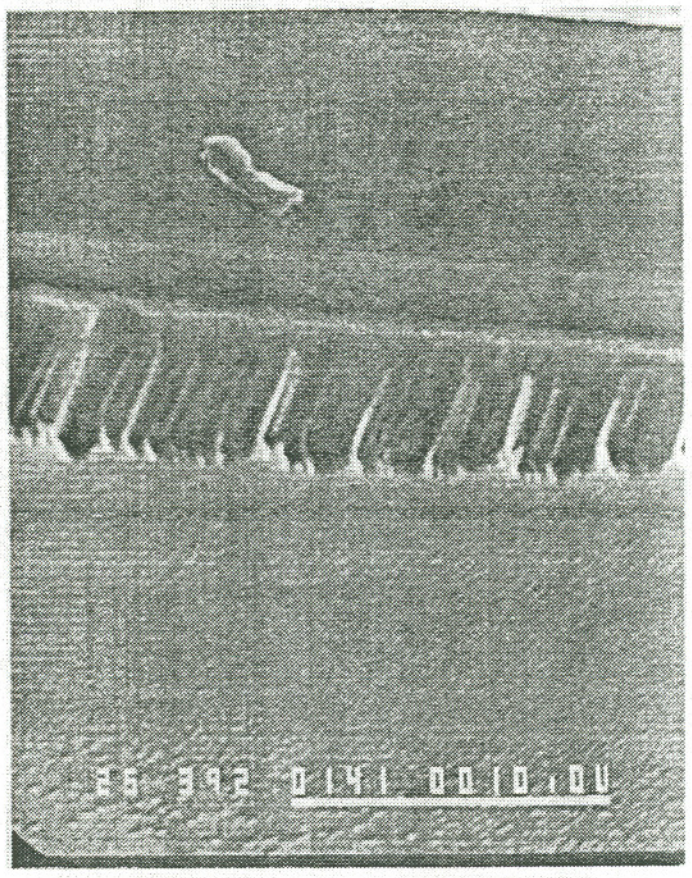

Figure 4.13 — SEM photograph of a mirror milled in the presence of beam drift. The view is the center of the curvature, 45° from vertical.

indicated a slow overall drift of several microns. The cause of the drift was never discovered, but it may have been due to the deterioration of a conductive coating on a non-conductive fitting, creating a charging of the fitting which would affect the positioning of the beam.

As this point, the twin lens gun came back from repairs at FEI, and was installed in the FIB system, along with a new gate valve. The new gun was found to be in proper working order, and similar tests as above showed no drift. Within a week excellent quality mirrors were obtained. The mirrors and their subsequent characterization will be presented and discussed in the next chapter.

Chapter 5 — Experimental Results

5.1 Micromachined Curved Mirrors

For this thesis, four unstable resonator semiconductor semiconductor lasers were fabricated with focused ion beam micromachining. The lasers were identified with the labels A1-#1, A1-#2, A1-#3, and A1-#4, respectively. All four devices were machined with the same procedures, except that for A1-#1 and A1-#2 the fifth aperture was used in the ion gun, with a corresponding spot diameter of 2010 nm, and for A1-#3 and A1-#4 the fourth aperture was used, with a corresponding spot diameter of 362 nm.

Figures 5.1 - 5.4 are SEM photographs of A1-#1. Figure 5.1 is the view of the entire curved mirror, at an angle of 30° from the top view. Figure 5.2 is a magnified view of the mirror, at the same angle. Figure 5.3 is the top view of the entire mirror, and Figure 5.4 is a magnified top view of the mirror. Device A1-#2, not shown here, appears quite similar to A1-#1. Device A1-#4 is shown in Figures 5.5 - 5.8, with the same four views. Device A1-#3, not shown here, appears quite similar to A1-#4.

From the first two photos in each set (Figures 5.1, 5.2, 5.5, and 5.6), we can

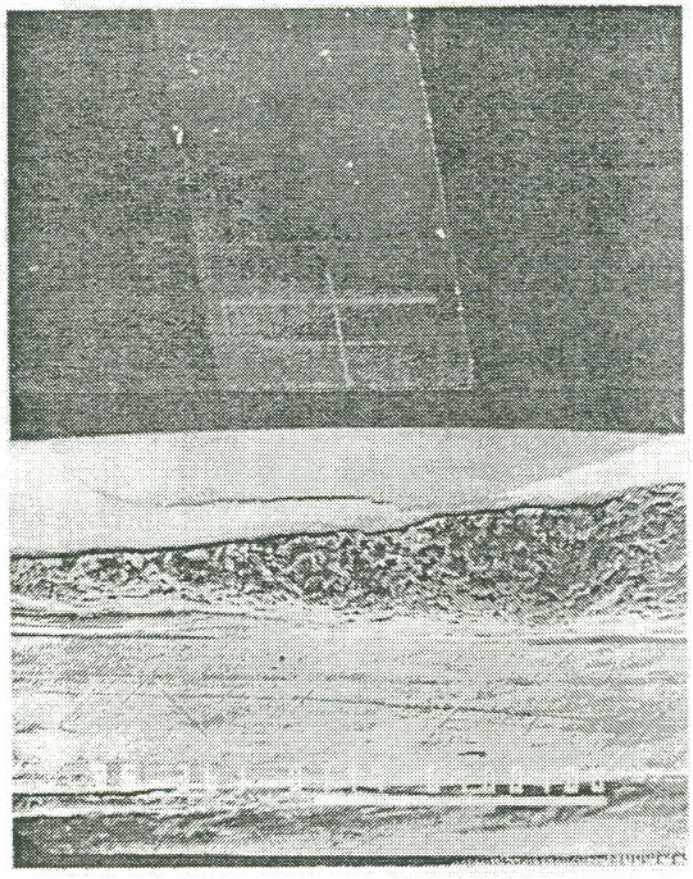

Figure 5.1 — SEM photograph of curved mirror on the unstable resonator laser A1-#1. The view is 30° from vertical, at a magnification of 360× .

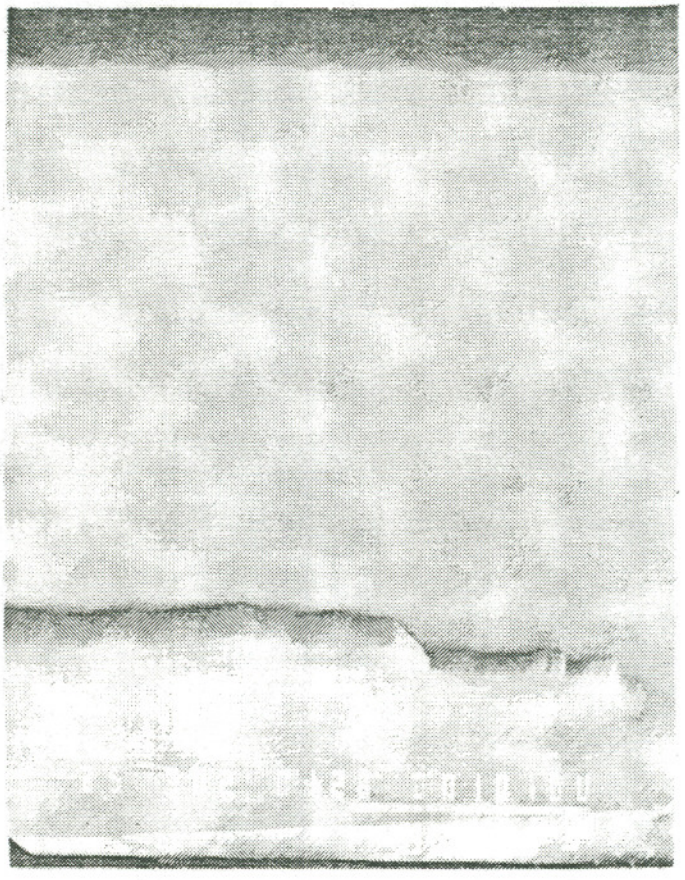

Figure 5.2 — SEM photograph of curved mirror on the unstable resonator laser A1-#1. The view is 30° from vertical, at a magnification of 3000× .

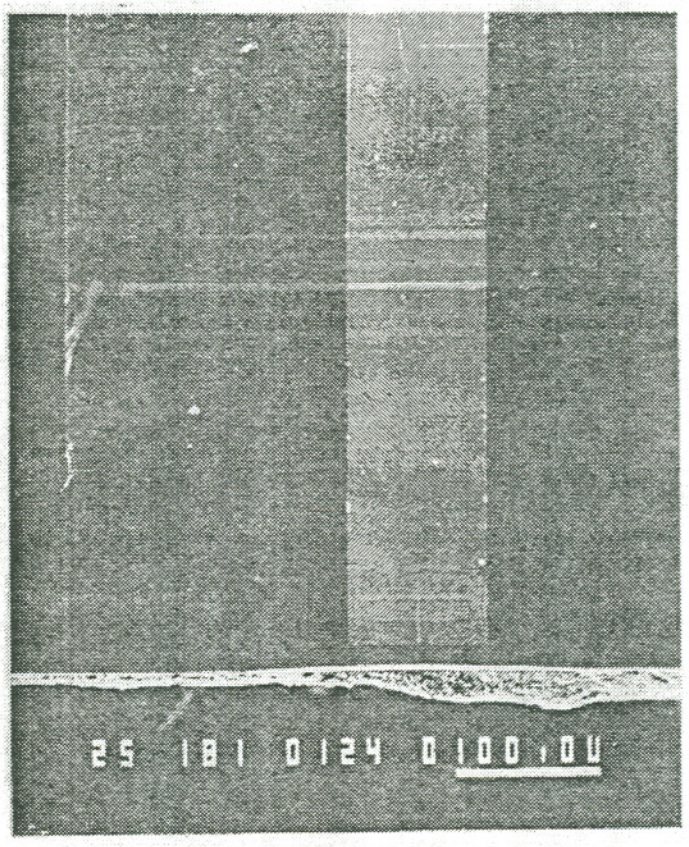

Figure 5.3 — SEM photograph of curved mirror on the unstable resonator laser A1-#1. The view is from the top, at a magnification of 180× .

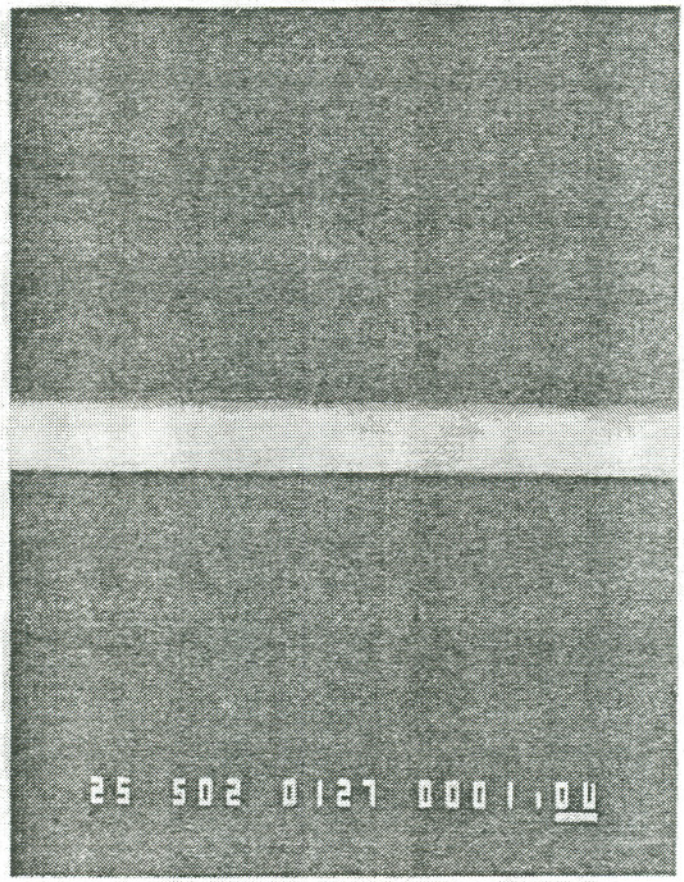

Figure 5.4 — SEM photograph of curved mirror on the unstable resonator laser A1-#1. The view is from the top, at a magnification of 5000× .

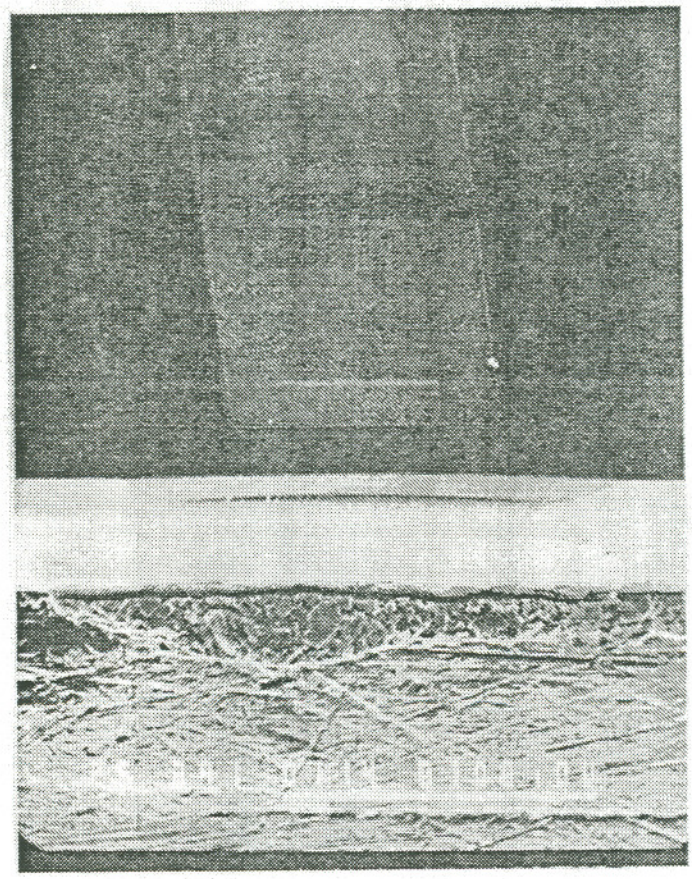

Figure 5.5 — SEM photograph of curved mirror on the unstable resonator laser A1-#4. The view is 30° from vertical, at a magnification of 390× .

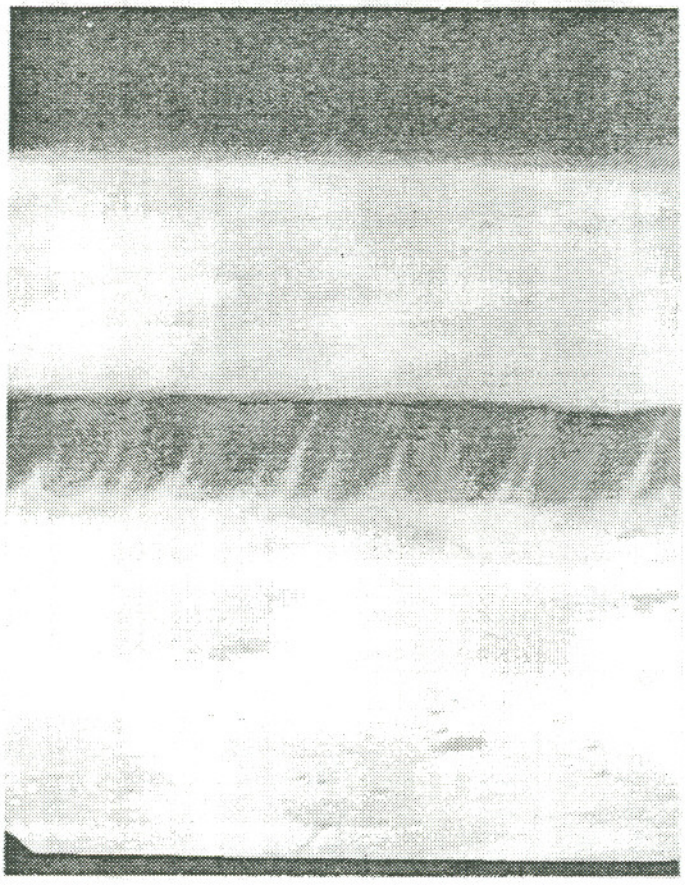

Figure 5.6 — SEM photograph of curved mirror on the unstable resonator laser A1-#4. The view is 30° from vertical, at a magnification of 5000× .

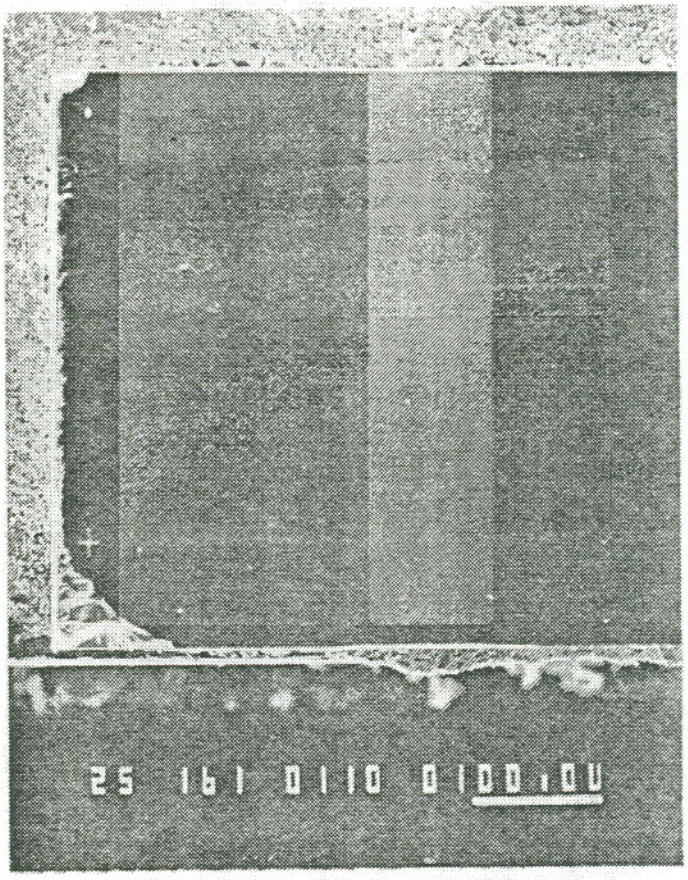

Figure 5.7 — SEM photograph of curved mirror on the unstable resonator laser A1-#4. The view is from the top, at a magnification of 160× .

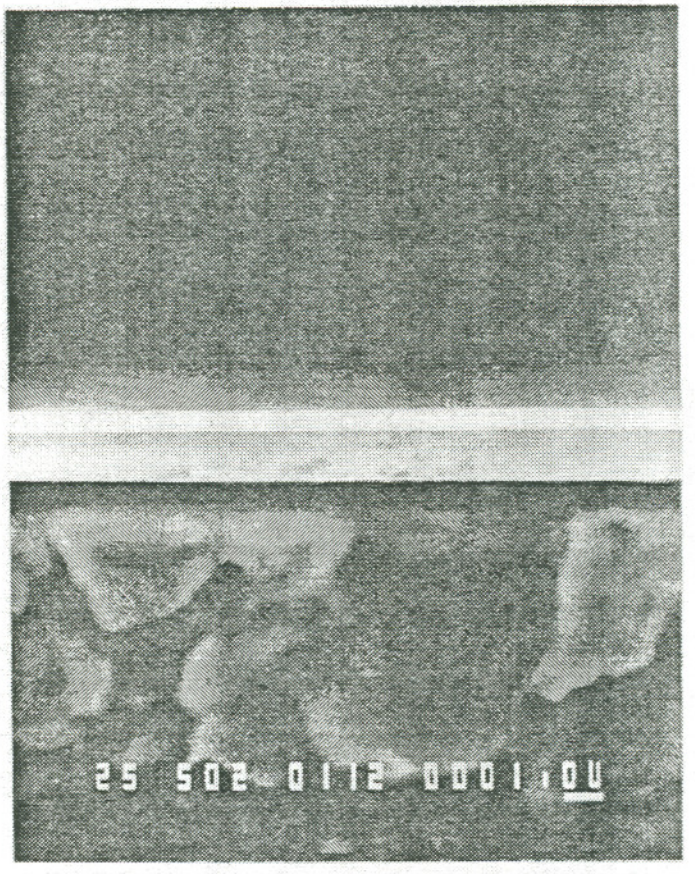

Figure 5.8 — SEM photograph of curved mirror on the unstable resonator laser A1-#4. The view is from the top, at a magnification of 5000× .

see that the curved mirrors are smooth to a scale smaller than 0.1 μm. This is important, since the absence of defects is essential to both producing a spatially uniform beam and testing the validity of any theories. From the second two photographs of each set (Figures 5.3, 5.4, 5.7 and 5.8), we can see that the mirror is a smooth continuous curve, and almost perpendicular to the laser facet, as judged from the small profile of the mirrors when seen from the top.

Figure 5.9 illustrates how the radius and angle of tilt of the machined mirror were calculated. The measured dimensions and estimated uncertainties, taken from SEM photographs, and the calculation results are given in Table 5.1 . The calculated radii were 1946 μm, 2454 μm, 1975 μm, and 1723 μm, and the calculated tilt angles were 1.9°, 2.0°, 3.0°, and 2.5°, for devices A1-#1, A1-#2, A1-#3, and A1-#4, respectively. The uncertainties for the radii, ±400 μm, and the uncertainties for the tilt angles, ±0.5°, were mostly from the uncertainty in determining the aperture depth (from Figure 5.9), caused by the tilt of the mirrors. All four mirrors depart from vertical by only a few degrees. This can be attributed to either an error in the initial tilt of the sample, or the gaussian profile[48] of the ion beam itself.

5.2 L-I Characteristics

Measurements of output light intensity (L) versus input current (I) were made of the four micromachined unstable resonator lasers, and compared with those of a conventional Fabry-Perot laser, with two planar mirrors, from the

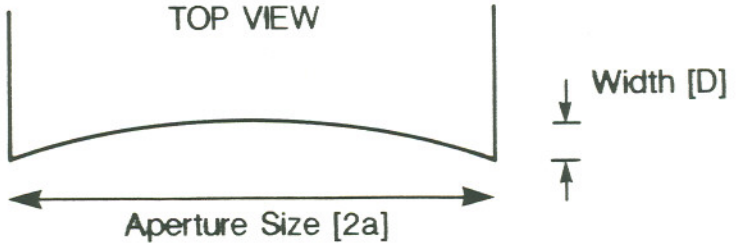

$$R_{calc} = \frac{a^2 + D^2}{2D}$$

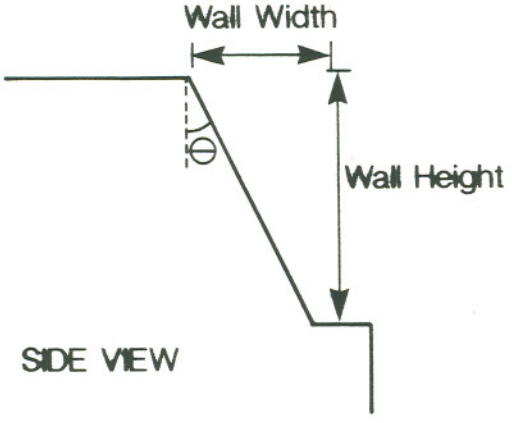

$$\Theta_{calc} = \tan^{-1}\left(\frac{\text{Width}}{\text{Height}}\right)$$

Figure 5.9 — Illustration of the method used to calculate the curvature and tilt angle of the curved mirrors.

Device	Aperture Size [μm]	Width [μm]	Radius [μm]	Wall Width [μm]	Wall Height[μm]	Tilt Angle
A1-#1	216±5	3.0±0.5	1946±400	1.7±0.2	52±5	1.9±0.5°
A1-#2	188±5	1.8±0.5	2454±400	1.8±0.2	52±5	2.0±0.5°
A1-#3	214±5	2.9±0.5	1975±400	0.5±0.1	9.7±1	3.0±0.5°
A1-#4	178±5	2.3±0.5	1723±400	0.6±0.1	13.9±1	2.5±0.5°

Table 5.1 — Measured unstable resonator dimensions.

same material, as shown in Figure 5.10 . The lasers were operated with 100 ns FWHM pulses at a repetition rate of 1 kHz. Input current was measured with an induction current probe, placed on the current-carrying line as close to the laser as possible. The light output from the unstable resonators was measured as emitted from the curved mirror. The average power was measured with a digital photometer, and multiplied by 1 kHz $\times$ 100 ns $=$ 10^4 to get the peak power measurement.

The threshold current of the Fabry-Perot laser was about 150 mA, which corresponds to a threshold current density of about 330 A/cm^2. The single facet slope efficiency was measured to be 0.53 W/A. The slight kinks in the L-I curve are likely due to measurement error caused by changing voltage scales on the oscilloscope. At the highest applied input current of 1200 mA, the output power measured for the Fabry-Perot device was 615 mW.

The threshold currents of the unstable resonators were about 300 mA, twice that of the Fabry-Perot laser. The single facet slope efficiencies were about 0.48 W/A, only slightly lower that that of the Fabry-Perot laser. Similar effects of FIB-induced damage on semiconductor lasers — an increased threshold current with little change in slope efficiency, as compared to undamaged lasers — were observed by Ximen[49]. These effects occur possibly because damage caused by the ion beam creates a saturable absorption region; the damaged region has high loss up to a certain light intensity, and a very low loss at higher intensities. Other losses, such as the losses associated with the unstable resonator geometry,

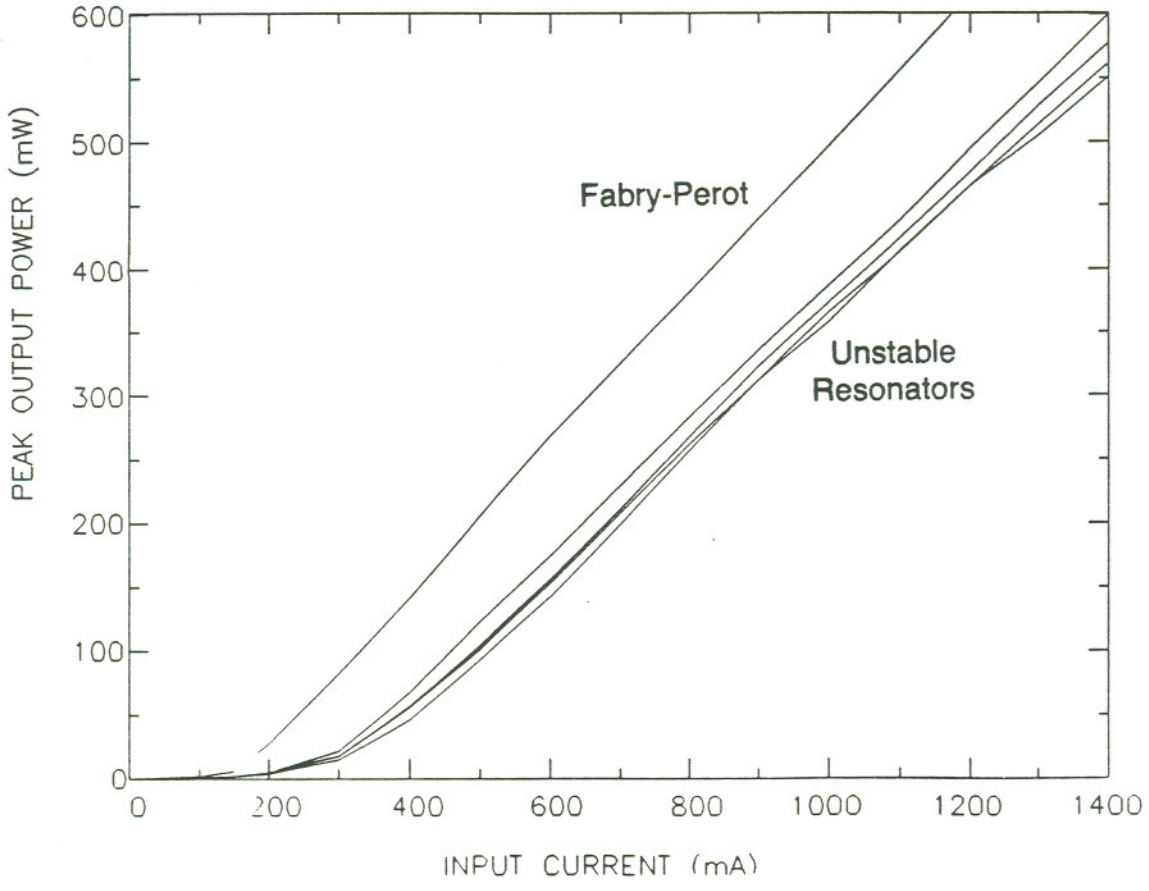

Figure 5.10 — L-I characteristics of Fabry-Perot and unstable resonator semiconductor lasers. The lasers were pulsed 100 ns at 1 KHz.

imperfections of the milled surface, and tilting of the machined mirrors in relation to the cleaved facet, would have an effect on both the threshold current and the slope efficiency, so are likely smaller than the saturable absorption losses for these devices.

The highest output power measured, 600 mW for A1-#4, is adequate for many of the applications mentioned in Chapter 1, and the highest reported to date for an unstable resonator semiconductor laser. This power is measured from a single facet, and would perhaps double if a high-reflectivity coating were applied to the planar facet. It should also be noted that the similarity of the L-I curves for all four of the machined devices is another indication of the reproducibility of the focused ion beam micromachining process.

5.3 Wavelength Measurements

Wavelength measurements were also made on all the devices. The experimental setup is shown schematically in Figure 5.11 . The laser and heat sink assembly were set into a rotating mount, and turned so that the junction of the laser was vertical. A lens focused the near field image of the laser facet onto the input slit of a SPEX 1269 spectrometer. For the Fabry-Perot laser, the image was an elongated spot, which was aligned parallel to the input slit. The image of the near field at the facet of the unstable resonators, on the other hand, was complicated by the presense of an extra "virtual spot", caused by the curved mirror, with a focus point a few microns behind the facet. Inside the spectrometer,

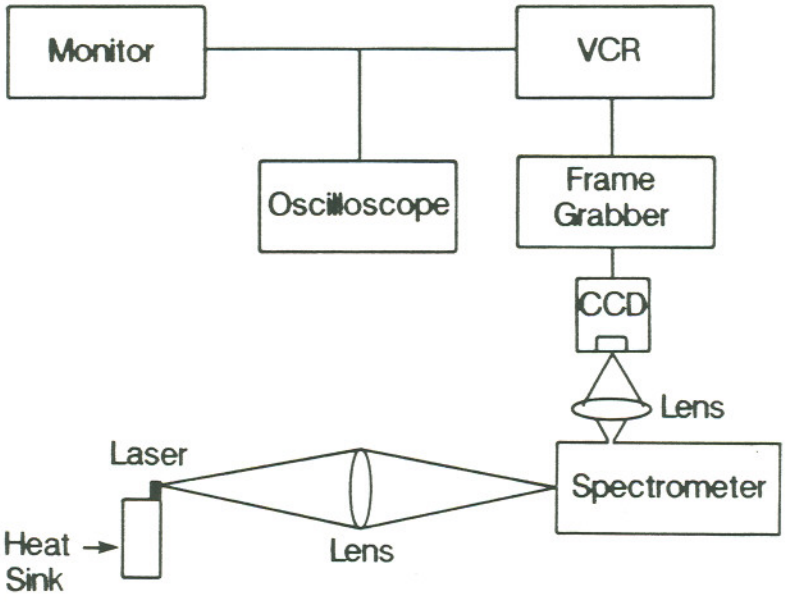

Figure 5.11 — Experimental setup for spectral measurements.

the light was reflected off a diffraction grating, in first order, towards the exit slit of the spectrometer, where the light was imaged with a CCD camera. The output of the CCD camera was sent to a frame grabber. Digitized video images were fed into a VCR and stored on a video tape. The output of the VCR was split to an oscilloscope and a video monitor.

Before data was recorded, the output of the CCD camera was fed directly into the oscilloscope, and the laser pulse repetition rate was adjusted so that the camera was not saturated. The CCD output was then reconnected to the frame grabber, and the frame grabber brightness and contrast controls were adjusted to get the maximum non-saturated video signal without eliminating the small background signal.

Once all the data was recorded on videotape, selected frames were digitized again by the frame grabber. Software on an Apple IIe created one-dimensional intensity data sets by summing the total intensity over each row of the digitized image. These data sets were stored on floppy disks and transferred to the OGI APEE MicroVax.

Wavelength measurements of all the lasers were made at currents corresponding to peak power outputs of 100, 300, and 500 mW. Spectra of the Fabry-Perot device are shown in Figures 5.12 - 5.14 . About 14 longitudinal modes, at wavelengths near 8400 Å, are seen at 100 mW. At 500 mW, at least 5 extra modes can be seen near 8380 Å. The cause of these extra peaks is not known, and cursory observations of other Fabry-Perot devices do not exhibit the

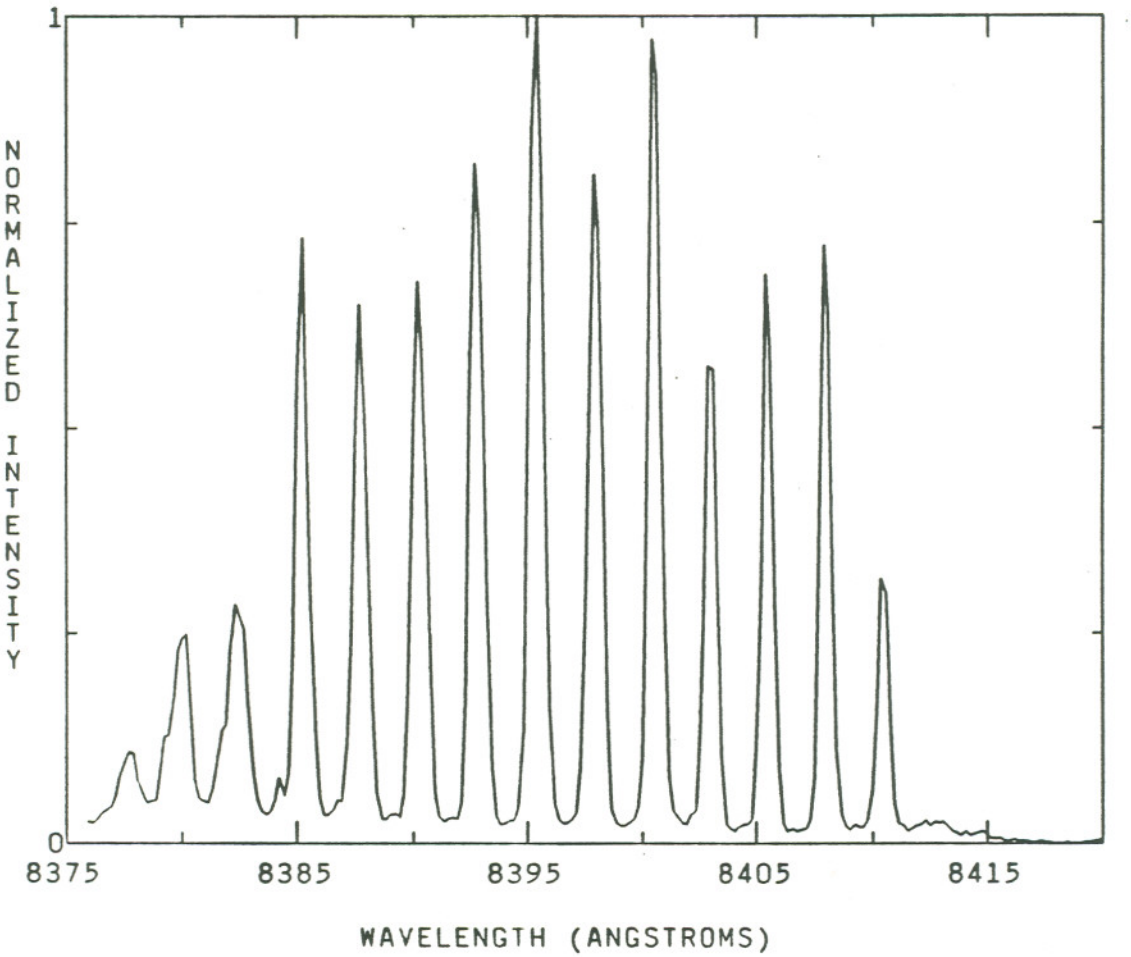

Figure 5.12 — Spectral characteristics of a Fabry-Perot laser A2-#1 at an output power level of 100 mW.

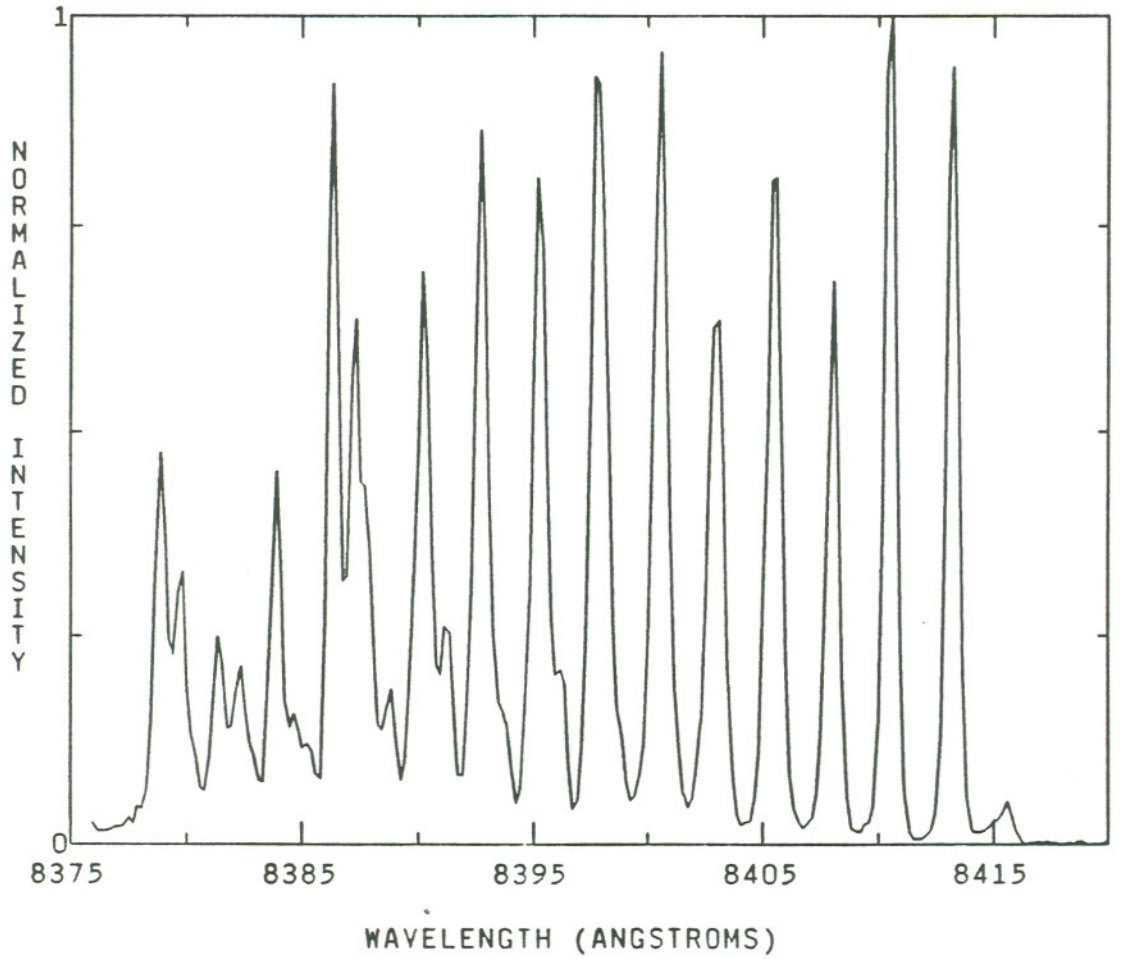

Figure 5.13 — Spectral characteristics of a Fabry-Perot laser A2-#1 at an output power level of 300 mW.

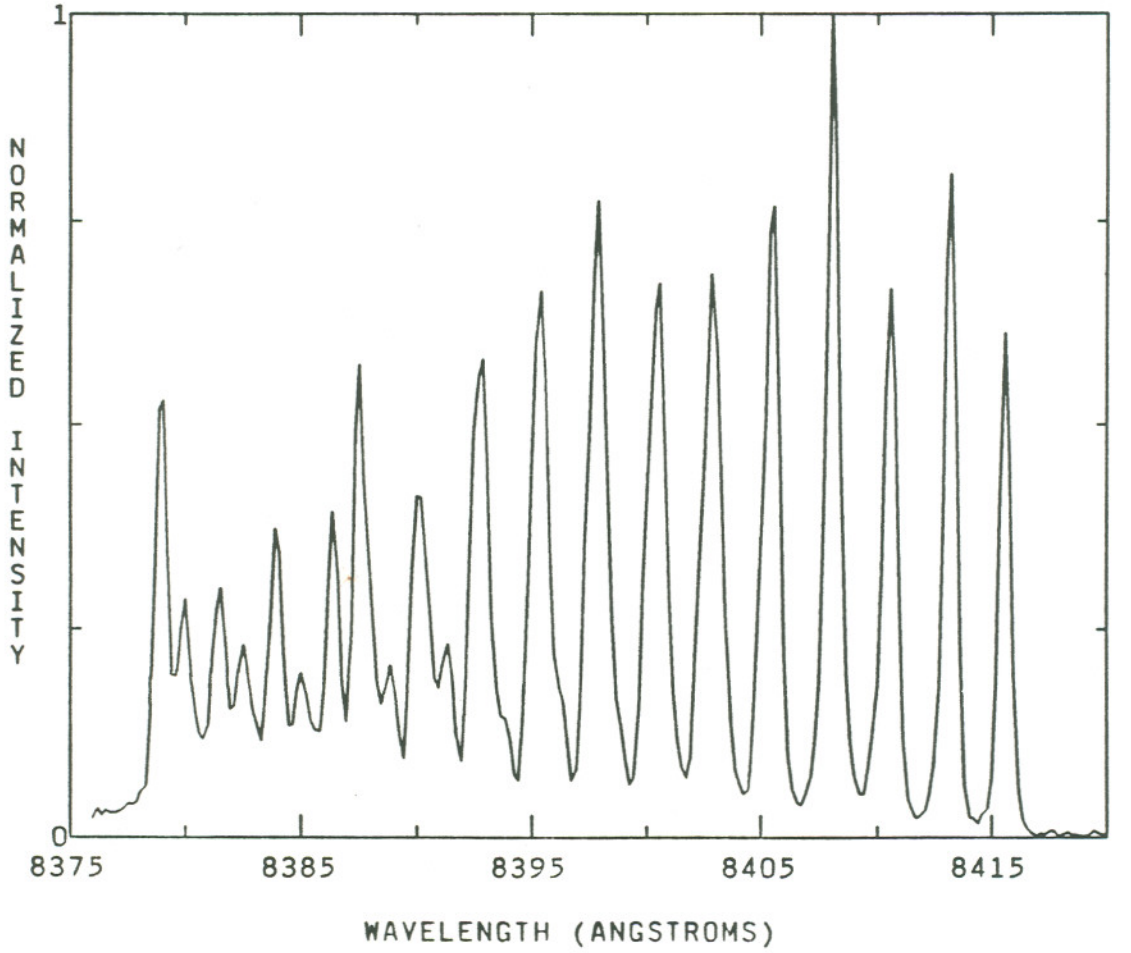

Figure 5.14 — Spectral characteristics of a Fabry-Perot laser A2-#1 at an output power level of 500 mW.

extra peaks at high powers.

Spectra of unstable resonator A1-#2 are are shown in Figures 5.15 - 5.17, and spectra of A1-#4 are shown in Figures 5.18 - 5.20 . The spectra of all the unstable resonators were in general characterized by having a a large number of longitudinal modes. Counting only those modes with an intensity of at least about 5% the maximum intensity peak, there were at least 70 longitudinal modes, over a range of about 150 Å. At a particular power level, a single mode might dominate, but the multimode behavior would reappear at higher powers. This effect is seen more clearly in the spectra for A1-#2 than for A1-#4. The spectra for A1-#4 seems to have a single dominant mode over its entire power range, but this is an artifact of the small number of measured power levels.

5.4 Far Field Measurements

Far field measurements, which are important because of the desire for a single-lobed diffraction-limited output beam, were also taken for the Fabry-Perot and unstable resonator devices. The experimental setup for these measurements is shown in Figure 5.21 . An optical filter (nominal 1.0 transmittance) was placed directly in front of the laser, and CCD camera was moved in as far as possible, to capture the laser light. The output of the CCD camera was tested for saturation and recorded on videotape as for the wavelength measurements, described in the previous section.

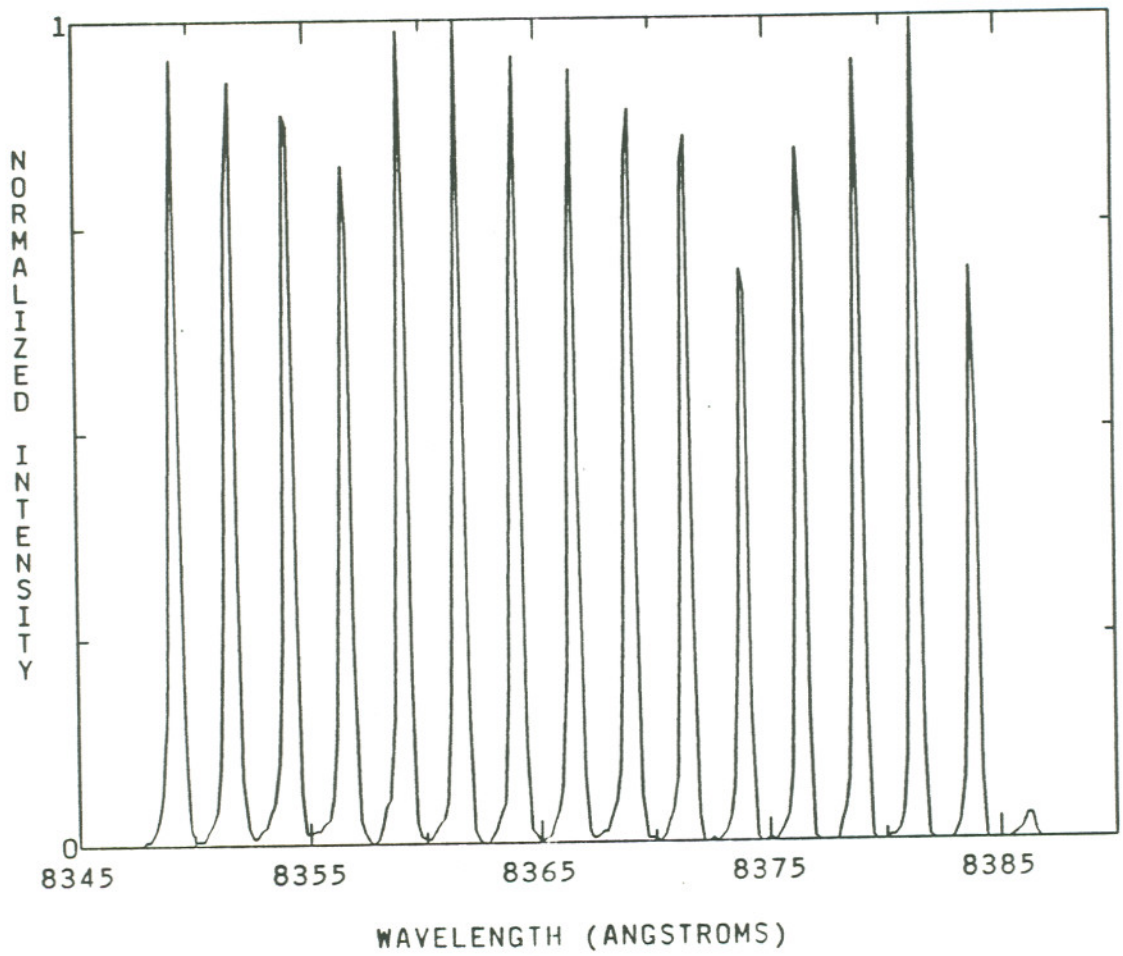

Figure 5.15 — Spectral characteristics of unstable resonator A1-#2 at an output power level of 100 mW.

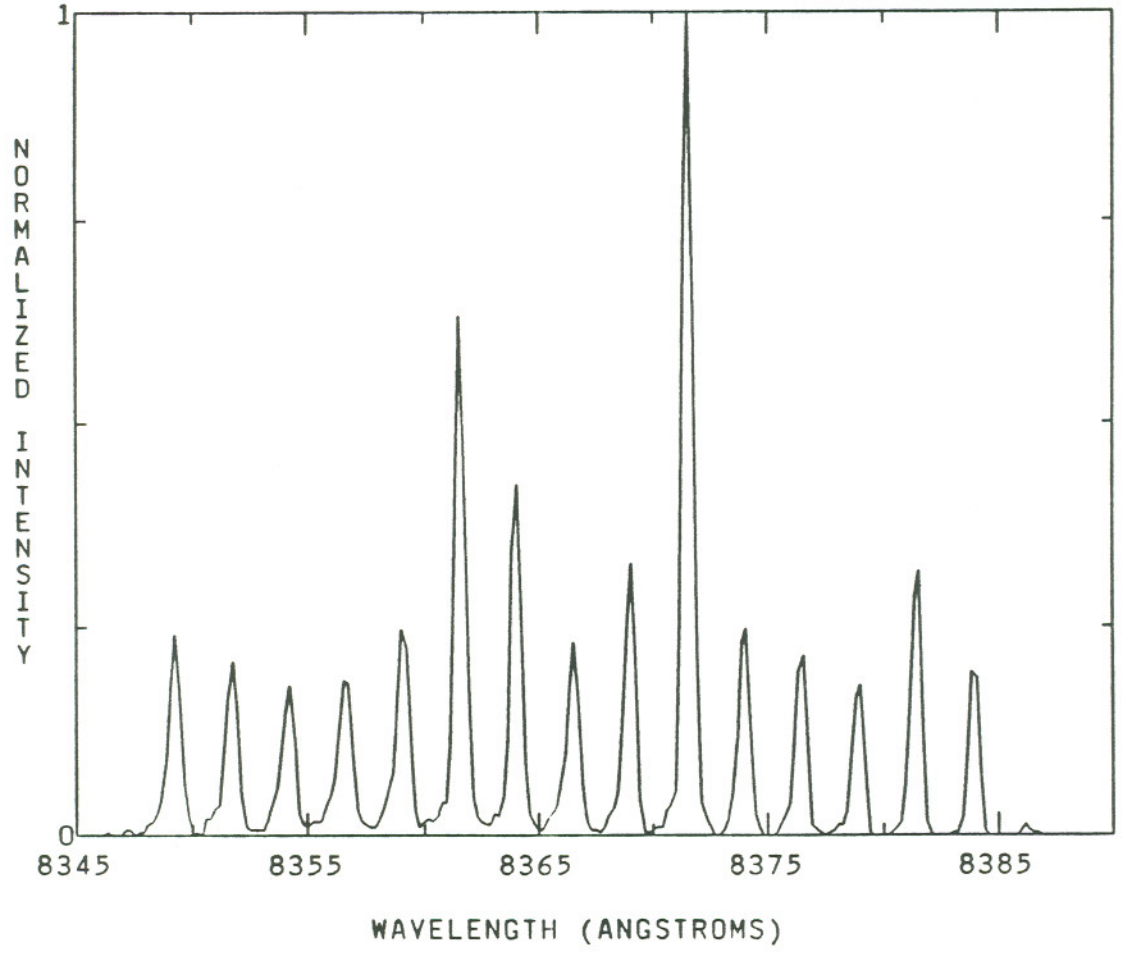

Figure 5.16 — Spectral characteristics of unstable resonator A1-#2 at an output power level of 300 mW.

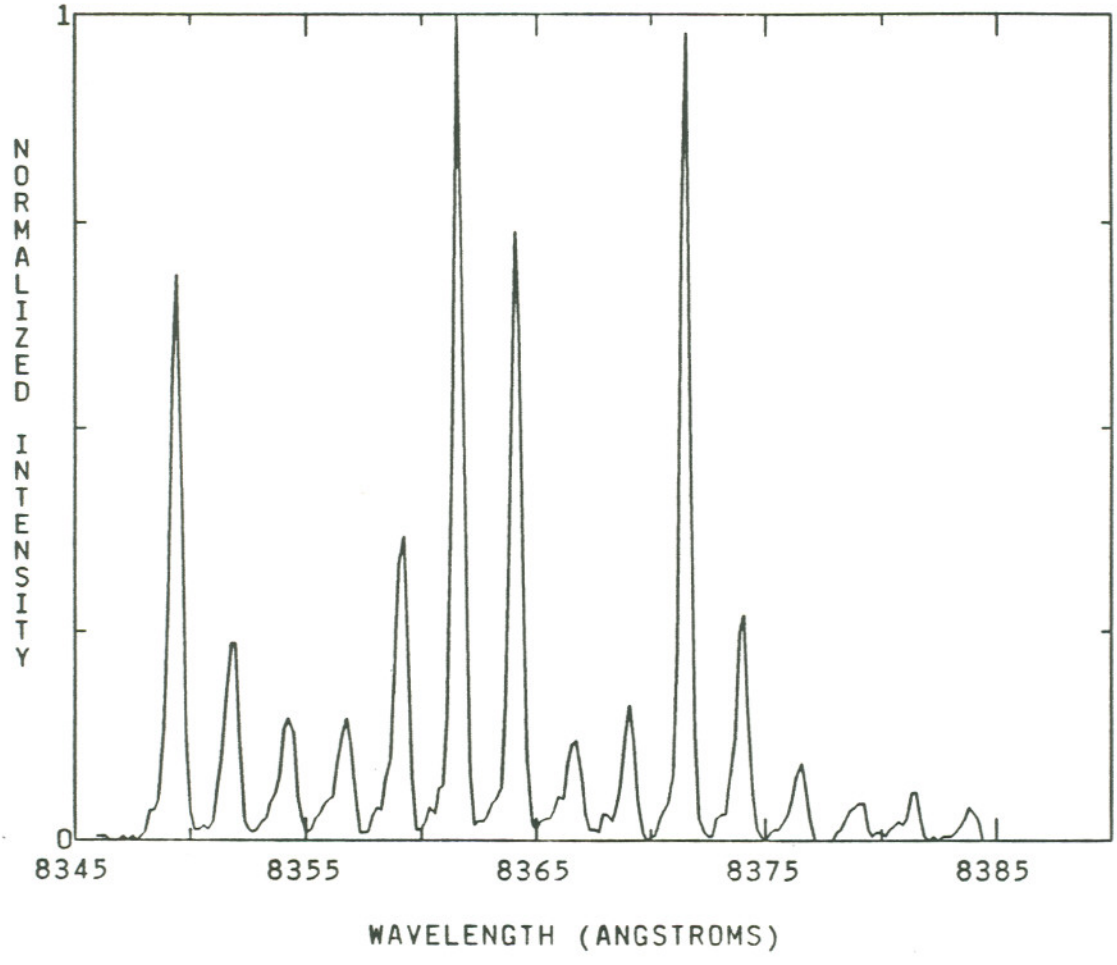

Figure 5.17 — Spectral characteristics of unstable resonator A1-#2 at an output power level of 500 mW.

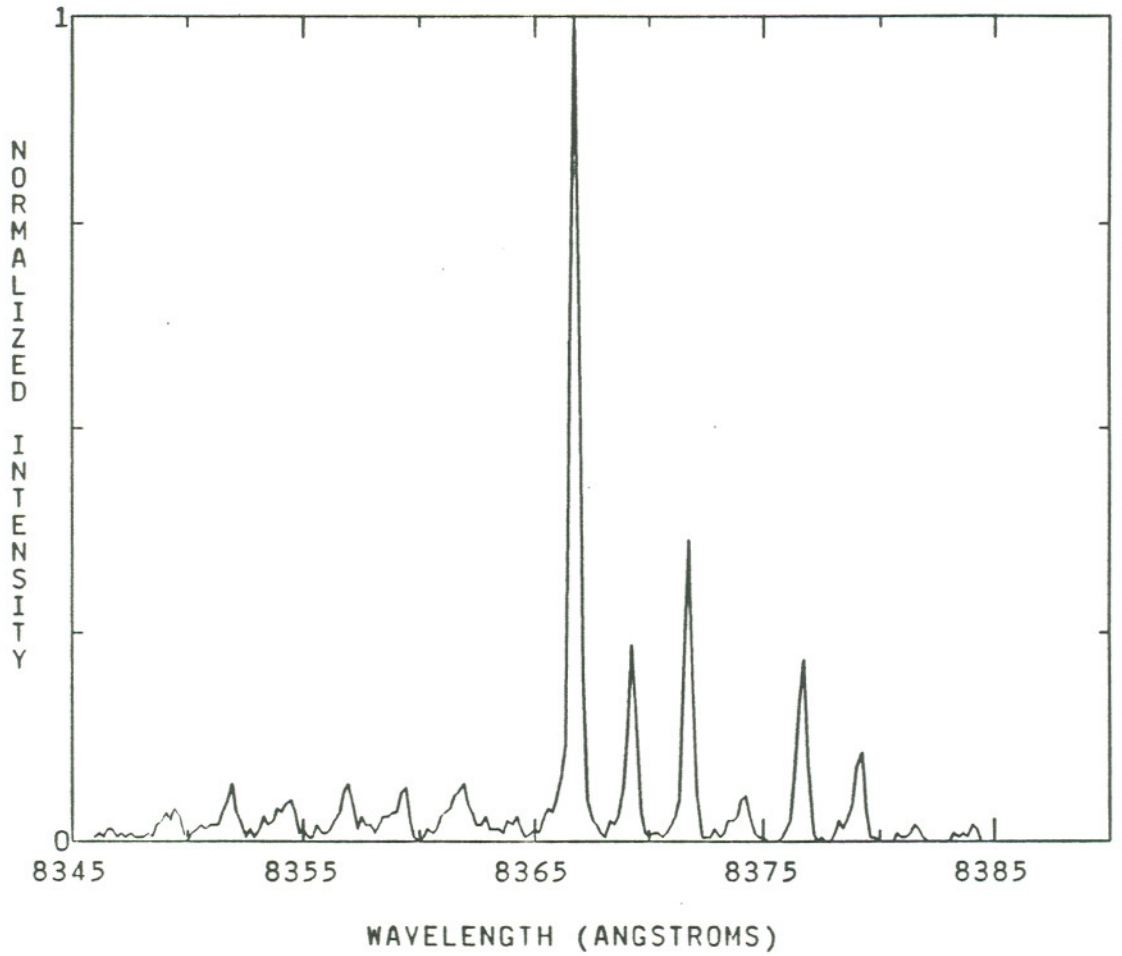

Figure 5.18 — Spectral characteristics of unstable resonator A1-#4 at an output power level of 100 mW.

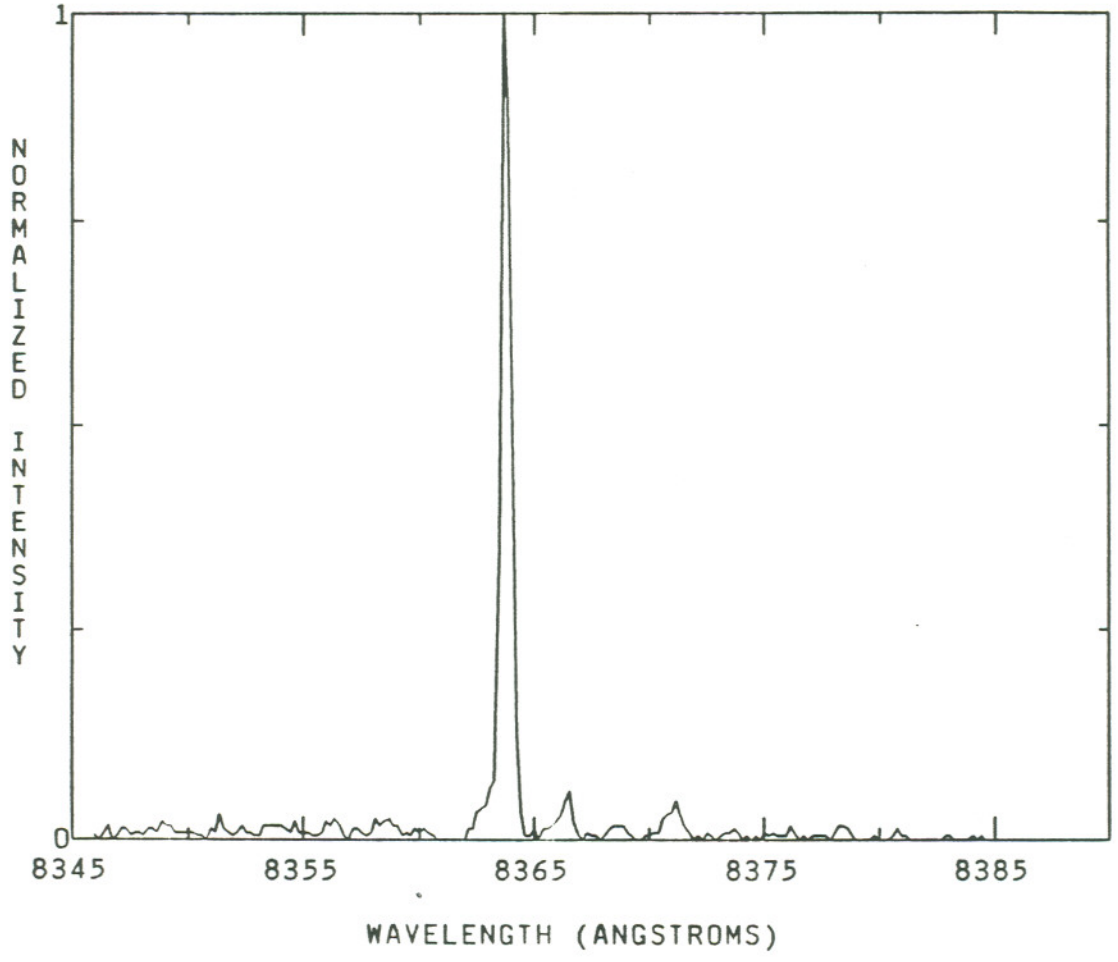

Figure 5.19 — Spectral characteristics of unstable resonator A1-#4 at an output power level of 300 mW.

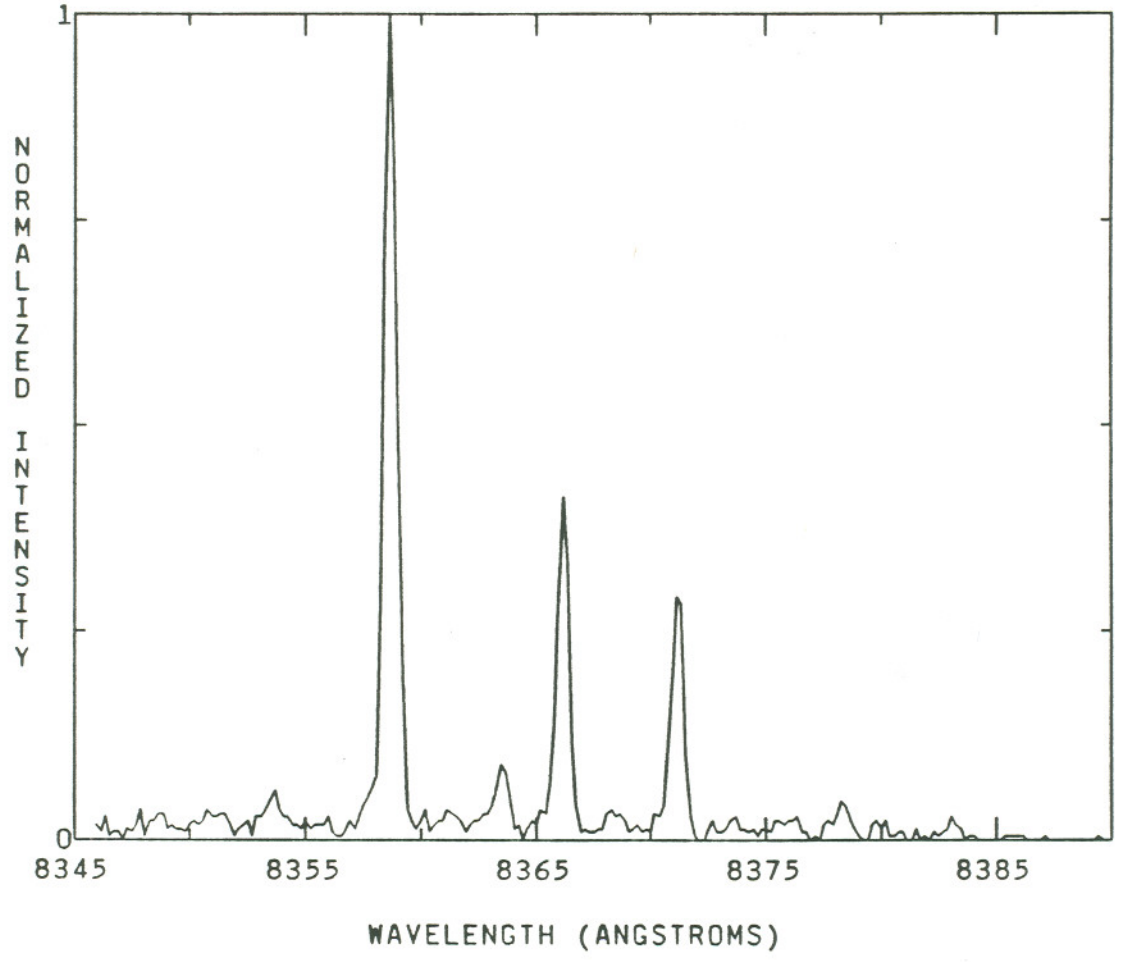

Figure 5.20 — Spectral characteristics of unstable resonator A1-#4 at an output power level of 500 mW.

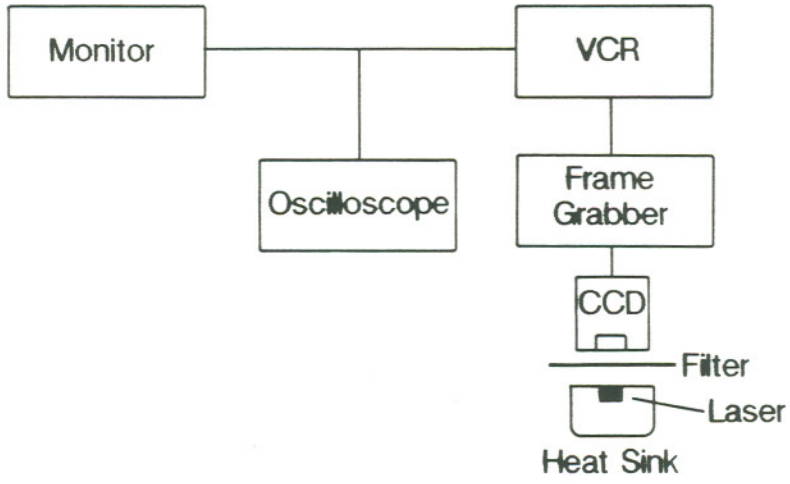

Figure 5.21 — Experimental setup for far field measurements.

The primary concern in measuring the far field is whether the light is measured at a plane far enough away to be considered a "true" far field — it must satisfy the Fraunhofer condition. This condition is given by

$$z >> \frac{\pi a^2}{\lambda} \tag{5.1}$$

where z is the distance from the lasing aperture to the measurement plane and a is the half width of the emitting aperture. For this experimental setup, z was 23 mm. Taking a to be 50 μm and λ to be 8400 Å, the minimum z is calculated to be 9.3 mm, so we can consider the Fraunhofer condition to be satisfied.

The far fields observed from the Fabry-Perot device (Figures 5.22 - 5.24) had a single broad band, with a sharp peak off to one side. The cause of the peak in the far field is not known, but it is possibly from stress induced in the crystal by the deposited SiO_2. Such stress might cause a distortion of the phase front of the beam at the facet, thus affecting the far field. Cursory observations of other Fabry-Perot devices made from the same material, however, do not exhibit such sharp peaks in the far field. Ignoring the peak, the broad part of the far field pattern ranges from 10° to 20° FWHM, which is much wider than the diffraction limit of 0.55° for a uniform plane wave of the same width.

Figures 5.25 - 5.27 are the far field patterns measures from the unstable resonator A1-#2. They show two broad groups of peaks, with two maxima roughly 12° apart. The width of the left large peak, as seen on the figures, decreases from 3.0° FWHM at 100 mW to 2.4° FWHM at 500 mW. The width of

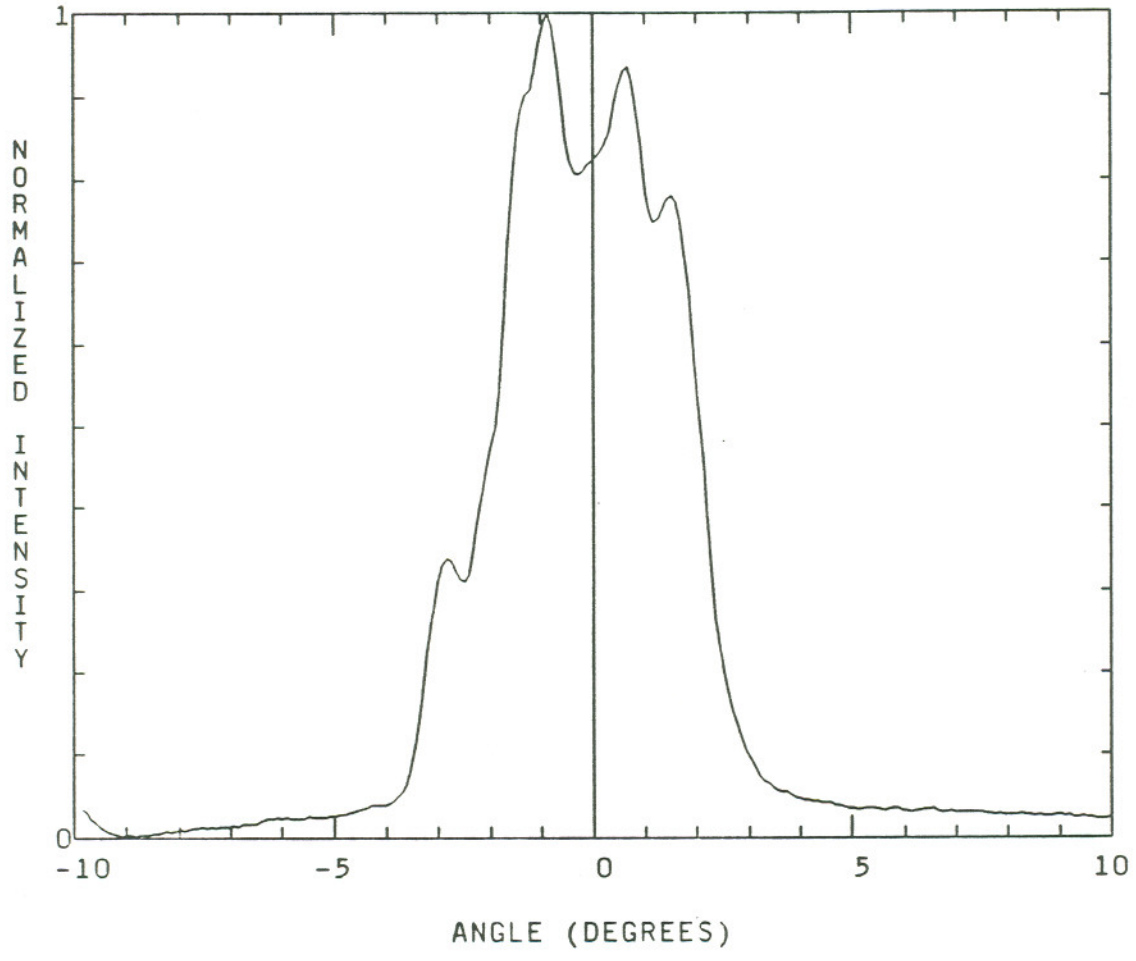

Figure 5.22 — Far field characteristics of Fabry-Perot laser A2-#1 at an output power level of 100 mW.

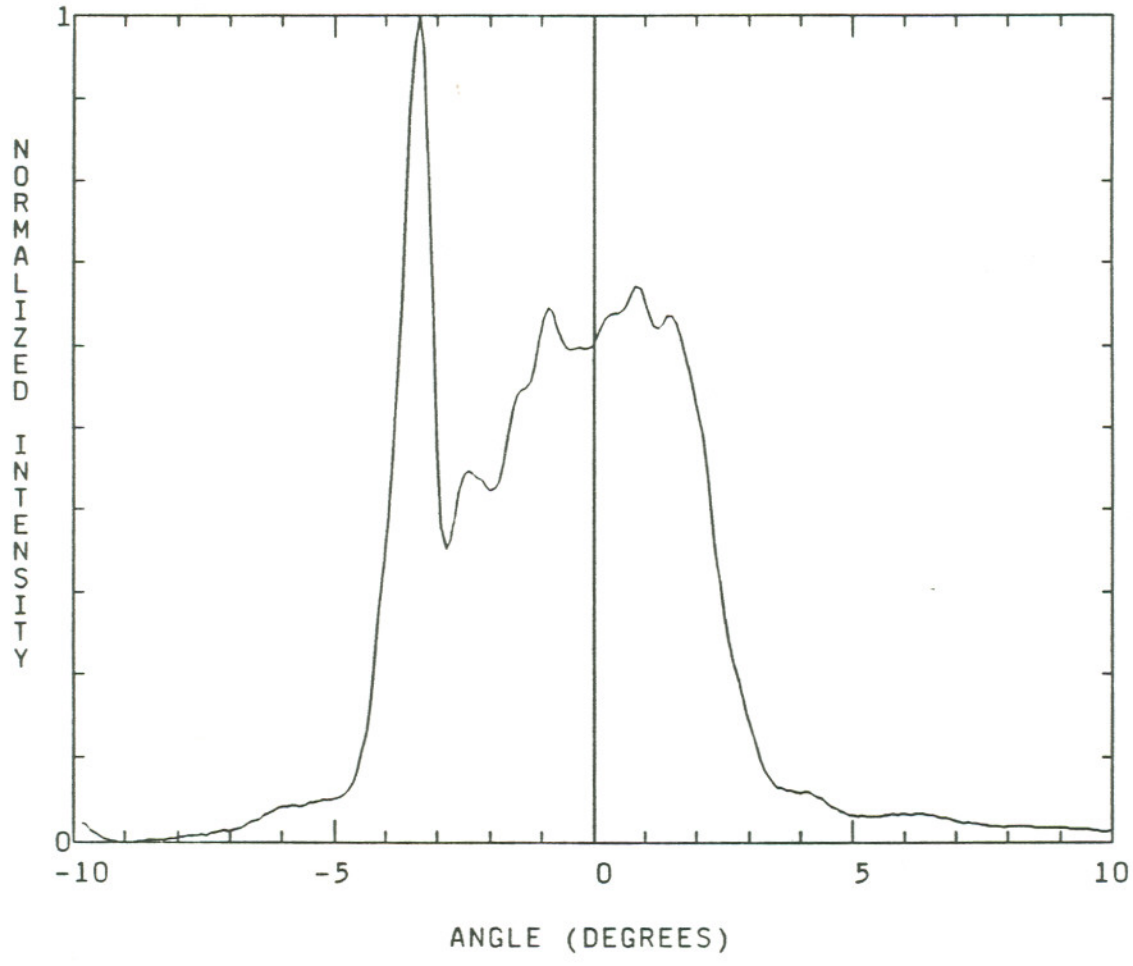

Figure 5.23 — Far field characteristics of Fabry-Perot laser A2-#1 at an output power level of 300 mW.

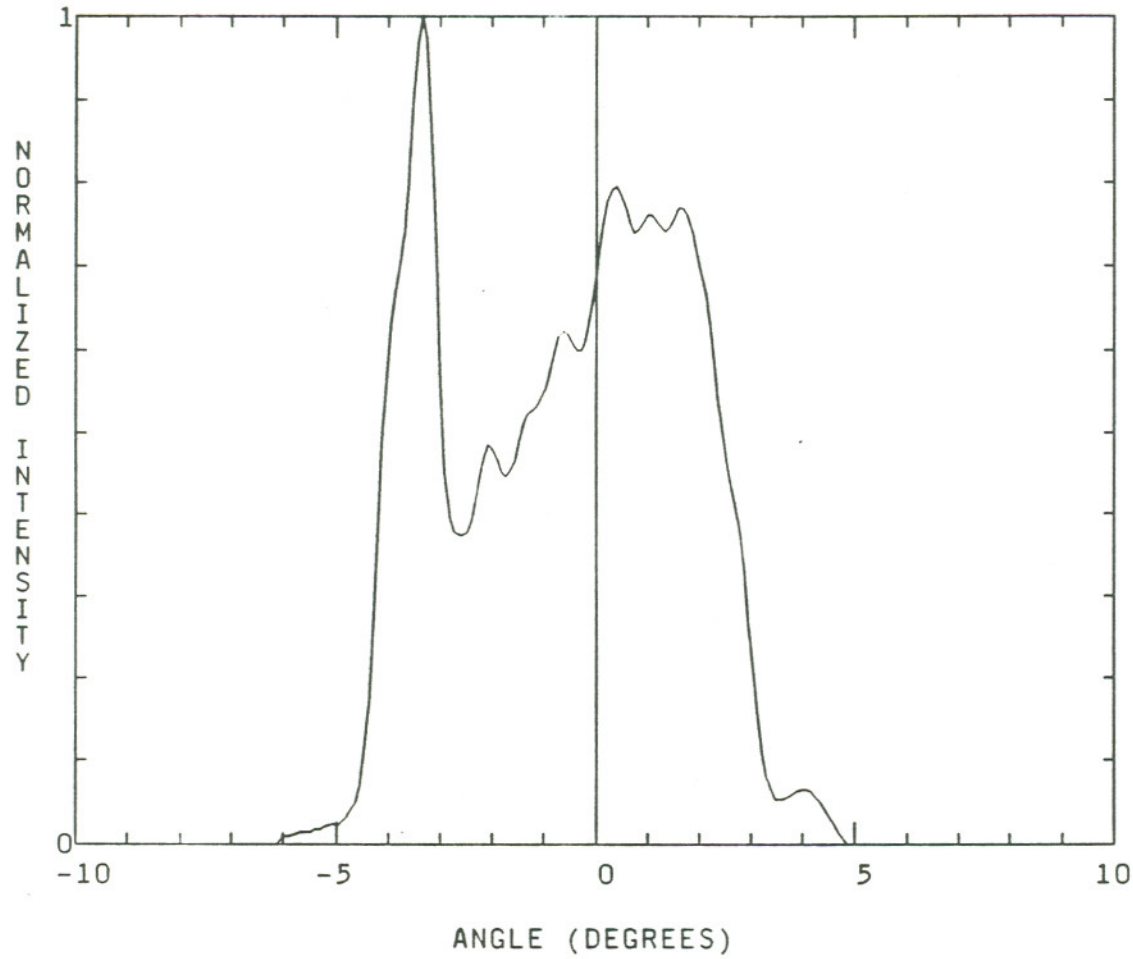

Figure 5.24 — Far field characteristics of Fabry-Perot laser A2-#1 at an output power level of 500 mW.

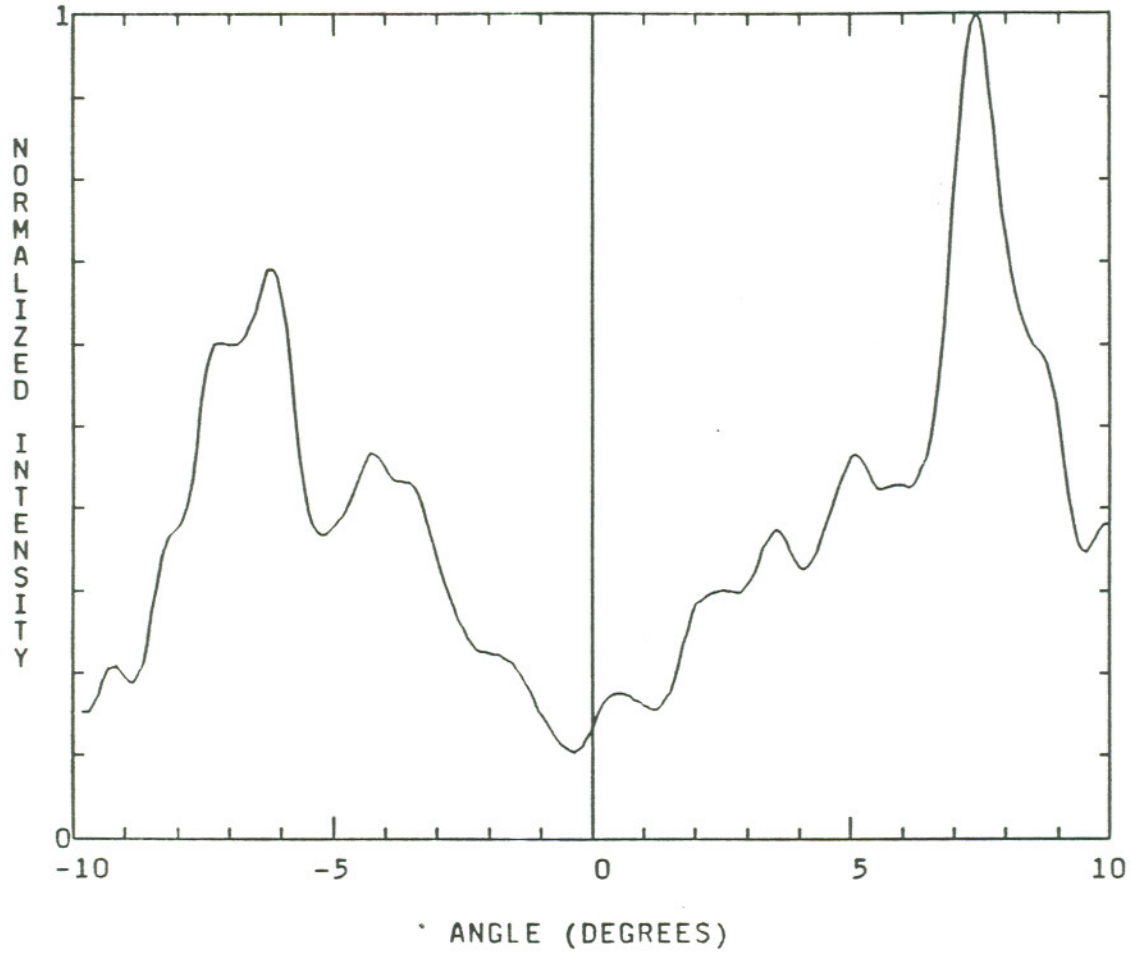

Figure 5.25 — Far field characteristics of unstable resonator A1-#2 at an output power level of 100 mW.

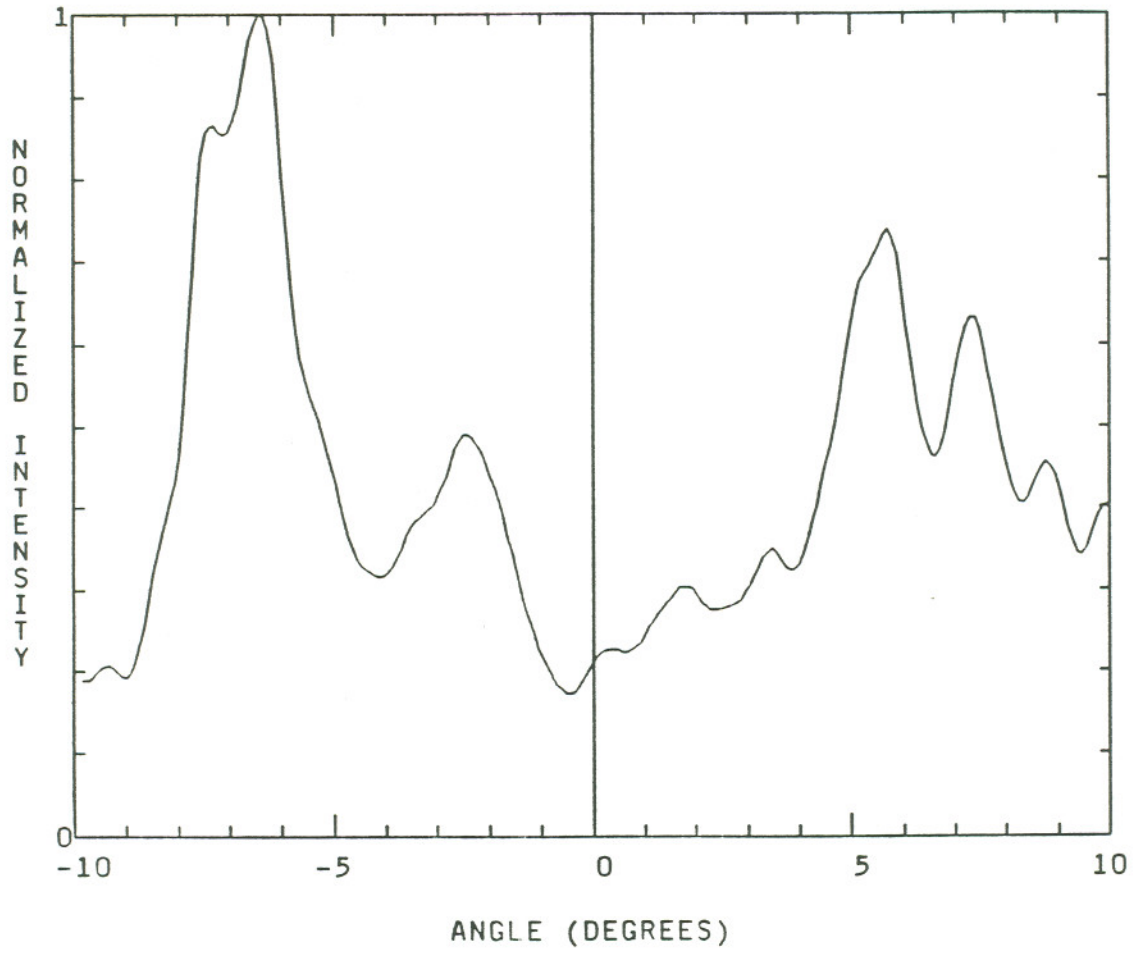

Figure 5.26 — Far field characteristics of unstable resonator A1-#2 at an output power level of 300 mW.

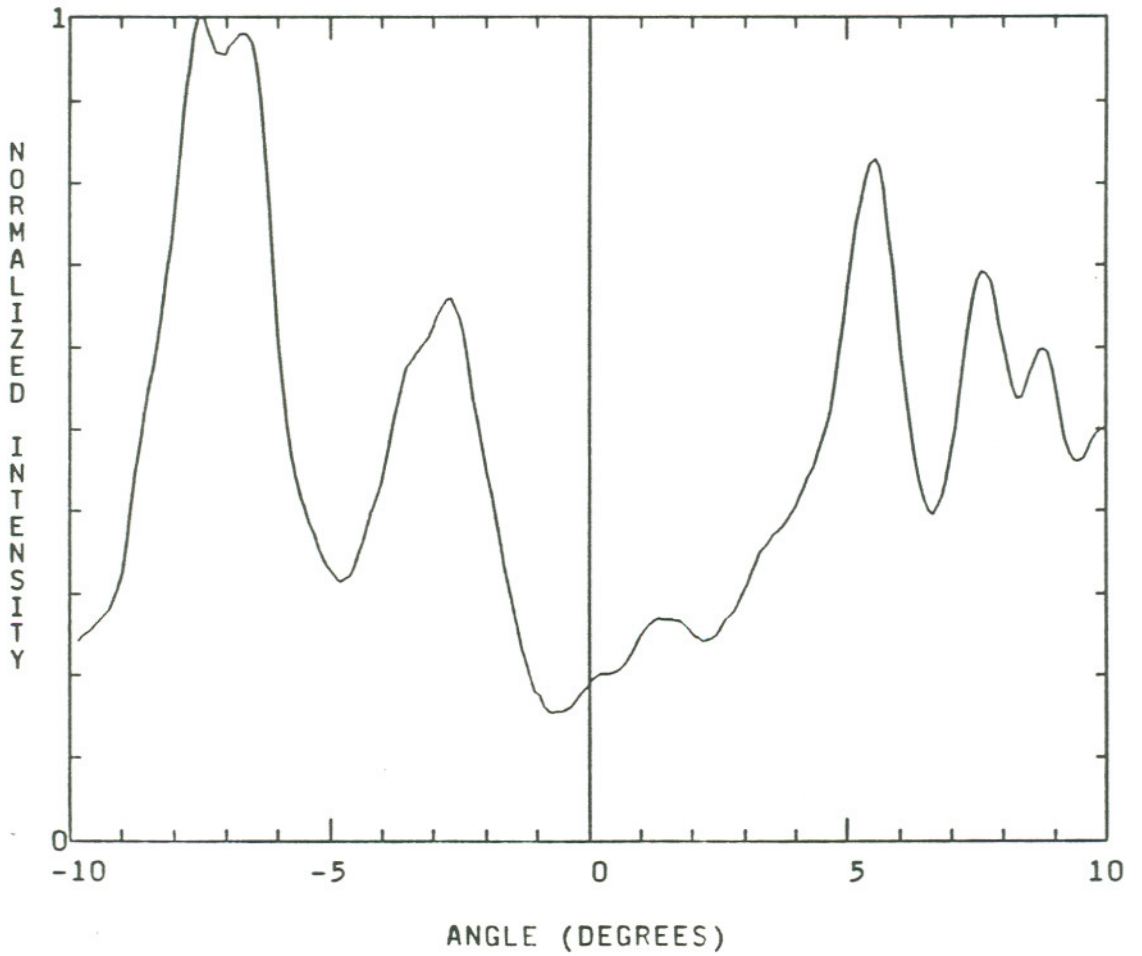

Figure 5.27 — Far field characteristics of unstable resonator A1-#2 at an output power level of 500 mW.

the right large peak, as seen on the figures, increases from 2.7° FWHM at 100 mW to 2.9° FWHM at 500 mW. In addition, at 500 mW, two other peaks, about 6° apart, and each 2.7° FWHM, differentiate from the broader groups.

Figures 5.28 - 5.30 are the far field patterns measures from the unstable resonator A1-#4. They show a similar pattern to Figures 5.25 - 5.28, although the maximum intensity peaks are somewhat narrower and well-defined. The width of the left large peak, as seen on the figures, decreases from 3.0° FWHM at 100 mW to 2.2° FWHM at 500 mW, while the width of the right large peak, as seen on the figures, remains roughly constant at 4.5° FWHM.

Similar two-lobed patterns, with similar dependence on drive current, are observed for the other micromachined devices, although the widths of the peaks are slightly different for each device. This is further evidence for the reproducibility of the micromachining process.

5.5 Imaging of Virtual Point Source

In measurements made at the Air Force Weapons Laboratory, the output of unstable resonator A1-#3 was focused by an 8 mm focal length lens and was imaged onto a detector array 89 cm away. The data was recorded by photographing the oscilloscope trace of the detector array output signal, and the absolute spot size was derived from the physical size of the detector array. Image traces for 1.5, 2, 3, and 5 times threshold current are shown in Figure 5.31. The FWHM of the imaged virtual spot was about 31 μm at 1.5 times threshold, and

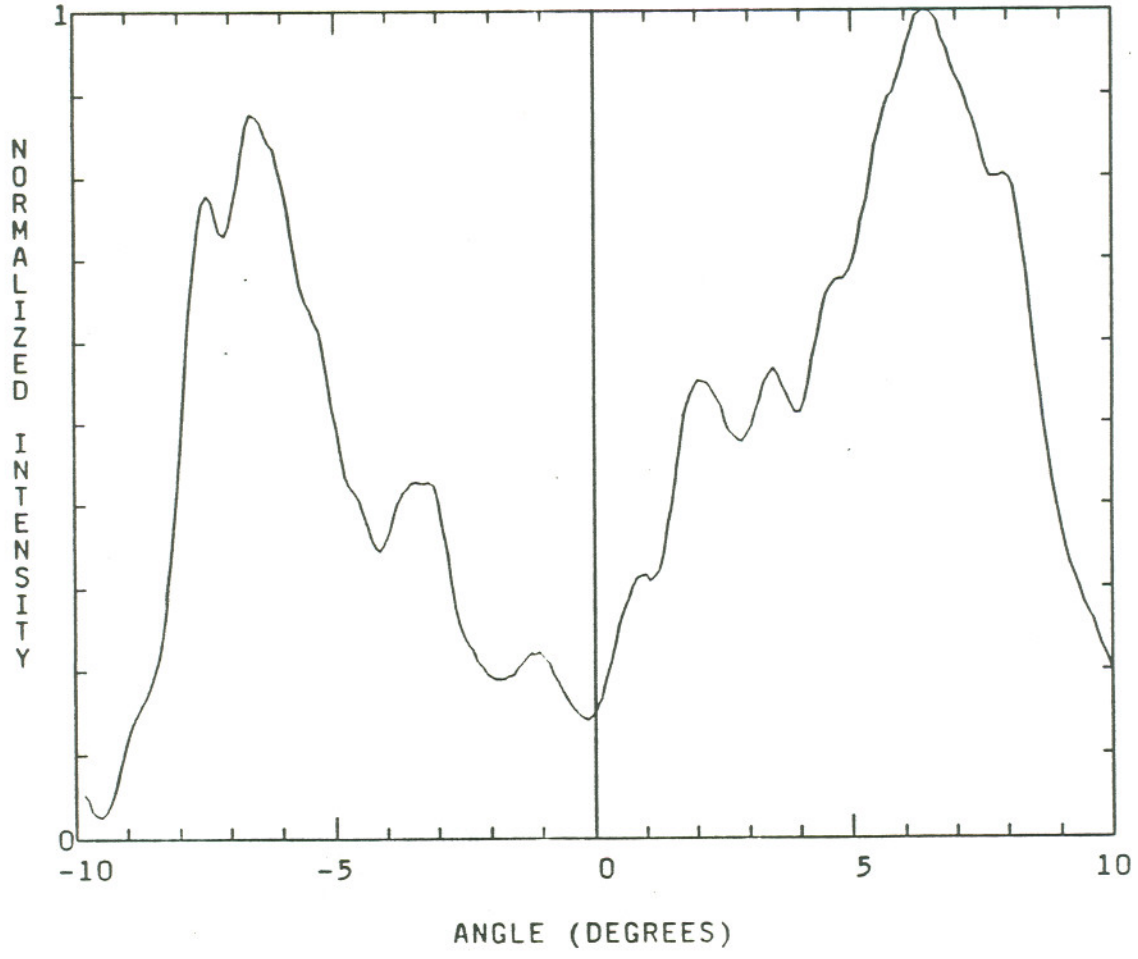

Figure 5.28 — Far field characteristics of unstable resonator A1-#4 at an output power level of 100 mW.

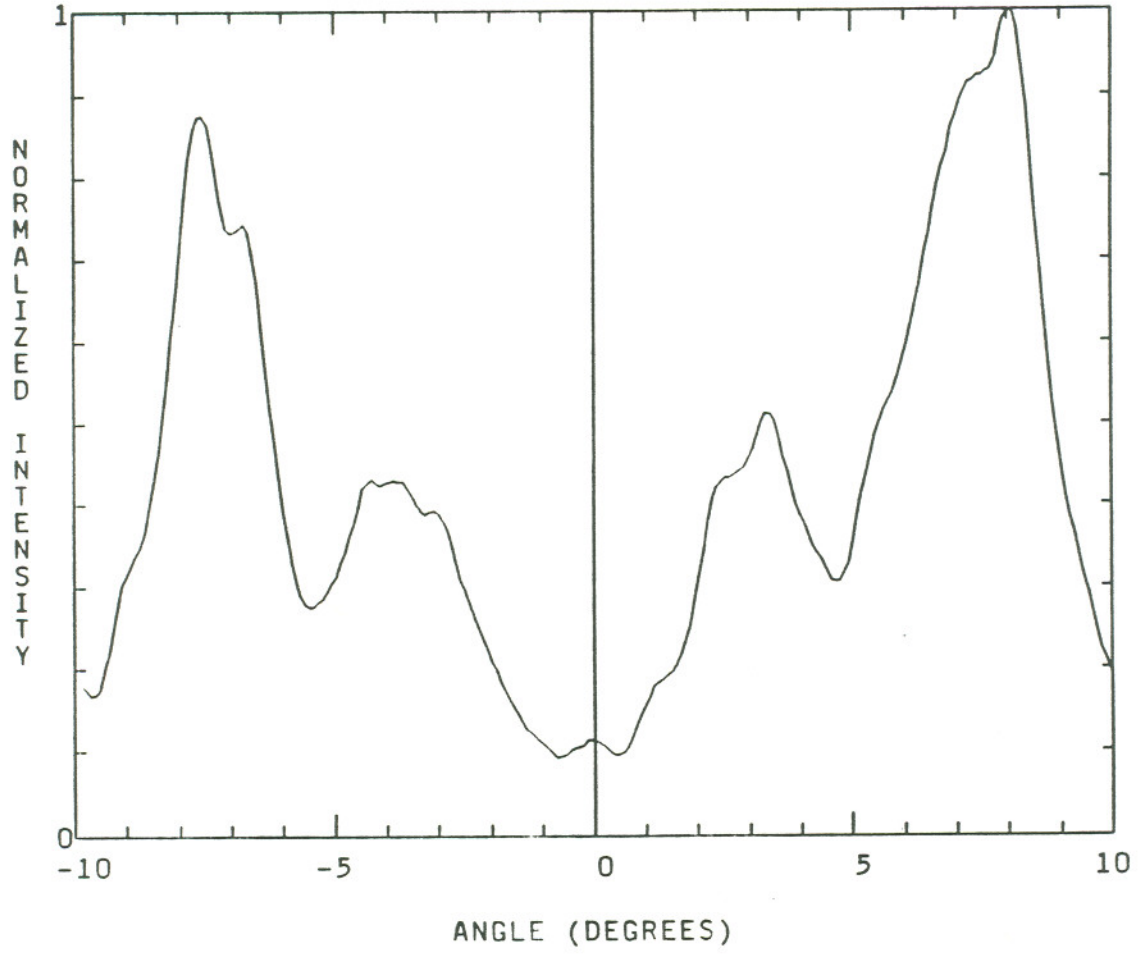

Figure 5.29 — Far field characteristics of unstable resonator A1-#4 at an output power level of 300 mW.

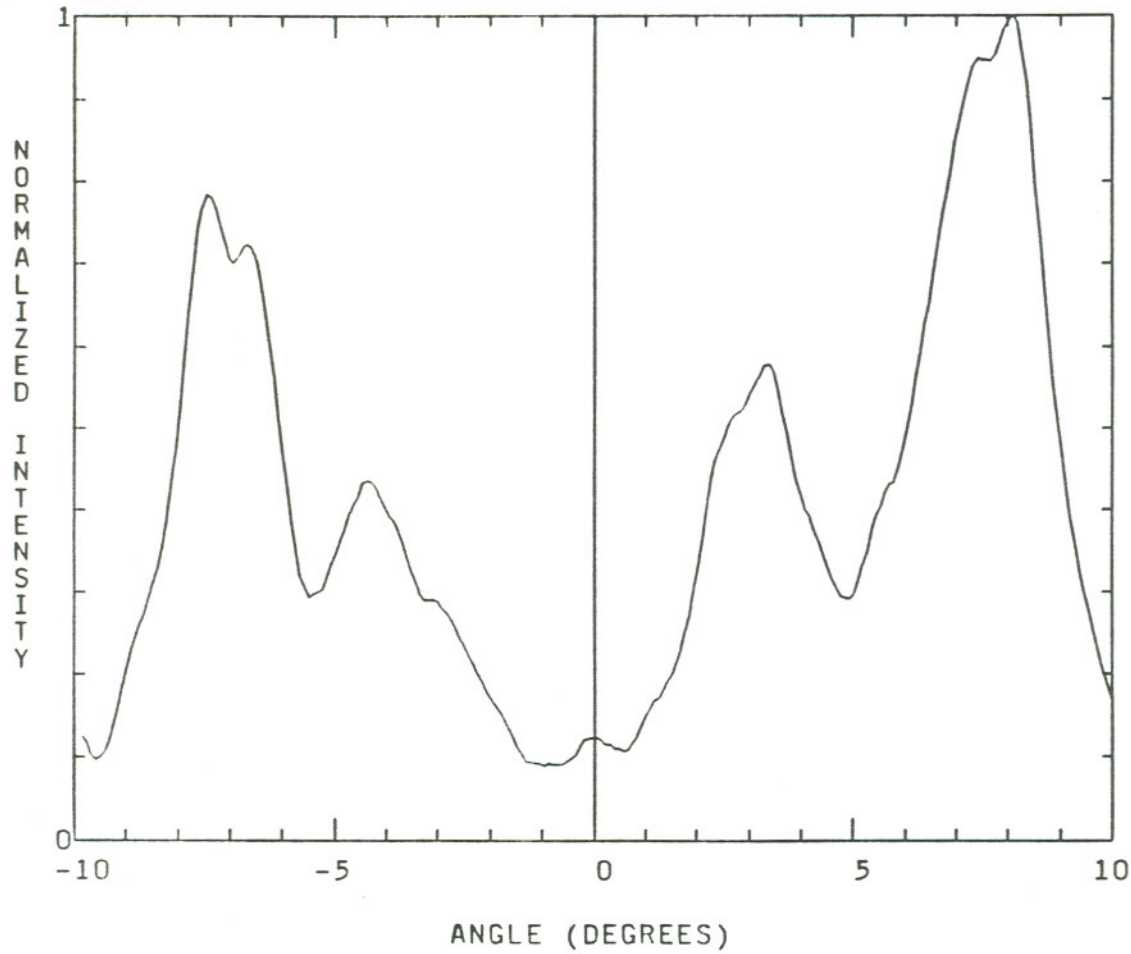

Figure 5.30 — Far field characteristics of unstable resonator A1-#4 at an output power level of 500 mW.

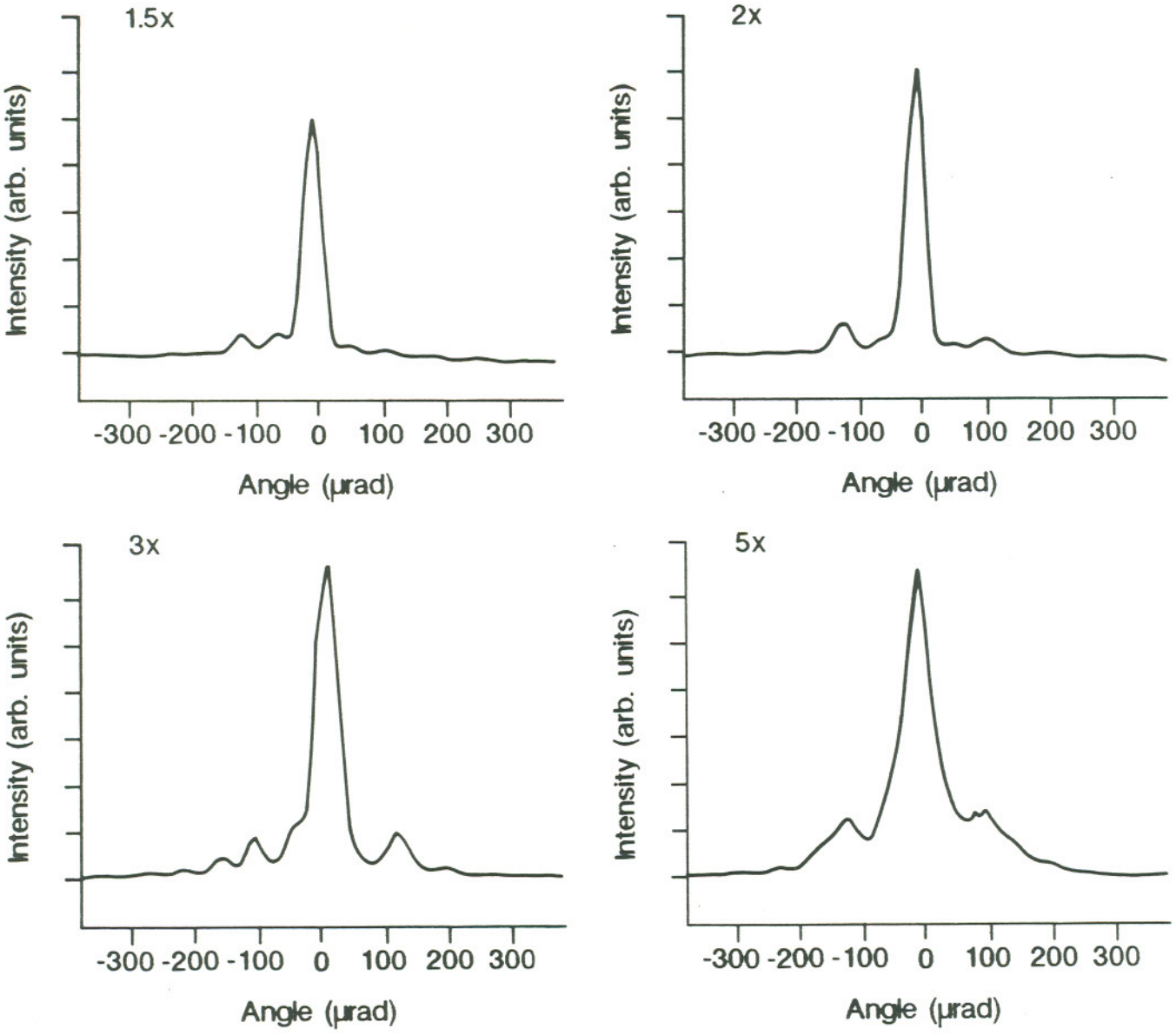

Figure 5.31 — Images of virtual point source of unstable resonator A1-#3, at currents of 1.5, 2, 3, and 5 times threshold.

increased to about 57 μm at 5 times threshold. Converting these values to angles, the FWHM divergences of the beams are 35 μrad and 64 μrad, respectively.

Unfortunately, no quantitative measurements were made of the lateral coherence, nor of the number of transverse modes operating in the laser, so it is unclear whether the laser is operating in the diffraction limit or not. In any case, although such a focusing arrangement is not practical for some applications, it might find use in optical disk writing or laser printing, where a high power focused spot is required.

Chapter 6
Conclusions and Future Work

6.1 Conclusions

The two numerical models presented in this thesis, that of Tilton and that of Chow, are an improvement over earlier analytical work, since they take into account gain and complex refractive index effects, and evaluate the field at many points inside the resonator. However, the two models gave much different results: the Tilton model produced a single-lobed diffraction-limited far field, while the Chow model a multi-lobed far field.

The two models have two basic differences. First, in the Tilton model, the wave propagation is calculated in terms of the components of a Fourier expansion of the electric field (Eqs. 3.7-3.8), while in the Chow model, it is calculated in terms of the field itself (Eq. 3.21). Second, the relationship between the gain and the carrier density is expressed in the Tilton model as linear equations (Eqs. 3.9-3.10) and in the Chow model as a second order differential equation (Eq. 3.23). It is not clear how much either of these differences would account for the observed discrepancy. In any case, neither of the two models matched the actual

far fields measured from any of the fabricated unstable resonator semiconductor lasers, although superficially the Chow model (Fig. 3.11) seems to more closely agree with the experimental results (Figs. 5.25 - 5.30).

There are two main limitations of the current models which must be addressed. The first is that the total mode loss is not calculated; for an active model the loss is not the same quantity as the mirror losses of the analytical models, and must somehow be derived from the gain at each point in the laser. The second is that the solution technique of launching an initial field into the resonator and letting it bounce around until it reaches a steady state only solves for the lowest loss transverse mode. The solution of these problems hopefully will produce useful tools for the design of unstable resonator semiconductor lasers.

The micromachining process produced curved mirrors which were smooth, close to the expected dimensions, and reproducible. The threshold currents and output powers were similar for all the machined unstable resonators. Although the lasers showed a large increase in threshold compared to the unmachined laser, they showed only a slight decrease in efficiency, which suggests either that a saturable absorbing region is created or that the threshold current depends more sensitively on the losses induced by the machining process than does the slope efficiency. The highest recorded output power, 600 mW, was the highest reported for an unstable resonator semiconductor laser. However, the spectra of the laser at that power showed almost one hundred longitudinal modes, with a

single dominant mode only at small ranges of output power. The far field patterns showed two major lobes, when a single lobe was desirable. Oxide-induced strain may have caused some distortion of the phase distribution at the facet, but this was not proven. The reproducibility of the patterns suggest that they are dependent on the resonator design, and that a different design might give better results.

6.2 Future Work

What clearly needs to be done is to create a simulation program that can accurately model the output of an unstable resonator semiconductor laser, so that it can be designed for optimal output characteristics, such as single-lobed or single lateral mode operation. It would be valuable to produce plots such as ones presented in Chapter 2, where the losses of the first few lateral modes are plotted against some parameter such as the equivalent Fresnel number or the resonator length, to use focused ion beam micromachining to fabricate unstable resonator lasers of various configurations, and then to compare experiment with theory.

On the characterization side, one important measurement that was not made of the lasers was of the lateral spatial coherence. Even though there were two lobes in the far field, if the output beam were spatially coherent then in theory the lobes could be combined to form a single-lobed diffraction-limited beam.

To decrease the number of longitudinal modes observed, a possible solution might be to use focused ion beam micromachining to incorporate a coupled cavity into the waveguide, as is done with conventional Fabry-Perot semiconductor lasers. Future study should determine whether the machined groove should be straight, have the same curvature of the mirror, or be concentric with the curved mirror. Furthermore, a separate contact could be attached to each waveguide section, to study the possibility of wavelength tuning.

References

1. T.H. Maiman, "Stimulated optical radiation in ruby," *Nature*, vol. 187, p. 493, August 1960.
2. D. Botez, "Recent developments in high-power single-element fundamental-mode diode lasers," *Laser Focus/Electro-Optics*, pp. 68--79, March 1987.
3. P.A. Kirkby, A.R. Goodwin, G.H.B. Thompson, and P.R. Selway, "Observations of self-focusing in stripe geometry semiconductor lasers and the development of a comprehensive model of their operation," *IEEE J. Quantum Electron.*, vol. QE-13(8), pp. 705-719, Aug. 1977.
4. D.R. Scifres, R.D. Burnham, and W. Streifer, "High power coupled multiple stripe quantum well injection lasers," *Appl. Phys. Lett.*, vol. 41(2), pp. 118-120, 15 July 1982.
5. D. Ackley, "High-power multiple-stripe injection lasers with channel guides," *IEEE J. Quantum Electron.*, vol. QE-18(11), pp. 1910-1917, Nov. 1982.
6. J. Katz, S. Margalit, and A. Yariv, "Diffraction coupled phase locked laser array," *Appl. Phys. Lett.*, vol. 42(7), pp. 554-556, 1 April 1983.
7. E. Kapon, C.P. Lindsey, J.S. Smith, S. Margalit, and A. Yariv, "Inverted-V chirped phased arrays of gain-guided GaAs/GaAlAs diode lasers," *Appl. Phys. Lett.*, vol. 45(12), pp. 1257-1259, 15 December 1984.
8. D.F. Welch, D. Scifres, P. Cross, H. Kung, W. Streifer, R.D. Burnham, and J. Yaeli, "High-power (575 mW) single-lobed emission from a phased-array laser," *Electron. Lett.*, vol. 21(14), pp. 603-605, 4 July 1985.
9. D.F. Welch, D. Scifres, P. Cross, H. Kung, W. Streifer, R.D. Burnham, J. Yaeli, and T.L. Paoli, "High power CW operation of phased array diode lasers with diffraction limited output beam," *Appl. Phys. Lett.*, vol. 47(11), pp. 1134-1136, 1 December 1985.
10. M. Taneya, M. Matsomoto, S. Matsui, S. Yano, and T. Hijikata, "0° phase mode operation in phased-array diode with symmetrically branching waveguide," *Appl. Phys. Lett.*, vol. 47(4), pp. 341-343, 15 August 1985.
11. L.J. Mawst, D. Botez, T.J. Roth, and J.J. Yang, "Diffraction-limited beam operation from a quantum-well laser phase-locked array grown by metalorganic chemical vapour deposition.," *Electron. Lett.*, vol. 24, pp. 570-571, 28 April 1988.
12. D. Botez, L.J. Mawst, P. Hayashida, and T.J. Roth, "High-power, diffraction-limited-beam operation from interferometric, phase-locked arrays of AlGaAs/GaAs diode lasers.," *J. Appl. Phys.*, vol. 65(9), pp. 3176-3178, 1 May 1989.
13. G.D. Boyd and H. Kogelnik, "Generalized confocal resonator theory," *Bell Syst. Tech. J.*, vol. 41, p. 1347, July 1962.

14. A.E. Siegman, "Unstable resonator optical resonators for laser applications," *Proc. IEEE*, pp. 277-287, March 1965.

15. A.P. Bogotov, P.G. Eliseev, M.A. Man'ko, G.T. Mikaslyan, and Y.M. Popov, "Injection laser with an unstable resonator," *Sov. J. Quantum Electron.*, vol. 10 (5), pp. 620-622, May 1980.

16. R. Craig, L. Casperson, D. Stafsudd, J.J.J. Yang, G. Evans, and R. Davidheiser, "Etched mirror unstable resonator semiconductor lasers," *Electron. Lett.*, vol. 21 (2), pp. 62-3, 17 Jan 1985.

17. R. Craig, *Unstable resonator semiconductor lasers.*, Ph.D. Thesis, University of California, Los Angeles, 1985.

18. R. Lang, M. Mittelstein, A. Yariv, and J. Salzman, "Unstable resonator semiconductor lasers I-Theory," *IEE Proc. J.*, vol. 134 (1), pp. 69-75, Feb 1987.

19. J. Salzman, T. Venkatesan, R. Lang, M. Mittelstein, and A. Yariv, "Unstable resonator semiconductor lasers II-Experiment," *IEE Proc. J.*, vol. 134 (1), pp. 76-86, Feb 1987.

20. H. Wang, Y.Y. Liu, M. Mittelstein, T.R. Chen, and A. Yariv , "GaInAsP/InP unstable resonator lasers," *Electron. Lett.*, vol. 23 (18), pp. 949-51, 27 Aug 1987.

21. J. Salzman and A. Yariv, "Phase-locked arrays of unstable resonator semiconductor lasers," *Appl. Phys. Lett.*, vol. 49 (8), pp. 440-2, 25 Aug 1986.

22. R. K. DeFreez, J. Puretz, R. A. Elliott, G. A. Crow, H. Ximen, D. J. Bossert, G. A. Wilson, and J. Orloff, "Focused-ion-beam micromachined diode laser mirrors," *Proceedings of the Society of Photo-Optical Engineers*, vol. 1043, pp. 25-35, 1989.

23. D. J. Bossert, R. K. DeFreez, H. Ximen, R. A. Elliott, J. M. Hunt, G. A. Evans, N. W. Carlson, M. Lurie, J. M. Hammer, D. P. Bour, S. L. Palfrey, and R. Amantea, "Grating surface emitting lasers in a ring configuration," *Appl. Phys. Lett.*, 21 May 1990.

24. R.K. DeFreez, J. Puretz, J. Orloff, R.A. Elliott, H. Namba, E. Omura, and H. Namizaki, "Operating characteristics and elevated lifetests of focused ion beam micromachined transverse junction stripe lasers," *Appl. Phys. Lett.*, vol. 53(13), pp. 1153-1155, 26 September 1988.

25. A.G. Fox and T. Li, "Modes in a maser interferometer with curved and tilted mirrors," *Proc. IEEE*, vol. 51, p. 89, January 1963.

26. A.G. Fox and T. Li, "Resonant modes in a maser interferometer," *Bell Syst. Tech. J.*, vol. 40, pp. 453-488, March 1961.

27. A.G. Fox and T. Li, "Resonant modes in a maser interferometer with curved mirrors," *Quantum Electronics III*, p. 1263, Columbia University Press, New York, 1964.

28. A.E. Siegman and R. Arrathoon, "Modes in unstable optical resonators and lens waveguides," *IEEE J. Quantum Electron.*, vol. QE-3(4), pp. 156-163, April 1967.

29. M. J. Smith, "Simplified calculation of mode degeneracy in unstable strip resonators," *Appl. Opt.*, vol. 20(24), pp. 4148-4149, 15 December 1981.

30. P. Horwitz, "Asymptotic theory of unstable resonator modes," *J. Opt. Soc. Amer.*, vol. 63, pp. 1528-1543, December 1974.

31. R.L. Sanderson and W. Streifer, "Unstable laser resonator modes," *Appl. Opt.*, vol. 8(10), pp. 2129-2136, October 1969.

32. A.E. Siegman and H.Y. Miller, "Unstable optical resonator loss calculations using the Prony method," *Appl. Opt.*, vol. 9(12), pp. 2729-2736, December 1970.

33. L.W. Chen and L.B. Felsen, "Coupled-mode theory of unstable resonators," *IEEE J. Quantum Electron.*, vol. QE-9, pp. 1102-1113, November 1973.

34. W.H. Southwell, "Virtual-source theory of unstable resonator modes," *Opt. Lett.*, vol. 6, pp. 487-489, October 1981.

35. A.E. Siegman, *Lasers,* pp. 859-923, University Science Books, Mill Valley, CA, 1986.

36. R. Lang, J. Salzman, and A. Yariv, "Modal analysis of semiconductor lasers with nonplanar mirrors," *IEEE J. Quantum Electron.*, vol. QE-22 (3), pp. 463-70, Mar 1986.

37. J. Salzman, R. Lang, and A. Yariv, "Eigenvalues of unstable resonator semiconductor lasers," *Opt. Comm.*, vol. 61 (5), pp. 332-6, 1 Mar 1987.

38. M. Tilton, G. Dente, and A. Paxton, "Mode control of broad area semiconductor lasers using unstable resonators," *Proc. OE/LASE '90*, p. 423, Los Angeles, CA, 16 January 1990.

39. M. Tilton and D. Depatie, Private communications.

40. J. Crank and P. Nicolson, "A practical method for numerical evaluation of partial differential equations of the heat conduction type.," *Proc. Cambridge Phil. Soc.*, vol. 43, pp. 50-66, 1947.

41. W. Chow and D. Depatie, "Filamentaion in conventional double heterostructure and quantum well semiconductor lasers," *IEEE J. Quantum Electron.*, vol. 24, pp. 1297-1301, July 1988.

42. W. Chow and D. Depatie, "Wave-optical effects in semiconductor laser amplifiers," *J. Appl. Phys.*, vol. 65, pp. 4124-4132, 1 June 1989.

43. B. Hakki, "Carrier and gain spatial profiles in GaAs stripe geometry lasers.," *J. Appl. Phys.*, vol. 44, pp. 3021-3028, 1973.

44. R. Bracewell, *The Fourier Transform and Its Applications,* pp. 275-281, McGraw-Hill Book Company, New York, 1965.

45. *NAG Fortran Library,* Numerical Algorithms Group, Oxford, United Kingdom, 1984.

46. D.W. Shaw, "Localized GaAs etching with acidic hydrogen peroxide solutions," *J. Electrochem. Soc.*, vol. 128, pp. 874-880, April 1981.

47. M. Wada, K. Hamada, T. Shibutani, H. Shimizu, M. Kume, K. Itoh, G. Kano, and I. Teramoto, "A new chemical etching technique for formation of cavity facets of (GaAl)As lasers," *IEEE J. Quantum Electron.*, vol. QE-21, pp. 658-662, 1985.

48. J. Puretz, "A theoretical and experimental study of liquid metal ion sources and their application to focused ion beam technology," *Ph.D. Dissertation,* Oregon Graduate Institute, December 1988.

49. H. Ximen, "A study of focued ion beam micromachining by development of a 3-D computer simulation and a 3-D digital scan strategy," *Ph.D. Dissertation,* Oregon Graduate Institute, September 1990.

Appendix A
Unstable Resonator Modeling Programs

This appendix contains programs to model the near field and far field characteristics of unstable resonator semiconductor lasers.

The program UNS.FOR, donated by Weng Chow of Sandia Laboratories and described in detail in Chapter 3, models the propagation of an electric field in an unstable resonator semiconductor laser. The modified version of the program, listed here, requires two input files. The first, UMODE.PARAM, is a simple one line file which contains the desired mirror curvature in microns (negative curvatures are concave toward the cavity), the cavity length in microns, the total number of passes, and the prefix for the generated output files. The second, TAPE10QW.DAT, contains various constants, parameters for calculating the current, loss, and initial field distributions, and the lookup table for determining the gain and index change as a function of the current density. After each propagation pass through the resonator, UNS.FOR outputs the phase and intensity distributions of the field at the planar mirror as a function of position across the stripe, in a form compatible with graphics software of the APEE MicroVax II.

The program NEAR.FAR.F takes the the real and imaginary parts of a

complex near field distribution and calculates the corresponding Fraunhofer far field intensity distribution using a fast Fourier transform (FFT) routine, as described in Section 3.6 .

******** UNS.FOR ********

```
      call param
      call reson
      stop
      end

      subroutine param
      common/lcfield/u(-1:202),xi(203),xp(203),
     $watt(10),us(201,201)
      complex u,us
      common/lcdim/y(201),jmax,dy,zmax,nmax,nswp,xk,yn0,dz,h
      common/lcden/xn0(203),eloss(203)
      common/lcgain/ag,bg,fill,xng(203),gxn(203),
     $pxn(203),ng
c
      open(10,file='tape10qw.dat')
      read(10,*)ymax,jmax
      read(10,*)xnmax,dl1,dl2,dl21,yn0,ynb
      read(10,*)xint0,xint1,ya0,yab,an0,an1c,an1s
      read(10,*)elmax,elmin,yloss0,ylossb,ylossf
      read(10,*)fill,h
      read(10,*)ng
      read(10,*)(xng(i),gxn(i),pxn(i),i=1,ng)
      xk=2.*3.142*3.6/.85
c  compute gain parameters (all in cgs)
      gamnr=.2e9
      b=1.4e-10
      ag=1.e18*b/gamnr
      bg=1.e7/(1.45*1.6*gamnr)
c  compute unsaturated carrier distribution
      if(jmax.gt.1)dy=ymax/(jmax-1)
      ynb2=.5*ynb
      x1=ynb2/dl1
      aa=1./(cosh(x1)+dl21*sinh(x1))
      bb=xnmax*aa*dl21*sinh(x1)*exp(ynb2/dl2)
c     xnmaxp=xnmax*ynb2/(dl1*alog(1.+exp(ynb2/dl1)))
      do1j=1,jmax
      y(j)=(j-1)*dy
      yj0=abs(y(j)-yn0)
      if(yj0.gt.ynb2)then
      xn0(j)=bb*exp(-yj0/dl2)
      else
```

```
      xn0(j)=xnmax*(1.-aa*cosh(yj0/dl1))
      endif
c     xn0(j)=xnmaxp/(exp((yj0-ynb2)/dl1)+1.)
    1 continue
c compute eloss distribution
      ylb2=ylossb/2.
      deloss=elmax-elmin
      do9j=1,jmax
      eloss(j)=elmax-deloss/(exp((abs(y(j)-yloss0)-ylb2)/ylossf)+1.)
    9 continue
c compute initial field distribution
      a0=sqrt(xint0)
      a1=sqrt(xint1)
      na2=2*an0
      yab2=yab/2.
      u(-1)=cmplx(0.,0.)
      u(jmax+1)=cmplx(0.,0.)
      do2j=1,jmax
c     u(j)=cmplx(exp(-((y(j)-ya0)/yab2)**na2)*
c    $(a0+a1*((y(j)-ya0)/yab2)**an1),0.)
      y1=3.142*(y(j)-ya0)/yab2
      u(j)=cmplx(exp(-((y(j)-ya0)/yab2)**na2)*
     $(a0*cos(an1c*y1)+a1*sin(an1s*y1)),0.)
    2 continue
      return
      end

      subroutine inten
c computes intensity (MW/cm2), phase (rad) and power (W).
      common/lcfield/u(-1:202),xi(203),xp(203),
     $watt(10),us(201,201)
      complex u,us
      common/lcdim/y(201),jmax,dy,zmax,nmax,nswp,xk,yn0,dz,h
      common/lcgain/ag,bg,fill,xng(203),gxn(203),
     $pxn(203),ng
      w=0.
      do1j=1,jmax
      ur=real(u(j))
      ui=aimag(u(j))
      xi(j)=ur**2+ui**2
      if(ui.ne.0..or.ur.ne.0.)xp(j)=atan2(ui,ur)
      w=xi(j)+w
    1 continue
```

```
      return
      end


      subroutine reson
c  propagates field inside resonator
      common/lcfield/u(-1:202),xi(203),xp(203),
     $watt(10),us(201,201)
      complex u,us
      common/lcdim/y(201),jmax,dy,zmax,nmax,nswp,xk,yn0,dz,h
      common/lcprop/alpha,beta,a(201),b(201),c(201),r(201)
      complex alpha,beta,a,b,c,r
      character*3 title

      ncount = 0
c  define laser configuration
c  r2c<0 for convex facet, r2c>0 for concave facet, r2c=0 for plane facet
c  uncoated facet, L=500microns

      r1 = 0.32
      r2 = 0.32
      nmax = 201
      nswp = 10
    4 open(4,file='umode.param')
      read(4,*)r2c,zmax,npass,title
      close(4)

c  open files for output
      open(21,file=title//'.inten')
      open(22,file=title//'.phase')
      open(49,file=title//'.power')

      ra1=sqrt(r1)
      ra2=sqrt(r2)
      if(r2c.ne.0.)phi1=r2c*2.*xk
      call pinit
      do 2 n = 1,npass
c  reflection at mirror 1 (plane mirror)
      do50j=1,jmax
   50 u(j)=ra1*u(j)
      if (n.eq.npass) then
        call inten
        do41j=1,jmax
```

```
      write(49,*) xi(j)
   41 continue
      endif
c  propagate from left to right
      call res(1)
      if (n.eq.npass) then
        call inten
        do42j=1,jmax
        write(49,*) xi(j)
   42 continue
      endif
c  reflection at mirror 2 (r2c=0 means plane mirror, < 0 means convex
c  and > 0 means concave)
      if(abs(r2c).le.1.e-3)then
      do60j=1,jmax
   60 u(j)=ra2*u(j)
      else
      do8j=1,jmax
      phi2=phi1*(1.-sqrt(1.-((y(j)-yn0)/r2c)**2))
      u(j)=ra2*cexp(cmplx(0.,-phi2))*u(j)
    8 continue
      endif
      if (n.eq.npass) then
        call inten
        do43j=1,jmax
        write(49,*) xi(j)
   43 continue
      endif
c  propagate from right to left
      call res(-1)
c  computes intensity and phase of incident wave at mirror 1
      call inten
      if (n.eq.npass) then
        do13j=1,jmax
        write(49,*) xi(j)
   13 continue
      endif
      ncount = ncount + 1
      if (ncount.eq.5) then
        do 14 j = 1,jmax
        write(21,*) y(j),xi(j)
        write(22,*) y(j),xp(j)
   14 continue
```

```
        if (n.ne.npass) then
            write(21,*)'
            write(22,*)'
        endif
      ncount = 0
      endif
      open(99, file = title//'.status')
      write(99,*)n,' passes completed'
      close(99)
    2 continue
      close(49)
      close(21)
      close(22)
      return
      end

      subroutine pinit
c computes matrix for propagation
      common/lcfield/u(-1:202),xi(203),xp(203),
     $watt(10),us(201,201)
      complex u,us
      common/lcdim/y(201),jmax,dy,zmax,nmax,nswp,xk,yn0,dz,h
      common/lcprop/alpha,beta,a(201),b(201),c(201),r(201)
      complex alpha,beta,a,b,c,r
      dz=zmax/(nmax-1)/nswp
      alpha=cmplx(0.,.25*dz/xk/dy**2)
      beta=(1.-2.*alpha)
      do1j=1,jmax
      a(j)=-alpha
      b(j)=(1.+2.*alpha)
    1 c(j)=-alpha
c     write(6,100)alpha,a(1),b(1),c(1)
c 100 format(' alpha a b c:',1p,2(/2(2(1x,e9.2),3x)))
      return
      end
      subroutine tridag(n)
c  diagonalizes matrix
      common/lcprop/alpha,beta,a(201),b(201),c(201),r(201)
      complex alpha,beta,a,b,c,r
      common/lcfield/u(-1:202),xi(203),xp(203),
     $watt(10),us(201,201)
      complex u,us
      complex gam(201),bet
```

```
      bet=b(1)
      u(1)=r(1)/bet
      do11j=2,n
      gam(j)=c(j-1)/bet
      bet=b(j)-a(j)*gam(j)
      if(abs(bet).eq.0.)pause
      u(j)=(r(j)-a(j)*u(j-1))/bet
   11 continue
      do12j=n-1,1,-1
      u(j)=u(j)-gam(j+1)*u(j+1)
   12 continue
      return
      end
      subroutine res(ndir)
c  propagates field forward for ndir=1 and backwards for ndir=-1
      common/lcfield/u(-1:202),xi(203),xp(203),
     $watt(10),us(201,201)
      complex u,us
      common/lcdim/y(201),jmax,dy,zmax,nmax,nswp,xk,yn0,dz,h
      common/lcprop/alpha,beta,a(201),b(201),c(201),r(201)
      complex alpha,beta,a,b,c,r
      common/lcden/xn0(203),eloss(203)
      complex dus(201),usp,f,cgain
      if(ndir)5,4,4
    4 nstart=1
      nend=nmax-1
      goto6
    5 nstart=nmax
      nend=2
    6 do1n=nstart,nend,ndir
      n1=n+ndir
      do3j=1,jmax
      dus(j)=(us(j,n1)-us(j,n))/nswp
      us(j,n)=u(j)
    3 continue
   10 do1i=1,nswp
      do2j=1,jmax
      usp=us(j,n1)-dus(j)*(nswp-i+1)
      xint=conjg(u(j))*u(j)+conjg(usp)*usp
      call gain(xint,xn0(j),eloss(j),xn,cgain)
      f=cgain*u(j)
      r(j)=alpha*(u(j+1)+u(j-1))+beta*u(j)+dz*f
    2 continue
```

```
      call tridag(jmax)
    1 continue
      do7j=1,jmax
      us(j,n1)=u(j)
    7 continue
      return
      end
      subroutine gain(xint,xn0,eloss,xn,cgain)
c  computes complex modal gain in 1/micron
c  xint is in Mw/cm2, den in 1.e18/cm3
      common/lcgain/ag,bg,fill,xng(203),gxn(203),
     $pxn(203),ng
      complex cgain
      if(xn0.gt.xng(1))goto4
      xn=xn0
      cgain=.5e-4*(fill*cmplx(gxn(1),2.*pxn(1))-eloss)
      return
    4 x3=xint*bg
      do1i=1,ng
      x1=xn0-xng(i)
      x2=xn0+xng(i)
      dy=x1*(1.+ag*x2)-x3*gxn(i)
      if(abs(dy).gt.1.e-5)goto2
      xn=xng(i)
      cgain=.5e-4*(fill*cmplx(gxn(i),2.*pxn(i))-eloss)
      return
    2 if(i.eq.1)goto3
      if(dy/dys.gt.0.)goto3
      dxng=xng(i)-xng(i-1)
      xn=xng(i-1)-dys*dxng/(dy-dys)
      gr=gxn(i-1)+(gxn(i)-gxn(i-1))/dxng*(xn-xng(i-1))
      pr=pxn(i-1)+(pxn(i)-pxn(i-1))/dxng*(xn-xng(i-1))
      cgain=.5e-4*(fill*cmplx(gr,2.*pr)-eloss)
      return
    3 dys=dy
    1 continue
      write(6,*)' no solution: xn0=',xn0,' xint=',xint
      stop
      end
```

******** UMODE.PARAM ********

-2000 450 1000 c05

******** TAPE10QW.DAT ********

```
300. 201
6.0 3. 3. 1. 150. 100.
100. 3. 150. 200. 1.
39
0.5  -534.  -575.
1.0  -339.  -1022.
1.5  -132.  -1235.
2.0    71.  -1334.
2.2   148.  -1363.
2.4   245.  -1384.
2.6   328.  -1403.
2.8   425.  -1413.
3.0   512.  -1425.
3.2   583.  -1434.
3.4   647.  -1447
3.6   705.  -1456.
3.8   773.  -1469.
4.0   823.  -1478.
4.2   878.  -1487.
4.4   919.  -1494.
4.6   968.  -1503.
4.8  1006.  -1509.
5.0  1052.  -1522.
5.2  1084.  -1528.
5.4  1116.  -1541.
5.6  1148.  -1550.
5.8  1177.  -1566.
6.0  1209.  -1575.
6.2  1232.  -1587.
6.4  1255.  -1597.
6.6  1280.  -1606.
6.8  1303.  -1622.
7.0  1325.  -1634.
7.5  1380.  -1662.
8.0  1432.  -1691.
8.5  1474.  -1722.
9.0  1512.  -1753.
```

```
9.5  1544.  -1784.
10.0 1580.  -1812.
10.5 1612.  -1840.
11.0 1640.  -1872.
11.5 1665.  -1894.
12.0 1695.  -1925.
```

******** NEAR.FAR.F ********

```
      double precision xreal(200),ximag(200)
      real y(200)
     integer i, ifail, j, jm1, n
      open(1,file="rdat.near")
      open(2,file="idat.near")
      open(3,file="inten.near")
      n=200
      do 100 i=1,n
            read(1,*)xnull,xreal(i)
            read(2,*)xnull,ximag(i)
            y(i)=dsqrt(xreal(i)*xreal(i)+ximag(i)*ximag(i))
            write(3,*)i,y(i)
 100  continue
      close(1)
      close(2)
      close(3)
     ifail = 0
     call c06ecf(xreal, ximag,  n, ifail)
      write(*,*)ifail
      open(4,file="inten.far")
     do 60 j=1,n/2
       jm1 = j - 1
            y(n/2+j)=dsqrt(xreal(j)*xreal(j)+ximag(j)*ximag(j))
  60 continue
     do 70 j=n/2,n
      jm1 = j - 1
            y(j-n/2)=dsqrt(xreal(j)*xreal(j)+ximag(j)*ximag(j))
  70 continue
     do 80 k=1,n
            write(4,*)k,y(k)
 80   continue
      close(4)
     end
```

Appendix B
Micromachining Control Program

This appendix contains the program ARC7.C, which was used in the focused ion beam micromachining of curved mirrors in semiconductor lasers. The program sends addresses to a CAMAC crate, a controller for eight digital-to-analog converters (DACs). The DACs send the control signals to the ramp generators, whose output goes to the ion beam controller, as described in Section 4.4 . The program prompts the user for the number of milling passes of the curved area, and displays the required voltage setting of the high resolution scan circuit, also described in Section 4.4 . The radius and aperture of the curved area are fixed for this program, but they can be changed by adjusting the appropriate variables, as given by the comment statements in the program.

The voltage setting of the high resolution circuit is measured by a digital multimeter, contacting one lead to the test point of the circuit and another to the ground of one of the BNC connectors. The setting is adjusted by a 20-turn potentiometer on the front panel of the circuit assembly. With the 10V input test signal, the output of the test point ranges from 0 V to 1 V. For a given mirror depth (d), if the displayed voltage setting is above this range, the number of line scans (LINES) must be increased.

The timing routines are dependent on the VMS operating system, and would most likely need to be changed if the program is run on another system.

******** ARC7.C ********

```
/* This control program creates a piece of a disk on the side,
by using overlapping line scans.*/

      /* To make the disk, connect the output of DAC #5 to
the DAC to be divided input of the High Res Circuit.  Connect
DAC #7 to the DAC to be added input of the HRC. Connect the x offset
input of the ramp generator to the output of the HRC. With DAC #5 set
at 10V (2047), turn the pot so that the proper voltage is at the test point. */



#include   <stdio.h>
#include   <math.h>
#include   <descrip.h>

main()
{
float       R;    /* Radius of the disk in "pixel space" */
float       D;    /* Depth of the piece in " pixel space" */
int         OLINES; /* Number of line scans past end of aperture */
int          LINES;   /* Number of line scans for curved mirror */
float       r;     /* D/LINES Reduction ratio of High Res Circuit */
int         p;     /* Number of milling roundtrips */

      short channel, crate, sta, func;

      /* These are variables whose values are sent to the DACs */
      int   x_amp = 0;
      int   y_amp;
      int   x_slope = 2047;
      int   y_slope = 2047;
      int   x_off;
      int   y_off;
      int   yes_blank = 1024;
      int   no_blank = 0;
      int   _off = OFF;

      /* These are DAC module addresses    */
      int   yamp = 0;
      int   xamp = 1;
      int   yslope      = 2;
```

```
        int    xslope = 3;
        int    yoff   = 4;
        int    xoff   = 5;
        int    blank = 6;
        int    off = 7;

        int    i, j, k, error, v ;

        int    statusarray[6];
        int    length[701];
        int    time[701];

        float test;
        double      dummy;

        $DESCRIPTOR(name, "CAA0:");


/*      Time Routine            */

        int millisec,start,finish ;
        char cur_time[24];
        $DESCRIPTOR(cur_time_desc, cur_time);
        register status;
/* ------------------------------------------------------------------------*/
/* Initialization of CAMAC */

        crate = 1;
        sta = 3;
        func = 16;

        caopen(&channel, &name, &error);
        if(error != 1)
              camsg(&error);

        printf("Crate channel open\n");

        cam16(&channel,&crate,&sta,&blank,&func,
                                  &yes_blank,statusarray);
        if (statusarray[0] != 1)
              printf("An error has occured\n");

printf("Radius=2000 2A=200: R=15000  D=18.75  LINES=500  OLINES=200\n");
```

```
R = 15000; D = 18.75; LINES = 500; OLINES = 200;
printf("Input number of passes\n");
r = D/LINES;
getchar();


/* This section calculates the length and time for each linescan */

for (i = 1; i <= LINES+OLINES; i++)
{
      length[i] = (int)(2 * sqrt((double)((R*R)-(R-i*r)*(R-i*r))));
      time[i]   = (int)(length[i] / 10) ;
}
length[0] = length[1];
time[0]   = time[1];

/* This section initializes x_amp, x_slope, y_slope, and _off */

cam16(&channel,&crate,&sta,&xamp,&func,&x_amp,statusarray);
if (statusarray[0] != 1)
      printf("An error has occured\n");

cam16(&channel,&crate,&sta,&xslope,&func,&x_slope,statusarray);
if (statusarray[0] != 1)
      printf("An error has occured\n");

cam16(&channel,&crate,&sta,&yslope,&func,&y_slope,statusarray);
if (statusarray[0] != 1)
      printf("An error has occured\n");

cam16(&channel,&crate,&sta,&off,&func,&_off,statusarray);
if (statusarray[0] != 1)
      printf("An error has occured\n");


/* This section is to aid in calibrating the High Res Circuit */


x_off = 2047;
cam16(&channel,&crate,&sta,&xoff,&func,&x_off,statusarray);
if (statusarray[0] != 1)
      printf("An error has occured\n");
```

```
        v = r*10000 - 6;
        printf("Adjust the test point to %d millivolts\n", v);

                printf("Press <RETURN> to begin milling.\n");
                getchar();

                cam16(&channel,&crate,&sta,&blank,&func,
                                        &no_blank,statusarray);
                if (statusarray[0] != 1)
                        printf("An error has occured\n");

/* This section makes the curved mirror.  At x_off = 0, i = LINES */
for (k = 1; k <= p; k++)
        {

        for(j = LINES+OLINES; j >= -1*(LINES+OLINES); j--)
                {
                        i = abs(j);
                        y_amp = length[i];
                        y_off = y_amp/2;
                        x_off = (i-LINES);

                        cam16(&channel,&crate,&sta,&yamp,&func,
                                        &y_amp,statusarray);
                        if (statusarray[0] != 1)
                                printf("An error has occured\n");

                        cam16(&channel,&crate,&sta,&yoff,&func,
                                        &y_off,statusarray);
                        if (statusarray[0] != 1)
                                printf("An error has occured\n");

                        cam16(&channel,&crate,&sta,&xoff,&func,
                                        &x_off,statusarray);
                        if (statusarray[0] != 1)
                                printf("An error has occured\n");

                /* The following is a wait routine*/
millisec = time[i];
if (((status=LIB$DATE_TIME(&cur_time_desc)) &1) != 1)
                LIB$STOP(status);
        cur_time[23] = '\0';
        start = 1000* (cur_time[19] - '0')
```

```
            +100* (cur_time[21]-'0') + 10* (cur_time[22]-'0');
        finish = start;
while((finish - start) < millisec)
{
if (((status=LIB$DATE_TIME(&cur_time_desc)) &1) != 1)
            LIB$STOP(status);
        cur_time[23] = '\0';
        finish = 1000* (cur_time[19] - '0')
            +100* (cur_time[21]-'0') + 10* (cur_time[22]-'0');
        if (finish < start)
            start = start - 10000;
}
            }
        printf("%3d passes completed on mirror\n",k);
        }

                cam16(&channel,&crate,&sta,&blank,&func,
                                &yes_blank,statusarray);
                if (statusarray[0] != 1)
                    printf("An error has occured\n");
            printf("Milling completed.  Press <RETURN> to exit.\n");
            for(i = 1; i <= 5; i++)
                { printf("\007"); sleep(1); }
            getchar();

                cam16(&channel,&crate,&sta,&blank,&func,
                                &no_blank,statusarray);
                if (statusarray[0] != 1)
                    printf("An error has occured\n");

        caclos(&channel, &error);
        camsg(&error);
}
```

BIOGRAPHICAL NOTE

The author was born in Perth Amboy, New Jersey on 26 March 1964. He spent much of his childhood in Fullerton, California, where he attended Troy High School. He attended the California Institute of Technology in Pasadena, California, and received the Bachelor of Science degree in Applied Physics in June 1985. From 1985 through 1988, he was a Member of the Technical Staff at the Jet Propulsion Laboratory, Pasadena, California, where he worked on the growth and processing of semiconductor lasers.

The author began his studies at the Oregon Graduate Institute in August 1988 and completed the requirements for the degree Master of Science in Applied Physics in September 1990.

The author's future plans are not clear at this time, but will very likely involve his true calling, playing the ukulele.